INTRODUCING THE COARSE-SCATTERING MULTIGROUP METHOD AND FINE-TUNING THE FINITE-ELEMENT WITH DISCONTIGUOUS-SUPPORT MULTIGROUP METHOD FOR TIME-DEPENDENT NEUTRON TRANSPORT

A Dissertation

by

PABLO ANDRÉS VAQUER

Submitted to the Graduate and Professional School of
Texas A&M University
in partial fulfillment of the requirements for the degree of

DOCTOR OF PHILOSOPHY

Chairs of Committee,	Ryan G. McClarren
Co-Chair of Committee,	Jim L. Morel
Committee Members,	Jean C. Ragusa
	Jean-Luc Guermond
Head of Department,	Michael A. Nastasi

December 2022

Major Subject: Nuclear Engineering

ABSTRACT

The purpose of this research is to reduce the runtime and improve the accuracy of deterministic neutron transport simulations. Here, we introduce the coarse-scattering (CS) method, and prove its ability to reduce the computational time required to model scattering in multigroup (MG) simulations. We applied the CS method to a slab-geometry criticality simulation and showed that it was able to reduce the overall runtime of the simulation by almost a factor of four. Furthermore, we proved that the coarse-scattering method can conserve particle balance as long as the CS scattering spectrum and CS fission spectrum are recomputed in the last iteration.

In this study, we also showed that finite-element with discontiguous-support (FEDS) method and the multigroup (MG) method have certain advantages and disadvantages for simulating time-of-flight problems. FEDS is inherently able to model cross sections more accurately, while MG inherently is able to model neutron speeds more accurately. We compared a wide variety of FEDS energy discretizations, and determined their performance for a single-material and a multi-material time-of-flight simulation. We found that either using FEDS energy discretizations with large energy penalties or FEDS energy discretizations with a small number of elements per coarse group performed best for time-of-flight simulations. The FEDS energy discretizations that used energy penalties were usually more accurate than the MG simulations for the single-material and the multi-material time-of-flight problems, for various detector distances and number of time bins. Also, the FEDS energy discretization that used exactly two FEDS elements in each coarse group was competitive with MG for the single-material time-of-flight problem and usually more accurate than MG for the multi-material time-of-flight problem.

DEDICATION

This dissertation is dedicated to my parents, my sister and my daughter.

ACKNOWLEDGMENTS

I would like to express my gratitude towards a few individuals who helped make this work possible. First, I would like to thank Dr. Ryan McClarren for his time, guidance and insight throughout these years. I would also like to thank Dr. Jim Morel, Dr. Jean Ragusa, and Dr. Jean-Luc Guermond for their insight and constructive feedback. I would also like to thank Dr. Teresa Bailey, Dr. Peter Brown, and Dr. Robert Cavallo at Lawrence Livermore National Laboratory for openly discussing the many challenges of this project. Additionally, I would like express my gratitude towards many of my fellow graduate students at Texas A&M University. Finally, and most importantly, I would like to express my deepest gratitude towards my family, for their love, support, and encouragement.

CONTRIBUTORS AND FUNDING SOURCES

Contributors

This work was supported by a dissertation committee consisting of my chair, Dr. Ryan McClarren, my co-chair, Dr. Jim Morel, and Dr. Jean Ragusa of the Department of Nuclear Engineering as well as Dr. Jean-Luc Guermond of the Department of Mathematics.

All work conducted for this dissertation was completed by the student independently.

Funding Sources

This work was sponsored by Lawrence Livermore National Laboratory and Texas A&M University.

TABLE OF CONTENTS

LIST OF FIGURES

FIGURE Page

LIST OF TABLES

TABLE Page

1. INTRODUCTION

The purpose of this research is to reduce the runtime and error in deterministic neutron transport simulations. Here, we introduce the coarse-scattering (CS) method to reduce the computational time required to model scattering in multigroup (MG) codes. Additionally, we compare various finite-element with discontiguous-support (FEDS) energy discretizations to determine which discretization works best for various steady-state and time-dependent quantities of interest.

Currently, there is no computationally-feasible way to model the true continuous-energy particle flux in neutron transport simulations. Monte Carlo codes do a great job of sampling from continuous distributions, however, for thermal reactor simulations, Monte Carlo codes tend to undersample the resolved and unresolved resonance range of the energy domain. Also, for fast reactor simulations, Monte Carlo codes tend to undersample the thermal and resolved resonance range of the energy domain. To make matters worse, the resolved resonance range can contain tens of thousands of resonances, the width of each resonance is quite small, and the neutron flux dips by orders of magnitude at each resonance, making it extraordinarily difficult to sample.

The deterministic MG method also does not properly capture resonance effects because the width of each energy group is much larger than the width of resonances. A single energy group can contain hundreds of resonances. In 2014, Till, Adams, and Morel [1] introduced FEDS, a generalization of MG that allows for discontiguous energy discretizations, and proved that it can capture resonance and spatial self-shielding effects more accurately than the standard MG method. Furthermore, Till demonstrated that FEDS performed much better than MG at estimating various steady-state quantities of interest [2]. However, Till has shown that FEDS previously performed slightly worse than MG for time-of-flight test problems with large detector distances [3]. For time-of-flight simulations, as the detector is moved further away, the neutron source becomes more accurately approximated as a point source. Also, as the detector is moved further away, there are larger time gaps between the slower neutrons and the faster neutrons arriving to the detector. For these reasons, neutron speed becomes the most important parameter to capture in the simulation. The problem with FEDS is that a discontiguous energy element can span an even wider range of energies than a contiguous energy group. This results in poorer estimates of true neutron speeds, and consequently makes it more challenging to accurately measure time-dependent quantities of interest. In this dissertation, we compare strategies for mitigating this effect, and improve the overall performance of FEDS for time-dependent simulations.

2. NEUTRON TRANSPORT THEORY

Nuclear reactors operate in a delicate state of equilibrium known as criticality. This state of equilibrium is so fragile that even a miniscule change in an underlying physical parameter can cause a reactor's power to decrease or increase exponentially in a matter of nanoseconds. Thankfully, the presence of delayed neutron precursors and negative-feedback effects make nuclear reactors easier to control. Also, the physics of nuclear reactors is well understood, and thus computer simulations can be used to accurately model various physical phenomena occurring in nuclear reactors.

The neutron transport equation is used for the highest-fidelity reactor physics simulations. In fact, neutron transport solvers are capable of predicting some quantities of interest, such as criticality, with error margins less than a fraction of a percent. Only a few assumptions are necessary to make the neutron transport equation valid:

1. Neutrons can be represented as singular points in space.
2. Neutron-nuclei interactions are binary.
3. All neutron interactions are instantaneous.
4. Long-range force fields are negligible.
5. The frequency of neutron-neutron interactions is negligible compared to neutron-nuclei interactions.
6. Free-neutron decay is negligible compared to neutron loss due to streaming and nuclear interactions.

Furthermore, in this study we assume:

7. The total cross section is independent of an incident neutron's direction $\hat{\Omega}$.

8. Fission is isotropic.

With these assumptions, the following time-dependent neutron transport equation can be derived:

$$\mathbf{L}\psi = (\mathbf{S} + \mathbf{F})\psi + Q \; , \tag{2.1}$$

where $\mathbf{L}$ is the loss operator, which represents any loss of neutrons,

$$\mathbf{L}\psi = \frac{1}{v(E)}\frac{\partial \psi}{\partial t} + \hat{\Omega} \cdot \nabla \psi + \Sigma_t(\vec{r}, E, t)\psi(\vec{r}, \hat{\Omega}, E, t) \; , \tag{2.2}$$

$\mathbf{S}$ is the scattering operator, which computes the source of scattered neutrons being emitted at energy E and direction $\hat{\Omega}$, caused by neutrons with initial energy E' and direction $\hat{\Omega}'$,

$$\mathbf{S}\psi = \int\limits_{4\pi} d\Omega' \int\limits_{0}^{\infty} dE' \, \Sigma_s(\vec{r}, \hat{\Omega}' \cdot \hat{\Omega}, E' \to E, t)\psi(\vec{r}, \hat{\Omega}', E', t) \; , \tag{2.3}$$

$\mathbf{F}$ is the fission operator, which computes the quantity and energy E of neutrons emitted from prompt fission reactions assuming that fission is isotropic,

$$\mathbf{F}\psi = \frac{1}{4\pi} \int\limits_{0}^{\infty} dE' \, \Sigma_f(\vec{r}, E' \to E, t)\phi(\vec{r}, E', t) \; , \tag{2.4}$$

$$\phi(\vec{r}, E', t) = \int\limits_{4\pi} d\Omega' \, \psi(\vec{r}, \hat{\Omega}', E', t) \; , \tag{2.5}$$

and Q is the extraneous source term, which includes other neutron sources in the medium, such as spontaneous fission sources and delayed neutron precursors,

$$Q = q(\vec{r}, \hat{\Omega}, E, t) + \sum_{i=1}^{N} \frac{\chi_{d,i}(E)}{4\pi} \lambda_i C_i(\vec{r}, t) \; . \tag{2.6}$$

Note:

$\vec{r}$	position of neutrons $< x, y, z >$
$\hat{\Omega}$	neutron direction-of-flight $< \theta, \varphi >$
E	neutron kinetic energy
t	time
$v(E)$	neutron speed
$\psi(\vec{r}, \hat{\Omega}, E, t)$	angular flux
$\Sigma_t(\vec{r}, E, t)$	total macroscopic cross section
$\Sigma_s(\vec{r}, \hat{\Omega}' \cdot \hat{\Omega}, E' \to E, t)$	double-differential scattering cross section
$\Sigma_f(\vec{r}, E' \to E, t)$	differential prompt fission cross section
$C_i(\vec{r}, t)$	concentration of delayed neutron precursor flavor i
λ_i	decay constant for precursor flavor i
$\chi_{d,i}(E)$	delayed neutron spectrum for precursor flavor i
$q(\vec{r}, \hat{\Omega}, E, t)$	other extraneous source terms, such as spontaneous fission.

For thermal reactors, the differential prompt fission cross section $\Sigma_f(\vec{r}, E' \to E, t)$ can be approximated as $\chi(E)\nu\Sigma_f(\vec{r}, E', t)$ because the kinetic energy of thermal neutrons is not enough to significantly impact the spectrum of neutrons being released from fission interactions. However, this approximation is not as accurate for fast reactors, where the incident neutron energy does noticeably affect the spectrum of neutrons being released from fission interactions.

Also, note that the loss, scattering, and fission operators are all linear operators,

$$\alpha \mathbf{L}\psi = \mathbf{L}\alpha\psi \, , \quad \alpha \mathbf{S}\psi = \mathbf{S}\alpha\psi \, , \quad \alpha \mathbf{F}\psi = \mathbf{F}\alpha\psi \, .$$

The steady-state neutron transport equation is sometimes referred to as the linear Boltzmann equation [4].

Some of the difficulties of solving the transport equation are buried into the energy dependence of cross sections. The energy dependence of cross sections can be complex due to nuclear resonances, a quantum mechanical effect which can cause nuclear cross sections to vary by several orders of magnitude due to a small change in incident neutron energy. Figure 2.1 shows how nuclear cross sections vary on a logarithmic scale.

Deterministic methods try to solve Eq. (2.1) by discretizing the six-dimensional phase space $\vec{r}$, $\hat{\Omega}$, and E, as well as time t.

2.1 The k-Eigenvalue Problem

The transport equation can be expressed as a generalized eigenvalue equation of the form $Ax = \lambda Bx$ [5]. This is done by assuming the neutron flux is steady-state and removing the extraneous source term. Specifically the k-eigenvalue transport equation is

$$(\mathbf{H} - \mathbf{S})\psi = \frac{1}{k}\mathbf{F}\psi \, , \tag{2.7}$$

where $\mathbf{H}$ is the streaming-and-removal operator,

$$\mathbf{H} = \hat{\Omega} \cdot \nabla + \Sigma_t(\vec{r}, E, t) \, ,$$

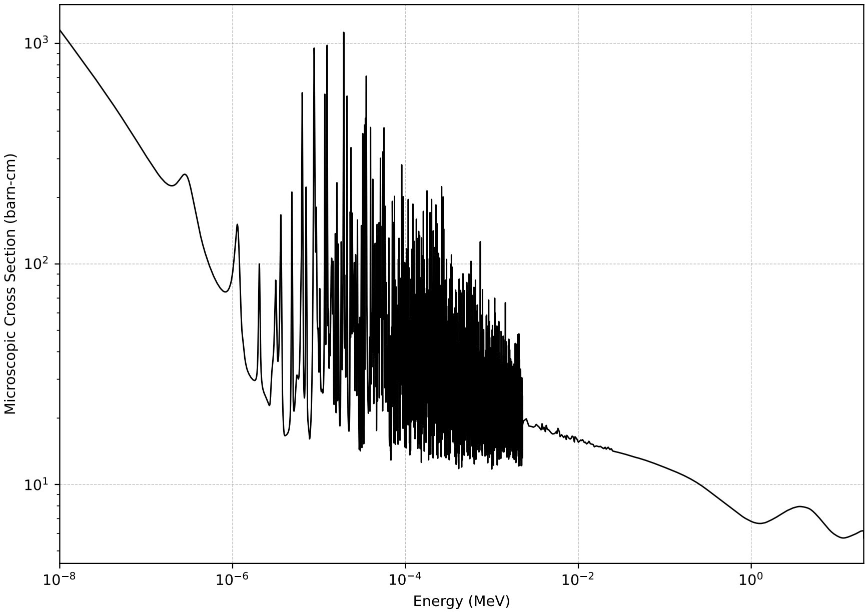

Figure 2.1: Microscopic total cross section for ^{235}U, acquired from ENDF/B-VII.1.

and k is the criticality eigenvalue. Note that in Eq. (2.7), delayed neutron production is included in the fission operator $\mathbf{F}$ by assuming that neutron precursor concentration has reached an equilibrium concetration, such that

$$\mathbf{F}\psi = \frac{1}{4\pi}\left[\int_0^\infty dE'\,\Sigma_f(\vec{r},E'\to E)\phi(\vec{r},E') + \sum_{i=1}^{6}\chi_{d,i}(E)\nu_{d,i}\int_0^\infty dE'\,\Sigma_f(E')\phi(E')\right].$$

Also, in Eq. (2.7), the k eigenvalue scales the fission source term so that the number of neutrons gained and lost are equivalent, ensuring the equation is indeed steady-state. The largest positive eigenvalue is k_{eff}. In nuclear reactors, when $k_{\text{eff}} = 1$ the reactor is critical, meaning that neutron production and destruction are equivalent and the reactor is steady state [6]. When $k_{\text{eff}} > 1$ the reactor is supercritical, meaning the neutron production is greater than neutron destruction, and reactor power is expected to increase after each neutron generation. When $k_{\text{eff}} < 1$ the reactor is subcritical, meaning the neutron production is less than neutron destruction, and reactor power is expected to decrease after each neutron generation.

2.2 The α-Eigenvalue Problem

The transport equation can be expressed as a time-dependent eigenvalue equation, the α-eigenvalue form of the transport equation. The α-eigenvalue equation can be derived by assuming the flux will grow or shrink exponentially over time,

$$\psi(\vec{r}, \hat{\Omega}, E, t) = \psi(\vec{r}, \hat{\Omega}, E, 0)e^{\alpha t} \tag{2.8}$$

By substituting Eq. (2.8) into Eq. (2.1), removing the source term, and diving by $e^{\alpha t}$ we get

$$(\alpha \mathbf{V}^{-1} + \mathbf{H})\psi = (\mathbf{S} + \mathbf{F})\psi \tag{2.9}$$

where $\mathbf{V}^{-1}$ is the inverse speed operator,

$$\mathbf{V}^{-1} = \frac{1}{v(E)} \,,$$

α is an eigenvalue with units of inverse time, and α_0 is the eigenvalue with the largest real component.

In nuclear reactors, if $\text{Re}(\alpha_0) = 0$ the neutron population is not changing and thus the reactor is critical. If $\text{Re}(\alpha_0) > 0$ the neutron population is increasing and thus the reactor is supercritical. If $\text{Re}(\alpha_0) < 0$ the neutron population is decreasing and thus the reactor is subcritical.

The α-eigenvalue is more descriptive than k-eigenvalue because it provides the time rate-of-change of the flux in a reactor.

2.3 Solving the Transport Equation

Throughout the history of nuclear engineering, several methods have been used to solve the transport equation. Analytical methods have been applied to simplified 1D problems. These analytical solutions are mostly used for code verification. Although, recently there has been some success using analytical methods in 3D [7].

In the 1930s, Enrico Fermi used the Monte Carlo method to solve the neutron diffusion equation. Today, the Monte Carlo method has been largely successful at solving the neutron transport equation. The Monte Carlo method can sample neutrons at different locations, energies, and directions from continuous probability distributions, and thus is capable of solving the continuous-energy form of the transport equation, Eq. (2.1) [8]. The only errors introduced by the Monte Carlo method are statistical noise, which are partially mitigated by variance reduction methods [9].

Although the Monte Carlo method is a great tool for many neutron transport simulations, it does have difficulties with certain problem types and quantities of interest. For example, for k- and α-eigenvalue problems, most Monte Carlo codes begin averaging k_{eff} and α_0 even before the eigenvector has converged. In time dependent problems, as smaller and smaller time steps are used, the statistical noise within a time step becomes quite large. Also, Monte Carlo methods tend to undersample the resolved resonance range of the energy domain. With today's tools, it is computationally infeasible to accurately sample the tens of thousands of dips in the neutron spectrum caused by resonances, especially for all locations and angles in a realistic 3D simulation.

Deterministic methods provide other ways to solve the neutron transport equation. An advantage that deterministic methods have over Monte Carlo methods is that a deterministic solution provides the angular flux in all spatial cells without statistical noise. However, deterministic methods have trouble modeling complex geometries, and all phase-space dimensions must be discretized.

The energy domain is particularly difficult to discretize because a small change in neutron energy can cause cross sections to vary by several orders of magnitude. The remainder of this document will present methods for improving runtimes and accuracy for deterministic simulations, with an emphasis on energy- and time-dependent neutron transport.

3. THEORY FOR THE MULTIGROUP METHOD

In this section, we will provide a brief overview of the multigroup (MG) method and how is it applied to time-dependent, k-eigenvalue, and α-eigenvalue problems, in order to build a foundation for theory on the coarse-scattering (CS) method and finite-element with discontiguous-support (FEDS) method.

The MG method groups together neutrons with similar values in energy. Specifically, this is achieved by partitioning the energy domain into groups such that each group consists of an energy interval, and collectively all groups define the entire energy domain [10]. To be explicit, group g is defined as

$$\{E|E \in [E_g, E_{g-1})\} .$$

Note, energy groups are typically indexed from highest to lowest enery:

$$\infty > E_1 > E_2 > \cdots > E_{G-1} > E_G > 0 .$$

Prior to conducting a radiation transport simulation, the MG method requires generating problem-specific MG cross sections. These problem-specific MG cross sections are calculated in order to preserve reaction rates. For group g,

$$\Sigma_g(\vec{r},\hat{\Omega})\psi_g(\vec{r},\hat{\Omega}) = \int\limits_{E_g}^{E_{g-1}} dE\, \Sigma(\vec{r},E)\psi(\vec{r},\hat{\Omega},E)$$

where

$$\psi_g(\vec{r},\hat{\Omega}) = \int\limits_{E_g}^{E_{g-1}} dE\, \psi(\vec{r},\hat{\Omega},E) .$$

Historically, the spatial domain was partitioned into regions, and cross sections were assumed to be constant and independent of angle within each region. Reaction rates are preserved if

$$\Sigma_{i,g}\phi_{i,g} = \int\limits_{E_g}^{E_{g-1}} dE\,\Sigma_i(E)\phi_i(E) \tag{3.1}$$

where $\phi_i(E)$ is the weighting flux for region i and is only estimated by solving the slowing down equation or another simplified transport problem, and $\phi_{i,g}$ is the volume-averaged scalar flux for region i. Equation (3.1) can be easily rearranged to

$$\Sigma_{i,g} = \frac{1}{\phi_{i,g}} \int\limits_{E_g}^{E_{g-1}} dE\,\Sigma_i(E)\phi_i(E)\,.$$

3.1 Derivation of the Multigroup Transport Equation

The MG transport equation can be derived by integrating the transport equation, Eq. (2.1), over all energies, resulting in G coupled equations (one for each group),

$$\begin{cases} \int\limits_{E_1}^{\infty} dE \left[\mathbf{L}\psi = (\mathbf{S}+\mathbf{F})\psi + Q\right] \\ \int\limits_{E_2}^{E_1} dE \left[\mathbf{L}\psi = (\mathbf{S}+\mathbf{F})\psi + Q\right] \\ \vdots \\ \int\limits_{E_G}^{E_{G-1}} dE \left[\mathbf{L}\psi = (\mathbf{S}+\mathbf{F})\psi + Q\right]. \end{cases}$$

These equations are coupled because neutrons can lose or gain energy from nuclear interactions. Thus, a neutron lost from one energy group can become a source in another energy group. The terms in the MG transport equation for group g can be expanded as

$$\int_{E_g}^{E_{g-1}} dE\,\mathbf{L}\psi = \frac{1}{v_g}\frac{\partial \psi_g}{\partial t} + \hat{\Omega}\cdot\nabla\psi_g + \Sigma_{t,g}(\vec{r},t)\psi_g(\vec{r},\hat{\Omega},t)$$

$$\int_{E_g}^{E_{g-1}} dE\,\mathbf{S}\psi = \sum_{g'=1}^{G}\int_{4\pi} d\Omega'\,\Sigma_{s,g'\to g}(\vec{r},\hat{\Omega}'\cdot\hat{\Omega},t)\psi_{g'}(\vec{r},\hat{\Omega}',t)$$

$$\int_{E_g}^{E_{g-1}} dE\,\mathbf{F}\psi = \frac{1}{4\pi}\sum_{g'=1}^{G}\Sigma_{f,g'\to g}(\vec{r},t)\phi_{g'}(\vec{r},t)$$

$$\int_{E_g}^{E_{g-1}} dE\,Q = q_g(\vec{r},E,t) + \sum_{i=1}^{N}\frac{\chi_{d,i,g}}{4\pi}\lambda_i C_i(\vec{r},t)$$

Thus, the expanded form of the MG transport equation is

$$\begin{aligned}\frac{1}{v_g}\frac{\partial \psi_g}{\partial t} + \hat{\Omega}\cdot\nabla\psi_g + \Sigma_{t,g}(\vec{r},t)\psi_g(\vec{r},\hat{\Omega},t) \;&=\\ \sum_{g'=1}^{G}\int_{4\pi} d\Omega'\,\Sigma_{s,g'\to g}(\vec{r},\hat{\Omega}'\cdot\hat{\Omega},t)\psi_{g'}(\vec{r},\hat{\Omega}',t) &+ \frac{1}{4\pi}\sum_{g'=1}^{G}\Sigma_{f,g'\to g}(\vec{r},t)\phi_{g'}(\vec{r},t) +\\ &q_g(\vec{r},E,t) + \sum_{i=1}^{N}\frac{\chi_{d,i,g}}{4\pi}\lambda_i C_i(\vec{r},t)\;. \qquad (3.2)\end{aligned}$$

Furthermore, the MG transport equation is equivalent to the continuous-energy transport equation only if:

$$\psi_g(\vec{r},\hat{\Omega},t) = \int_{E_g}^{E_{g-1}} dE\,\psi(\vec{r},\hat{\Omega},E,t)$$

$$\frac{1}{v_g}\frac{\partial \psi_g(\vec{r},\hat{\Omega},t)}{\partial t} = \int_{E_g}^{E_{g-1}} dE\,\frac{1}{v(E)}\frac{\partial \psi(\vec{r},\hat{\Omega},E,t)}{\partial t}$$

$$\Sigma_{t,g}(\vec{r},t)\psi_g(\vec{r},\hat{\Omega},t) = \int_{E_g}^{E_{g-1}} dE\,\Sigma_t(\vec{r},E,t)\psi(\vec{r},\hat{\Omega},E,t)$$

$$\Sigma_{s,g'\to g}(\vec{r},\hat{\Omega}'\cdot\hat{\Omega},t)\psi_{g'}(\vec{r},\hat{\Omega}',t) = \int_{E_g}^{E_{g-1}} dE \int_{4\pi} d\Omega' \int_{E_{g'}}^{E_{g'-1}} dE'\ \Sigma_s(\vec{r},\hat{\Omega}'\cdot\hat{\Omega},E'\to E,t)\psi(\vec{r},\hat{\Omega}',E',t)$$

$$\Sigma_{f,g'\to g}(\vec{r},t)\phi_{g'}(\vec{r},t) = \int_{E_g}^{E_{g-1}} dE \int_{E_{g'}}^{E_{g'-1}} dE'\ \Sigma_f(\vec{r},E'\to E,t)\phi(\vec{r},E',t)$$

where

$\psi_g(\vec{r},\hat{\Omega},t)$	angular flux for group g
v_g	speed for group g
$\Sigma_{t,g}(\vec{r},t)$	total macroscopic cross section for group g
$\Sigma_{s,g'\to g}(\vec{r},\hat{\Omega}'\cdot\hat{\Omega},t)$	macroscopic scattering cross section from group g' to group g
$\Sigma_{f,g'\to g}(\vec{r},t)$	prompt fission cross section from group g' to group g
$C_i(\vec{r},t)$	concentration of delayed neutron precursor flavor i
λ_i	decay constant for precursor flavor i
$\chi_{d,i,g}$	delayed neutron source into group g for precursor flavor i
$q_g(\vec{r},\hat{\Omega},t)$	extraneous source term for group g

However, since $\psi(\vec{r}, \hat{\Omega}, E, t)$ is not known prior to solving the Eq. (3.2) the terms v_g, $\Sigma_{t,g}$, $\Sigma_{s,g' \to g}$, and $\Sigma_{f,g' \to g}$ must be approximated beforehand.

3.2 Spherical Harmonics

Spherical harmonics $Y_\ell^m(\hat{\Omega})$ are eigenfunctions of the scattering operator [11],

$$\mathbf{S} Y_\ell^m(\hat{\Omega}) = \Sigma_{s,\ell} Y_\ell^m(\hat{\Omega}) \, ,$$

where $\Sigma_{s,\ell}$ is the eigenvalue as well as the moments for scattering:

$$\Sigma_{s,\ell} = \int_{-1}^{1} d\mu_0 \, \Sigma_s(\mu_0) P_\ell(\mu_0) \, ,$$

where $\mu_0 = \hat{\Omega}' \cdot \hat{\Omega}$ and P_ℓ are Legendre polynomials,

$$P_\ell(x) = \frac{1}{2^\ell \, \ell!} \frac{d^\ell}{dx^\ell} \left[(x^2 - 1)^\ell \right] \, .$$

The spherical-harmonic function is defined as

$$Y_\ell^m(\hat{\Omega}) = \begin{cases} (-1)^m \sqrt{2} \sqrt{\frac{2\ell+1}{4\pi} \frac{(\ell-|m|)!}{(\ell+|m|)!}} P_\ell^{|m|}(\mu) \sin(|m|\varphi) & \text{if } m < 0 \\ \sqrt{\frac{2\ell+1}{4\pi}} P_\ell^m(\mu) & \text{if } m = 0 \\ (-1)^m \sqrt{2} \sqrt{\frac{2\ell+1}{4\pi} \frac{(\ell-m)!}{(\ell+m)!}} P_\ell^m(\mu) \cos(m\varphi) & \text{if } m > 0 \, , \end{cases}$$

where μ is cosine of the polar angle, φ is the azimuthal angle, and P_ℓ^m are associated Legendre polynomials,

$$P_\ell^m(x) = (-1)^m (1 - x^2)^{m/2} \frac{d^m}{dx^m} \left[P_\ell(x) \right] \, .$$

Now that we have defined spherical harmonics, we introduce a “moment” operator $\mathbf{M}_\ell^m$:

$$\mathbf{M}_\ell^m f(\hat{\Omega}) = \int\limits_{4\pi} d\Omega \, Y_\ell^m(\hat{\Omega}) f(\hat{\Omega}) \, .$$

Furthermore, we will define the operator $\mathbf{M}_L$ as the collection of all spherical-harmonic moments from the 0^{th} moment up to the L^{th} moments, and the pseudo-inverse operator $\mathbf{M}_L^{-1}$ as

$$f(\hat{\Omega}) \approx \mathbf{M}_L^{-1}\mathbf{M}_L f(\hat{\Omega}) = \sum_{\ell=0}^{L} \frac{2\ell+1}{4\pi} \sum_{m=-\ell}^{+\ell} Y_\ell^m(\hat{\Omega}) \big[\mathbf{M}_\ell^m f(\hat{\Omega})\big] \, .$$

If we let $L \to \infty$, then the spherical-harmonic expansion is exact. Otherwise, $\mathbf{M}_L^{-1}\mathbf{M}_L f(\hat{\Omega})$ is just a L^{th}-order approximation of $f(\hat{\Omega})$. For fission, since it is typically assumed to be isotropic, only the 0^{th} moment is taken and is defined as

$$\mathbf{M}_0 f(\hat{\Omega}) = \int\limits_{4\pi} d\Omega \, f(\hat{\Omega}) \, ,$$

and the pseudo-inverse 0^{th} term as

$$\mathbf{M}_0^{-1}\mathbf{M}_0 f(\hat{\Omega}) = \frac{1}{4\pi}\big[\mathbf{M}_0 f(\hat{\Omega})\big] \, .$$

The first step to computing the spherical-harmonic-expanded source terms for the MG transport equation is to take moments of the angular flux. The ℓ, m moment for group g is

$$\phi_{\ell,g}^m = \mathbf{M}_\ell^m \psi_g(\hat{\Omega}) \, .$$

The spherical-harmonic moments of the angular flux for all G groups is

$$\Phi_{L,G} = \mathbf{M}_L \Psi_G \, .$$

3.3 Matrix Form of the Multigroup Transport Equation

The matrix form of the MG transport equation is defined as,

$$\mathbf{L}_G \Psi_G = \mathbf{M}_L^{-1} \mathbf{S}_{L,G} \Phi_{L,G} + \mathbf{M}_0^{-1} \mathbf{F}_G \Phi_{0,G} + Q_G \;, \tag{3.3}$$

where the MG loss operator for group g is defined as

$$\mathbf{L}_g \Psi_g = \frac{1}{v_g} \frac{\partial \psi_g}{\partial t} + \hat{\Omega} \cdot \nabla \psi_g + \Sigma_{t,g} \psi_g \;,$$

the MG scattering operator for group g is

$$\mathbf{M}_L^{-1} \mathbf{S}_{L,g} \Phi_{L,g} = \sum_{\ell=0}^{L} \frac{2\ell+1}{4\pi} \sum_{m=-\ell}^{+\ell} Y_\ell^m(\hat{\Omega}) \sum_{g'=1}^{G} \Sigma_{s,\ell,g' \to g} \phi_{\ell,g}^m \;,$$

the fission operator for group g is

$$\mathbf{M}_0^{-1} \mathbf{F}_g \Phi_{0,g} = \frac{1}{4\pi} \sum_{g'=1}^{G} \Sigma_{f,g' \to g} \phi_{0,g} \;,$$

and the extraneous source term for group g is

$$Q_g = q_g(\vec{r}, t) + \sum_{i=1}^{N} \frac{\chi_{d,i,g}}{4\pi} \lambda_i C_i(\vec{r}, t) \;.$$

It should be noted that the MG loss operator $\mathbf{L}_G$ is difficult to invert, so Eq. (3.3) is typically solved by lagging the production terms (the right-hand side of the equation). Also, when a large number of groups is used, the size of the scattering transfer matrix becomes massive. However, the scattering transfer matrix is also sparse and well-suited for reduced-order modeling approaches.

4. EIGENVALUE ALGORITHMS FOR MULTIGROUP EQUATIONS

4.1 Solving the k-Eigenvalue Equation

The k-eigenvalue transport equation, Eq. (2.7), can be written in MG form as

$$\mathbf{H}_G \Psi_G = \mathbf{M}_L^{-1} \mathbf{S}_{L,G} \Phi_{L,G} + \frac{1}{k} \mathbf{M}_0^{-1} \mathbf{F}_G \Phi_{0,G} \,.$$

The k-eigenvalue equation can be solved iteratively using the Power method, also known as von Mises iterations [12]. Namely, the steps for solving (4.1) are:

Step 1: Solve the MG transport equation for $\Psi_G^{(i+1)}$ by lagging the right-hand-side:

$$\mathbf{H}_G \Psi_G^{(i+1)} = \mathbf{M}_L^{-1} \mathbf{S}_{L,G} \Phi_{L,G}^{(i)} + \frac{1}{k_{\text{eff}}^{(i)}} \mathbf{M}_0^{-1} \mathbf{F}_G \Phi_{0,G}^{(i)} \,,$$

where the superscript (i) is used to indicate iteration number.

Step 2: Compute flux moments:

$$\Phi_{L,G}^{(i+1)} = \mathbf{M}_L \Psi_G^{(i+1)} \,.$$

Step 3: Compute the eigenvalue:

$$k_{\text{eff}}^{(i+1)} = k_{\text{eff}}^{(i)} \frac{||\mathbf{F}_G \Phi_{0,G}^{(i+1)}||}{||\mathbf{F}_G \Phi_{0,G}^{(i)}||} \,,$$

where $||\cdot||$ is a norm over space and energy.

Step 4: Normalize flux moments before starting the next iteration:

$$\Phi_{L,G}^{(i+1)} = \frac{\Phi_{L,G}^{(i+1)}}{||\Phi_{0,G}^{(i+1)}||} \,.$$

Repeat Steps 1 through 4 for each iteration until the convergence criteria is met.

4.2 Solving the α-Eigenvalue equation

The α-eigenvalue transport equation, Eq. (2.9), can be written in MG form as

$$(\alpha \mathbf{V}_G^{-1} + \mathbf{H}_G)\Psi_G = \mathbf{M}_L^{-1}\mathbf{S}_{L,G}\Phi_{L,G} + \mathbf{M}_0^{-1}\mathbf{F}_G\Phi_{0,G} \,.$$

The α-eigenvalue equation can be solved iteratively using the Rayleigh Quotient method [13]. Namely, the steps for solving (4.2) are:

Step 1: Solve the MG transport equation for $\Psi_G^{(i+1)}$ by lagging the right-hand-side:

$$\begin{cases} (\alpha^{(i)}\mathbf{V}_G^{-1} + \mathbf{H}_G)\Psi_G^{(i+1)} = \mathbf{M}_L^{-1}\mathbf{S}_{L,G}\Phi_{L,G}^{(i)} + \mathbf{M}_0^{-1}\mathbf{F}_G\Phi_{0,G}^{(i)} & \text{for} \quad \alpha_0^{(i)} > 0 \\ \mathbf{H}_G\Psi_G^{(i+1)} = -\alpha^{(i)}\mathbf{V}_G^{-1}\Psi_G^{(i)} + \mathbf{M}_L^{-1}\mathbf{S}_{L,G}\Phi_{L,G}^{(i)} + \mathbf{M}_0^{-1}\mathbf{F}_G\Phi_{0,G}^{(i)} & \text{for} \quad \alpha_0^{(i)} < 0 \end{cases}$$

Step 2: Update the eigenvalue via the Rayleigh Quotient method:

$$\begin{cases} \alpha^{(i+1)} = \alpha^{(i)} + \frac{\langle \Psi_G^{(i+1)}, (\mathbf{M}_L^{-1}\mathbf{S}_{L,G}\Delta\Phi_{L,G}^{(i+1)} + \mathbf{M}_0^{-1}\mathbf{F}_G\Delta\Phi_{0,G}^{(i+1)})\rangle}{\langle \Psi_G^{(i+1)}, \mathbf{V}_G^{-1}\Psi_G^{(i+1)}\rangle} & \text{for} \quad \alpha_0^{(i)} > 0 \\ \alpha^{(i+1)} = \frac{\langle \Psi_G^{(i+1)}, (\mathbf{M}_L^{-1}\mathbf{S}_{L,G}\Delta\Phi_{L,G}^{(i+1)} + \mathbf{M}_0^{-1}\mathbf{F}_G\Delta\Phi_{0,G}^{(i+1)} - \alpha^{(i)}\mathbf{V}_G^{-1}\Psi_G^{(i)})\rangle}{\langle \Psi_G^{(i+1)}, \mathbf{V}_G^{-1}\Psi_G^{(i+1)}\rangle} & \text{for} \quad \alpha_0^{(i)} < 0 \end{cases}$$

where

$$\Delta\Phi_{L,G}^{(i+1)} = \Phi_{L,G}^{(i+1)} - \Phi_{L,G}^{(i)}$$

$$\Delta\Phi_{0,G}^{(i+1)} = \Phi_{0,G}^{(i+1)} - \Phi_{0,G}^{(i)} \,,$$

and $\langle \cdot , \cdot \rangle$ is an inner product over space, angle and energy. Repeat Steps 1 and 2 for each iteration, until the convergence criteria is met.

5. THEORY FOR THE COARSE-SCATTERING METHOD

In this dissertation, we introduce the coarse-scattering method (CS), an approach that reduces simulation runtimes required to model scattering in multigroup (MG) codes. The purpose of the CS method is to reduce the size of group-to-group transfer matrices by lumping multiple energy groups, g, together into coarse energy elements, e, such that

$$g \subset e \, .$$

This enables us to make the following substitutions to the scattering and fission operators in the MG transport equation:

$$\sum_{g'=1}^{G} \Sigma_{s,\ell,g'\to g} \phi_{\ell,g'}^{m} \quad \to \quad S_{\ell,e\to g}^{m} \sum_{e'=1}^{E} \Sigma_{s,\ell,e'\to e} \phi_{\ell,e'}^{m} \, , \tag{5.1}$$

$$\sum_{g'=1}^{G} \Sigma_{f,g'\to g} \phi_{0,g'} \quad \to \quad F_{e\to g} \sum_{e'=1}^{E} \Sigma_{f,e'\to e} \phi_{0,e'} \, , \tag{5.2}$$

where

$$S_{\ell,e\to g}^{m} = \frac{\sum_{g'=1}^{G} \Sigma_{s,\ell,g'\to g} \phi_{\ell,g'}^{m}}{\sum_{e'=1}^{E} \Sigma_{s,\ell,e'\to e} \phi_{\ell,e'}^{m}} \tag{5.3}$$

$$F_{e\to g} = \frac{\sum_{g'=1}^{G} \Sigma_{f,g'\to g} \phi_{0,g'}}{\sum_{e'=1}^{E} \Sigma_{f,e'\to e} \phi_{0,e'}} \tag{5.4}$$

$$\phi_{\ell,e}^{m} = \sum_{g\in e} \phi_{\ell,g}^{m} \, . \tag{5.5}$$

and

$S^m_{\ell,e\to g}$	CS scattering spectrum
$F_{e\to g}$	CS fission spectrum
$\Sigma_{s,\ell,g'\to g}$	group-to-group scattering matrix for the ℓ^{th}-Legendre moment
$\Sigma_{f,\ell,g'\to g}$	group-to-group fission matrix
$\Sigma_{s,\ell,e'\to e}$	coarse-element-to-coarse-element scattering matrix
$\Sigma_{f,e'\to e}$	coarse-element-to-coarse-element fission matrix
$\phi^m_{\ell,g'}$	ℓ^{th} flux moment for energy group g'
$\phi^m_{\ell,e'}$	ℓ^{th} flux moment for energy coarse-element e' .

The coarse-scattering and coarse-fission transfer matrices can be computed prior to the simulation by using an estimate of the group flux φ_g as a weighting spectrum

$$\Sigma_{s,\ell,e'\to e} = \frac{1}{\varphi_{e'}} \sum_{g\in e} \sum_{g'\in e'} \Sigma_{s,\ell,g'\to g}\varphi_{g'} \ ,$$

$$\Sigma_{f,e'\to e} = \frac{1}{\varphi_{e'}} \sum_{g\in e} \sum_{g'\in e'} \Sigma_{f,g'\to g}\varphi_{g'} \ .$$

If a flat flux is simply used as the weighting spectrum, this simplifies to

$$\Sigma_{s,\ell,e'\to e} = \sum_{g\in e} \sum_{g'\in e'} \Sigma_{s,\ell,g'\to g} \ ,$$

$$\Sigma_{f,e'\to e} = \sum_{g\in e} \sum_{g'\in e'} \Sigma_{f,g'\to g} \ .$$

5.1 Matrix Form of the Coarse-Scattering Method

A fine-grid-to-coarse-grid mapping matrix $C_{G\to E}$, of size $G \times E$ consisting of zeroes and ones, can be used to map fluxes onto a coarse grid:

$$\Phi^m_{\ell,E} = C_{G\to E}\Phi^m_{\ell,G} \ ,$$

Similarly, the scattering and fission matrices can easily be mapped onto the coarse grid too by assuming a flat weighting spectrum, producing matrices of size $E \times E$:

$$S_{\ell,E} = C_{G\to E}S_{\ell,G}C^T_{G\to E} \ ,$$

$$F_E = C_{G\to E}F_G C^T_{G\to E} \ ,$$

where T represents the transpose of the matrix. Also, the CS scattering and fission spectra, previously defined in Eq. (5.3) and Eq. (5.4), can be written as matrices of size $G \times E$:

$$\mathbf{S}^m_{\ell,E\to G} = \mathbf{S}^m_{\ell,G}\Phi^m_{\ell,G} \otimes (\mathbf{1} \oslash \mathbf{S}^m_{\ell,E}\Phi^m_{\ell,E})^T \odot C^T_{G\to E}$$

$$\mathbf{F}_{E\to G} = \mathbf{F}_G\Phi_{0,G} \otimes (\mathbf{1} \oslash \mathbf{F}_E\Phi_{0,E})^T \odot C^T_{G\to E}$$

where $\otimes$ is the Kronecker product operator, $\mathbf{1}$ is a vector of ones, $\oslash$ is the Hadamard division operator, and $\odot$ is the Hadamard product operator.

Thereby, the matrix form of the CS transport equation is:

$$\mathbf{L}_G\Psi_G = \mathbf{M}_L^{-1}\mathbf{S}_{L,E\to G}\mathbf{S}_{L,E}\Phi_{L,E} + \frac{1}{k_{\text{eff}}}\mathbf{M}_0^{-1}\mathbf{F}_{E\to G}\mathbf{F}_E\Phi_{0,E}$$

where, for a single group g:

$$\mathbf{L}_g \Psi_g = \frac{1}{v_g}\frac{\partial \psi_g}{\partial t} + \hat{\Omega}\cdot\nabla\psi_g + \Sigma_{t,g}\psi_g$$

$$\mathbf{M}_L^{-1}\mathbf{S}_{L,e\to g}\mathbf{S}_{L,e}\Phi_{L,e} = \sum_{\ell=0}^{L}\sum_{m=-\ell}^{+\ell}\frac{2\ell+1}{4\pi}Y_\ell^m(\hat{\Omega})S^m_{\ell,e\to g}\sum_{e'=1}^{E}\Sigma_{s,\ell,e'\to e}\phi^m_{\ell,e'}$$

$$\mathbf{M}_0^{-1}\mathbf{F}_{e\to g}\mathbf{F}_e\Phi_{0,e} = \frac{1}{4\pi}F_{e\to g}\sum_{e'=1}^{E}\Sigma_{f,e'\to e}\phi_{0,e'}$$

$$\phi^m_{\ell,e} = \sum_{g\in e}\int_{4\pi} d\Omega\,\psi_g Y_\ell^m(\hat{\Omega})\,.$$

Figure 5.1 shows an example of a MG transfer matrix that was collapsed into a CS transfer matrix.

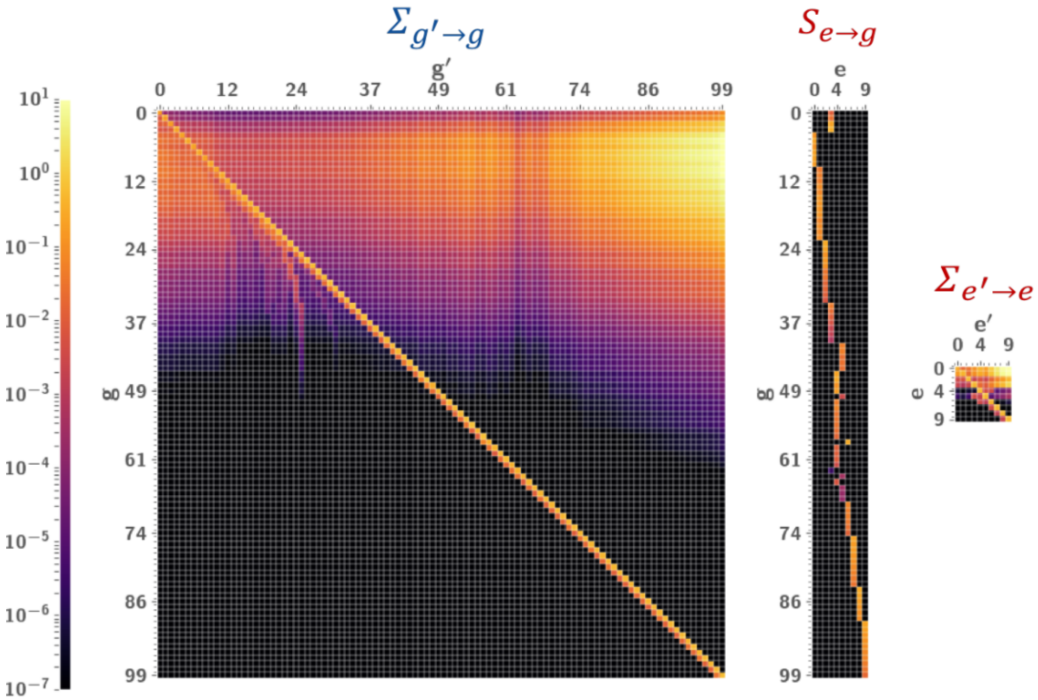

Figure 5.1: Example of a MG transfer matrix that was condensed into a CS transfer matrix.

5.2 Eigenvalue Algorithms using the Coarse-Scattering Method

In order for CS to converge to the same solution as MG, it is necessary to recompute the $\mathbf{S}_{\ell,e\to g}$ and $\mathbf{F}_{e\to g}$ during source iterations. However, note that $\mathbf{S}_{\ell,e\to g}$ and $\mathbf{F}_{e\to g}$ may not vary significantly from one iteration to the next, therefore it's not necessary to recompute both $\mathbf{S}_{\ell,e\to g}$ and $\mathbf{F}_{e\to g}$ every single iteration.

The asymptotic computational cost of solving the MG transport equation is order G^2 per iteration. However, for CS, the asymptotic computational cost is only order G^2 only in iterations when $\mathbf{S}_{\ell,e\to g}$ and $\mathbf{F}_{e\to g}$ are recomputed. Thus, if the CS method is applied appropriately it can reduce the overall runtime of a simulation.

5.3 Solving the Coarse-Scattering k-Eigenvalue Equation

The k-eigenvalue CS transport equation is

$$\mathbf{H}_G\Psi_G = \mathbf{M}_L^{-1}\mathbf{S}_{L,E\to G}\mathbf{S}_{L,E}\Phi_{L,E} + \frac{1}{k_{\text{eff}}}\mathbf{M}_0^{-1}\mathbf{F}_{E\to G}\mathbf{F}_E\Phi_{0,E}\ . \tag{5.6}$$

The k-eigenvalue equation can be solved iteratively using the Power method. Namely, the steps for solving Eq. (5.6) are:

Step 1: Solve the MG transport equation for $\Psi_G^{(i+1)}$ by lagging the right-hand-side:

$$\mathbf{H}_G\Psi_G^{(i+1)} = \mathbf{M}_L^{-1}\mathbf{S}^{(i)}_{L,E\to G}\mathbf{S}_{L,E}\Phi^{(i)}_{L,E} + \frac{1}{k^{(i)}_{\text{eff}}}\mathbf{M}_0^{-1}\mathbf{F}^{(i)}_{E\to G}\mathbf{F}_E\Phi^{(i)}_{0,E}\ .$$

Step 2: Compute the fine and coarse flux moments:

$$\Phi^{(i+1)}_{L,G} = \mathbf{M}_L\Psi^{(i+1)}_G\ , \qquad \Phi^{(i+1)}_{L,E} = C_{G\to E}\Phi^{(i+1)}_{L,G}\ .$$

Step 3: Update CS scattering and fission spectra:

$$\mathbf{S}^{m}_{\ell,E\to G}{}^{(i+1)} = \begin{cases} \mathbf{S}^{m}_{\ell,G}\Phi^{m,(i+1)}_{\ell,G} \otimes (\mathbf{1} \oslash \mathbf{S}^{m}_{\ell,E}\Phi^{m,(i+1)}_{\ell,E})^{T} \odot C^{T}_{G\to E} & \text{if } (i+1) \text{ is divisible by } r_{\mathbf{S}} \\ \mathbf{S}^{m}_{\ell,E\to G}{}^{(i)} & \text{otherwise} \end{cases}$$

$$\mathbf{F}^{(i+1)}_{E\to G} = \begin{cases} \mathbf{F}_{G}\Phi^{(i+1)}_{0,G} \otimes (\mathbf{1} \oslash \mathbf{F}_{E}\Phi^{(i+1)}_{0,E})^{T} \odot C^{T}_{G\to E} & \text{if } (i+1) \text{ is divisible by } r_{\mathbf{F}} \\ \mathbf{F}^{(i)}_{E\to G} & \text{otherwise} \end{cases}$$

where $r_{\mathbf{S}}$ and $r_{\mathbf{F}}$ are integers that control how frequently the CS scattering and fission spectra are recomputed.

Step 4: Compute the eigenvalue:

$$k^{(i+1)}_{\text{eff}} = k^{(i)}_{\text{eff}} \frac{||\mathbf{F}_{E}\Phi^{(i+1)}_{0,E}||}{||\mathbf{F}_{E}\Phi^{(i)}_{0,E}||} \, .$$

where $||\cdot||$ is a norm over space and energy.

Step 5: Normalize the coarse flux moments before starting the next iteration:

$$\Phi^{(i+1)}_{L,E} = \frac{\Phi^{(i+1)}_{L,E}}{||\Phi^{(i+1)}_{0,E}||} \, .$$

Repeat Steps 1 through 5 for each iteration until the convergence criteria is met.

5.4 Solving the Coarse-Scattering α-Eigenvalue Equation

The α-eigenvalue CS transport equation is

$$(\alpha\mathbf{V}^{-1}_{G} + \mathbf{H}_{G})\Psi_{G} = \mathbf{M}^{-1}_{L}\mathbf{S}_{L,E\to G}\mathbf{S}_{L,E}\Phi_{L,E} + \mathbf{M}^{-1}_{0}\mathbf{F}_{E\to G}\mathbf{F}_{E}\Phi_{0,E} \, . \tag{5.7}$$

The α-eigenvalue equation can be solved iteratively using the Rayleigh Quotient method [13]. Namely, the steps for solving Eq. (5.7) are:

Step 1: Solve the MG transport equation for $\Psi_G^{(i+1)}$ by lagging the right-hand-side:

$$\begin{cases} (\alpha_0^{(i)}\mathbf{V}_G^{-1} + \mathbf{H}_G)\Psi_G^{(i+1)} = \mathbf{M}_L^{-1}\mathbf{S}_{L,E\to G}\mathbf{S}_{L,E}\Phi_{L,E}^{(i)} + \mathbf{M}_0^{-1}\mathbf{F}_{E\to G}\mathbf{F}_E\Phi_{0,E}^{(i)} & \text{for } \alpha_0^{(i)} > 0 \\ \mathbf{H}_G\Psi_G^{(i+1)} = -\alpha_0^{(i)}\mathbf{V}_G^{-1}\Psi_G^{(i)} + \mathbf{M}_L^{-1}\mathbf{S}_{L,E\to G}\mathbf{S}_{L,E}\Phi_{L,E}^{(i)} + \mathbf{M}_0^{-1}\mathbf{F}_{E\to G}\mathbf{F}_E\Phi_{0,E}^{(i)} & \text{for } \alpha_0^{(i)} < 0 \end{cases}$$

Step 2: Compute the fine and coarse flux moments:

$$\Phi_{L,G}^{(i+1)} = \mathbf{M}_L\Psi_G^{(i+1)}\,, \qquad \Phi_{L,E}^{(i+1)} = C_{G\to E}\Phi_{L,G}^{(i+1)}\,.$$

Step 3: Update CS scattering and fission spectra:

$$\mathbf{S}_{\ell,E\to G}^{m}{}^{(i+1)} = \begin{cases} \mathbf{S}_{\ell,G}^{m}\Phi_{\ell,G}^{m,(i+1)} \otimes (\mathbf{1} \oslash \mathbf{S}_{\ell,E}^{m}\Phi_{\ell,E}^{m,(i+1)})^T \odot C_{G\to E}^T & \text{if } (i+1) \text{ is divisible by } r_{\mathbf{S}} \\ \mathbf{S}_{\ell,E\to G}^{m}{}^{(i)} & \text{otherwise} \end{cases}$$

$$\mathbf{F}_{E\to G}^{(i+1)} = \begin{cases} \mathbf{F}_G\Phi_{0,G}^{(i+1)} \otimes (\mathbf{1} \oslash \mathbf{F}_E\Phi_{0,E}^{(i+1)})^T \odot C_{G\to E}^T & \text{if } (i+1) \text{ is divisible by } r_{\mathbf{F}} \\ \mathbf{F}_{E\to G}^{(i)} & \text{otherwise} \end{cases}$$

where $r_{\mathbf{S}}$ and $r_{\mathbf{F}}$ are integers that control how frequently the CS scattering and fission spectra are recomputed, and $\langle\,\cdot\,,\,\cdot\,\rangle$ is an inner product over space, angle and energy.

Step 4: Update the eigenvalue via the Rayleigh Quotient method:

$$\begin{cases} \alpha_0^{(i+1)} = \alpha_0^{(i)} + \frac{\langle\Psi_G^{(i+1)}, (\mathbf{M}_L^{-1}\mathbf{S}_{L,E\to G}^{(i+1)}\mathbf{S}_{L,E}\Delta\Phi_{L,E}^{(i+1)} + \mathbf{M}_0^{-1}\mathbf{F}_{E\to G}^{(i+1)}\mathbf{F}_E\Delta\Phi_{0,E}^{(i+1)})\rangle}{\langle\Psi_G^{(i+1)}, \mathbf{V}_G^{-1}\Psi_G^{(i+1)}\rangle} & \text{for} \quad \alpha_0^{(i)} > 0 \\ \alpha_0^{(i+1)} = \frac{\langle\Psi_G^{(i+1)}, (\mathbf{M}_L^{-1}\mathbf{S}_{L,E\to G}^{(i+1)}\mathbf{S}_{L,E}\Delta\Phi_{L,E}^{(i+1)} + \mathbf{M}_0^{-1}\mathbf{F}_{E\to G}^{(i+1)}\mathbf{F}_E\Delta\Phi_{0,E}^{(i+1)} - \alpha^{(i)}\mathbf{V}_G^{-1}\Psi_G^{(i)})\rangle}{\langle\Psi_G^{(i+1)}, \mathbf{V}_G^{-1}\Psi_G^{(i+1)}\rangle} & \text{for} \quad \alpha_0^{(i)} < 0 \end{cases}$$

where

$$\Delta\Phi_{L,E}^{(i+1)} = \Phi_{L,E}^{(i+1)} - \Phi_{L,E}^{(i)}$$

$$\Delta\Phi_{0,E}^{(i+1)} = \Phi_{0,E}^{(i+1)} - \Phi_{0,E}^{(i)}\,.$$

5.5 Particle Balance for the Coarse-Scattering Method

We start by defining the residual ρ as the following norm,

$$\rho = ||(\mathbf{M}_L^{-1}\mathbf{S}_{L,G} + \mathbf{M}_0^{-1}\mathbf{F}_G)\Phi_{L,G} - (\mathbf{M}_L^{-1}\mathbf{S}_{L,E\to G}\mathbf{S}_{L,E} + \mathbf{M}_0^{-1}\mathbf{F}_{E\to G}\mathbf{F}_E)\Phi_{L,E}|| \, . \quad (5.8)$$

Particle balance is maintained if the residual in the last iteration $\rho^{(i+1)}$ is less than machine epsilon. Thus, in order to ensure particle balance, we simply have to recompute $\mathbf{S}_{L,E\to G}$ and $\mathbf{F}_{E\to G}$ in the last iteration, because then Eq. (5.8) will equal zero.

6. COARSE-SCATTERING TEST PROBLEM: A SLAB OF HIGHLY-ENRICHED URANIUM

In this section, we used a bare slab of highly-enriched uranium (HEU) as a test problem to study the improvement in simulation runtime that coarse-scattering (CS) method can provide. Since HEU is a high-Z material, it will barely moderate any neutrons down to thermal energies. Thus, most neutrons will have high kinetic energies including those causing fissions, hence the kinetic energy of neutrons causing fission is not negligible. For this problem, a fission matrix is necessary to accurately model fission, because the spectrum of neutron energies emitted from fission reactions will depend on the energy of the incident neutrons. This allows us to apply CS method to fission as well, and study it's impact on simulation runtime.

When the CS method was used, the simulations required more Power iterations to converge, however they required significantly less computational time per iteration, and thus less computational time over all.

6.1 Description of the Coarse-Scattering Test Problem

This test problem consists of an 8 cm slab of highly-enriched uranium (HEU) with a density of 18.74 g/cm^3 at room temperature (293.6 K), with vacuums on the left and right boundaries. The composition of the HEU is shown in Table 6.1.

Table 6.1: Isotopic composition of HEU.

Isotope	Number Density ($\frac{\text{nuclei}}{\text{barn-cm}}$)
^{234}U	4.9184×10^{-4}
^{235}U	4.4994×10^{-2}
^{238}U	2.4984×10^{-3}

The cross sections for HEU were extracted from the United States' Evaluated Nuclear Data Library B-VII.1 (ENDF/B-VII.1) [14], and post-processed with the NJOY Nuclear Data Processing System, Version 2016 (NJOY2016) [15] in order to create MG cross sections. The MG discretization consisted of logarithmically-spaced energy groups.

The quantity of interest for this problem was criticality, k_{eff}, for the HEU slab. The discrete-ordinates (S_N) method was used for the k-eigenvalue calculations. The 8 cm slab was discretized into 20 equally spaced spatial cells with diamond-difference discretization. The angular domain was discretized into 32 polar angles, and Gauss-Legendre quadrature was used for scattering. For a simulation with isotropic scattering and 1000 fine groups, k_{eff} was computed to be $1.19072 \pm 10^{-}5$. For a simulation with anisotropic scattering modeled using a third-order Legendre polynomial expansion and 1000 fine groups, k_{eff} was computed to be $1.11910 \pm 10^{-}5$.

Several runtime comparisons were conducted with this problem. The purpose was to determine when CS provides the greatest reduction in runtime compared to standard MG.

6.2 Runtime Comparison 1: Varying the Number of Coarse Elements

In this study, we ran several CS k-eigenvalue calculations, using the Power iterations, until the error was less than 10^{-5} for criticality, k_{eff}, and flux, ϕ. For each simulation, we used 1000 fine groups, but varied the number of coarse elements from 1 to 250 coarse elements to determine which number of coarse elements provides the greatest reduction in simulation runtime. For these simulations, we assumed isotropic scattering, we recomputed $\mathbf{S}_{0,e\to g}$ every 3 iterations, and we recomputed $\mathbf{F}_{e\to g}$ every 12 iterations. Figure 6.1 shows simulation runtimes for the simulations with varying numbers of coarse elements. All the simulations converge to the same result (within the convergence tolerances for k_{eff} and ϕ). The greatest reduction in runtime was achieved when 50 coarse elements were used.

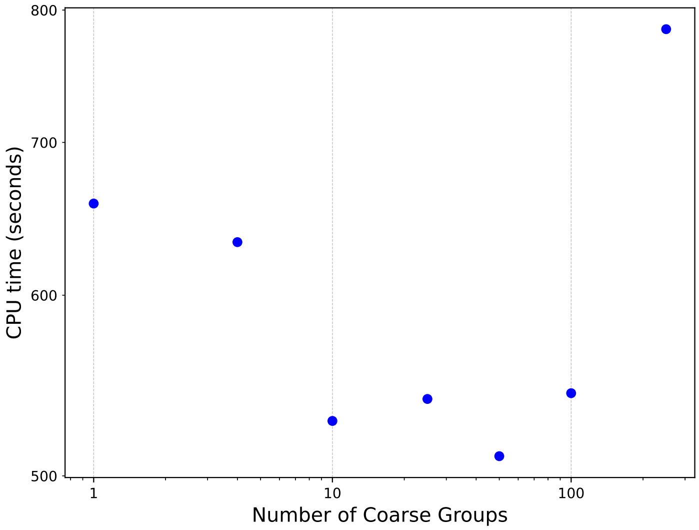

Figure 6.1: Comparison of CPU times for simulations 1000 fine groups, but with different number of coarse elements in each simulation.

Figure 6.2 shows the error in the flux as a function of iteration (left) and as a function of runtime (right). Using the CS method may require more iterations to converge, however each iteration requires far less computational time, which results in a shorter total runtime.

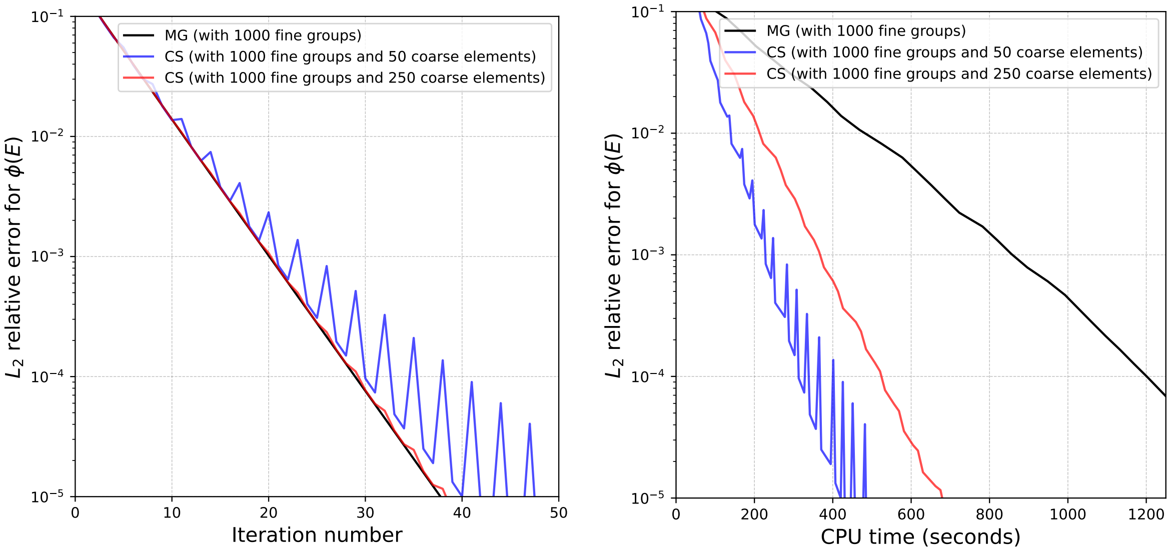

Figure 6.2: The L_2 error norm of the neutron flux as a function of iteration (left) and as a function of runtime (right). Note, each CS iteration requires less CPU time.

6.3 Runtime Comparison 2: Varying the Frequency of CS Fission Spectrum Recomputations

In this study, we ran several CS k-eigenvalue calculations, using the Power iterations, until the error was less than 10^{-5} for criticality, k_{eff}, and flux, ϕ. For each simulation, we used 1000 fine groups and 50 coarse elements. We also assumed isotropic scattering and recomputed $\mathbf{S}_{0,e\to g}$ every 3 iterations. This time we varied the frequency of $\mathbf{F}_{e\to g}$ recomputations, from recomputing $\mathbf{F}_{e\to g}$ every 3 iterations to recomputing $\mathbf{F}_{e\to g}$ every 60 iterations. Figure 6.3 shows simulation runtimes for the CS simulations with different frequencies of $\mathbf{F}_{e\to g}$ recomputations. We found that recomputing $\mathbf{F}_{e\to g}$ every 36 iterations provided the greatest reduction in runtime compared to standard MG. This result was expected because the fission spectrum should not change much from one iteration to the next.

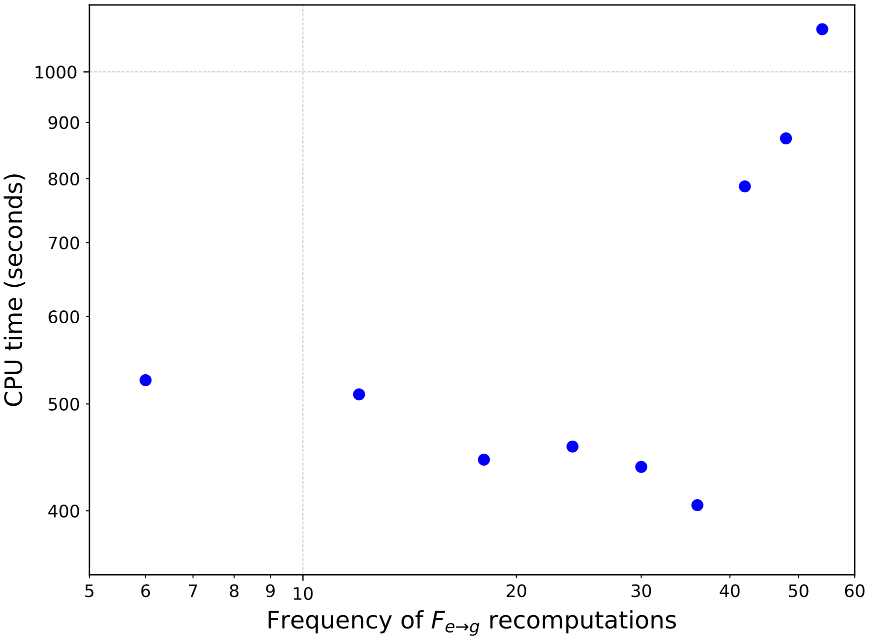

Figure 6.3: Comparison of simulation runtimes with different frequencies of $\mathbf{F}_{e\to g}$ recomputations.

6.4 Runtime Comparison 3: Varying the Frequency of CS Scattering Spectrum Recomputations

In this study, we ran several CS k-eigenvalue calculations, using the Power iterations, until the error was less than 10^{-5} for criticality, k_{eff}, and flux, ϕ. For each simulation, we used 1000 fine groups and 50 coarse elements. We recomputed $\mathbf{F}_{e\to g}$ every 18 iterations. However, this time we varied the frequency of $\mathbf{S}_{0,e\to g}$ recomputations, from recomputing $\mathbf{S}_{0,e\to g}$ every single iteration to recomputing $\mathbf{S}_{0,e\to g}$ every 7 iterations. Figure 6.4 shows simulation runtimes for the CS simulations with different frequencies of $\mathbf{S}_{0,e\to g}$ recomputations. We found that recomputing $\mathbf{S}_{0,e\to g}$ every 3 iterations provided the greatest reduction in runtime compared to standard MG.

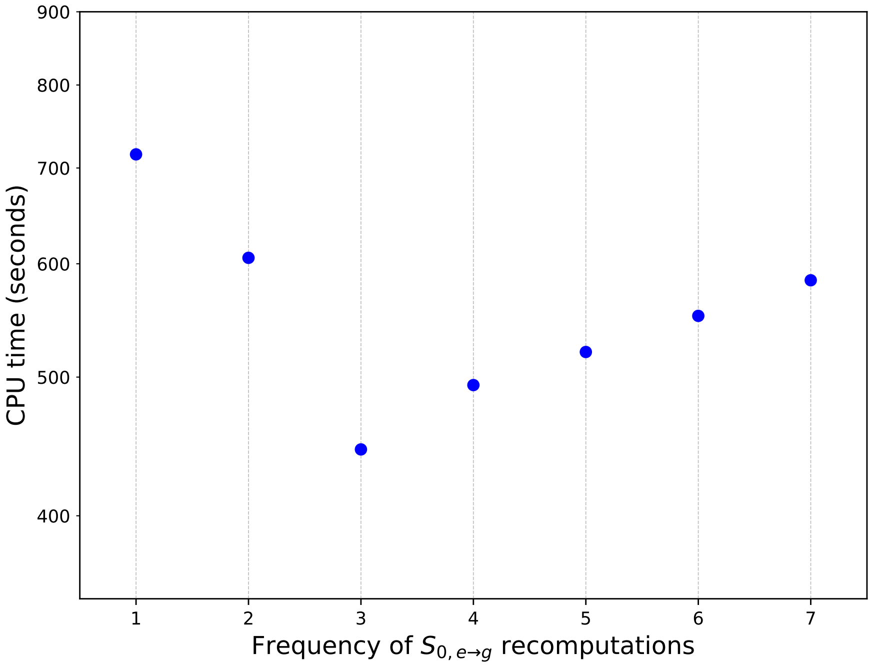

Figure 6.4: Comparison of simulation runtimes with different frequencies of $\mathbf{S}_{0,e\to g}$ recomputations.

6.5 Runtime Comparison 4: Varying the Number of Fine Groups

In this study, we ran several MG simulations and CS simulations until the error for k_{eff} and ϕ was less than 10^{-5} in each simulation. This time we varied the number of fine groups from 100 fine groups up to 1000 fine groups, and compared the difference in simulation runtimes between the standard MG simulations and the CS simulations. For the each of the CS simulations, we used 50 coarse elements. We also assumed isotropic scattering, recomputed $\mathbf{S}_{0,e\to g}$ every 3 iterations, and recomputed $\mathbf{F}_{e\to g}$ every 18 iterations. Figure 6.5 compares the simulation runtimes for CS and MG, for various numbers of fine groups. Notice that as more fine groups are used there is a greater reduction in simulation runtime between standard MG method and the CS method. Figure 6.6 shows the reduction in runtime compared to MG simulation, specifically, it plots the MG runtime divided by the CS runtime for an equivalent simulation. For 1000 fine groups, the CS simulation ran

3.9 times faster than the MG simulation.

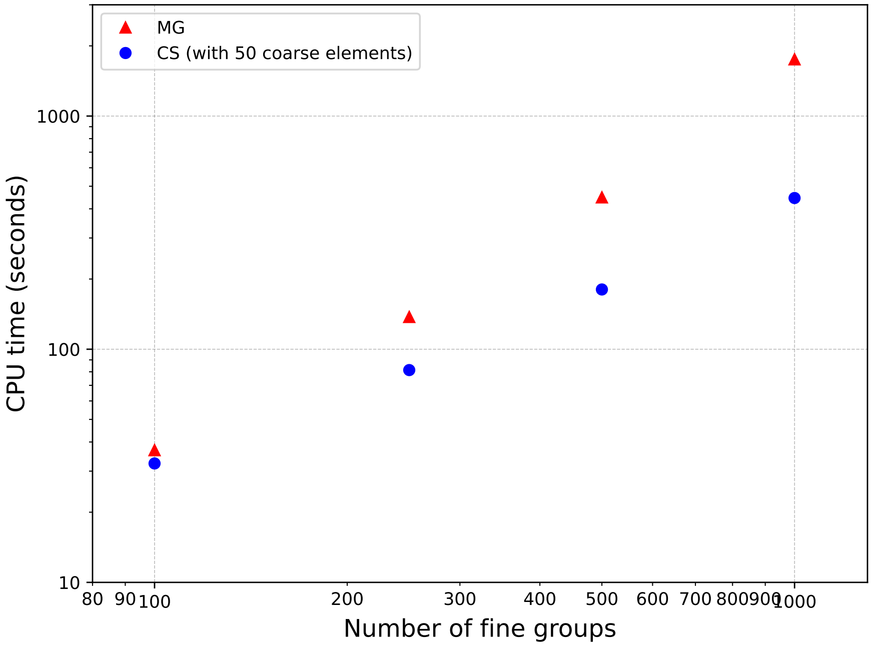

Figure 6.5: Comparison of simulation runtimes, for simulations with isotropic scattering, with different numbers of fine groups.

We also conducted a similar study, but this time using anisotropic scattering modeled using a third-order Legendre polynomial expansion (P_3-scattering). We still used 50 coarse elements, recomputed $\mathbf{S}_{0,e\to g}$ every 3 iterations, and recomputed $\mathbf{F}_{e\to g}$ every 18 iterations. However, we recomputed $\mathbf{S}_{1,e\to g}$ every 9 iterations, and recomputed $\mathbf{S}_{2,e\to g}$ and $\mathbf{S}_{3,e\to g}$ every 18 iterations. Figure 6.7 shows the simulation runtimes for CS and MG for various numbers of fine groups. For 1000 fine groups, the CS simulation ran 3.2 times faster than the MG simulation.

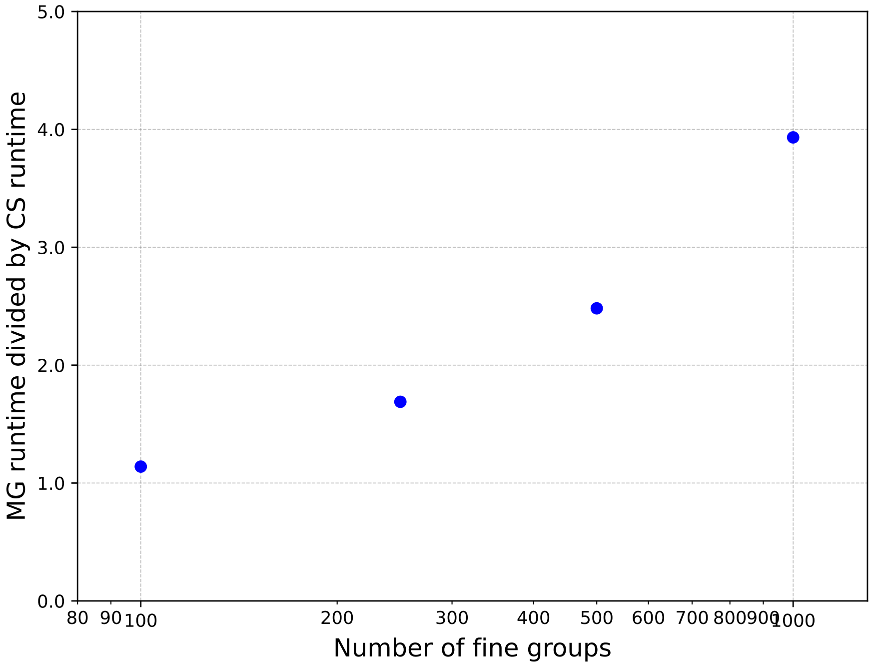

Figure 6.6: Reduction in runtime, for simulations with isotropic scattering, with different numbers of fine groups.

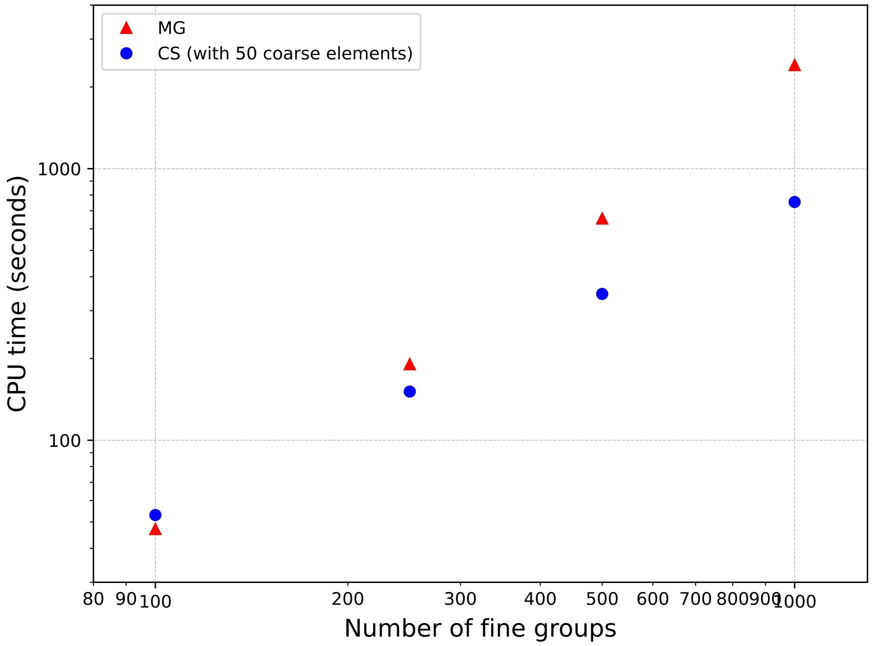

Figure 6.7: Comparison of simulation runtimes, for simulations with P_3-scattering, with different numbers of fine groups.

7. THEORY FOR THE FINITE-ELEMENT WITH DISCONTIGUOUS-SUPPORT METHOD

The finite-element with discontiguous-support (FEDS) multigroup method is a Petrov-Galerkin finite element method [16] which allows the energy domain to be partitioned into discontiguous elements [3]. For example, with FEDS, particles with energies 1 eV and 3 eV may belong to one energy element, whereas particles with energies 2 eV and 4 eV may belong to a different energy element. Figure 7.1 compares a contiguous partitioning of the energy domain using the standard multigroup (MG) method to discontiguous partitioning of the energy domain using FEDS.

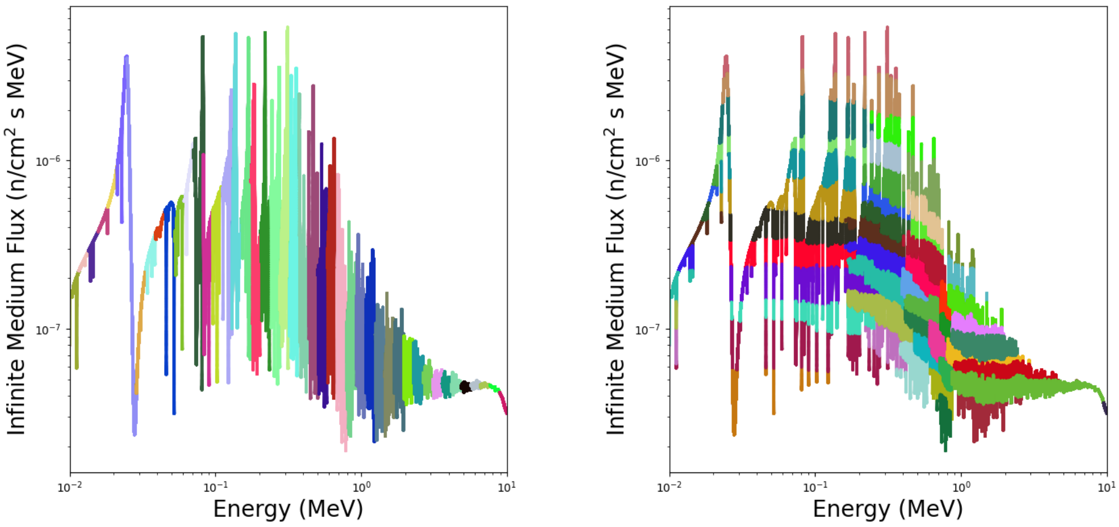

(a) MG

(b) FEDS

Figure 7.1: These plots show the difference in energy partitioning between MG and FEDS. In the left plot, each color represents a different MG energy group. In the right plot, each color represents a different FEDS energy element.

The FEDS method evolved from other nonstandard energy discretization methods. In 1935, astrophysicists first developed the opacity density function (ODF) method as a way to partition the energy domain based on opacities [17]. Since then, many have made significant contributions to the evolution of methods similar to ODF [18, 19], such as the multiband method [20, 21, 22, 23, 24], the subgroup method [25, 26, 27, 28], and the probability tables method [29, 30, 31, 32, 33]. Many of these energy discretization methods use bands, a cross section range, in order to partition elements; energies that have total cross sections that fall within the upper and lower limits of a band belong to that band.

The main distinction between FEDS and its predecessors is that FEDS energy discretization is constructed based on minimizing the variation of the flux within each FEDS energy element. Also, FEDS elements are not strictly confined to group or band boundaries. Notice how in Figure 7.1 there is little variation in flux within each FEDS element and the elements are not bounded by groups or bands, whereas in MG, there is a large variation in flux within each group, and each MG group is restricted to a contiguous energy interval. FEDS has demonstrated greater accuracy than MG for steady-state radiation-transport simulations with one or more resonant materials [3, 34, 35, 36, 37].

7.1 Derivation of the Finite-Element with Discontiguous-Support Multigroup Transport Equation

The angular flux can be expressed as a linear combination of discontiguous basis functions [3],

$$\varphi(\vec{r}, \hat{\Omega}, E, t) = \sum_{e} \psi_e(\vec{r}, \hat{\Omega}, t) b_e(\vec{r}, E) \ , \tag{7.1}$$

These basis functions, $b_e(\vec{r}, E)$, are defined as,

$$b_e(\vec{r}, E) = w_e(E) C_e(\vec{r}) f(\vec{r}, E)$$

where $f(\vec{r}, E)$ is an approximation of the neutron spectrum at location $\vec{r}$, and the weight functions are,

$$w_e(E) = \begin{cases} 1 & E \in E_e \\ 0 & \text{otherwise} \end{cases} .$$

where E_e includes all the energies that belong to element e [3]. Finally, we normalize the basis functions by computing $C_e(\vec{r})$ as

$$C_e(\vec{r}) = \left[\int\limits_{E_e} f(\vec{r}, E)\, dE \right]^{-1} .$$

This results in basis functions and weight functions which are orthonormal,

$$\int\limits_0^\infty dE\, w_n(E) b_e(E) = \delta_{e,n} \int\limits_0^\infty dE\, C_e(\vec{r}) f(\vec{r}, E) .$$

$$\int\limits_0^\infty dE\, w_n(E) b_e(E) = \delta_{e,n} ,$$

where $\delta_{e,n}$ is the Kronecker delta function [38].

Now that we have defined the basis functions and weights for FEDS, we substitute the Petrov-Galerkin finite element approximation into the neutron transport equation, Eq. (2.1),

$$\mathbf{L}\varphi = (\mathbf{S} + \mathbf{F})\varphi + Q \tag{7.2}$$

where φ is an approximation of the angular flux comprised of linear combination of discontiguous basis functions, defined in Eq. (7.1), and $\mathbf{L}$, $\mathbf{S}$, $\mathbf{F}$, and Q are defined in Eqs.(2.2) – (2.6). We continue the derivation of the FEDS transport equation by integrating Eq. (7.2) over all energies belonging to element e,

$$\int\limits_{E_e} dE\, \mathbf{L}\varphi = \int\limits_{E_e} dE \left[(\mathbf{S}+\mathbf{F})\varphi + Q\right] . \tag{7.3}$$

Notice that this derivation of the FEDS transport equation is equivalent to the derivation of the MG equation, in which we integrated over all energies belonging to an energy group.

The left-hand-side of Eq. (7.3) can be expressed as

$$\int\limits_{E_e} dE\, \mathbf{L}\varphi = \int\limits_{0}^{\infty} dE\, w_e(E)\mathbf{L}\varphi .$$

After expanding the FEDS approximation of the angular flux,

$$\int\limits_{E_e} dE\, \mathbf{L}\varphi = \int\limits_{0}^{\infty} dE\, w_e(E)\mathbf{L}\left[\sum_{n=1}^{N} \psi_n(\vec{r},\hat{\Omega},t) b_n(\vec{r},E)\right] .$$

Note, the integrand is only nonzero when e and n are the same element, hence

$$\int\limits_{E_e} dE\, \mathbf{L}\varphi = \int\limits_{0}^{\infty} dE \left[\frac{1}{v(E)}\frac{\partial}{\partial t} + \hat{\Omega}\cdot\nabla\ + \Sigma_t(\vec{r},E,t)\right] \left[\psi_e(\vec{r},\hat{\Omega},t) b_e(\vec{r},E)\right] .$$

Finally, if we use element-averaged values for speed and cross section we can simplify this to

$$\int\limits_{E_e} dE\, \mathbf{L}\varphi = \frac{1}{v_e}\frac{\partial\psi_e}{\partial t} + \hat{\Omega}\cdot\nabla\psi_e\ + \Sigma_{t,e}(\vec{r},t)\psi_e(\vec{r},\hat{\Omega},t) .$$

Similarly,

$$\int\limits_{E_e} dE\, \mathbf{S}\varphi = \sum_{e'=1}^{E} \int\limits_{4\pi} d\Omega'\, \Sigma_{s,e'\to e}(\vec{r},\hat{\Omega}'\cdot\hat{\Omega},t)\psi_{e'}(\vec{r},\hat{\Omega}',\ t)$$

$$\int\limits_{E_e} dE\, \mathbf{F}\varphi = \frac{1}{4\pi}\sum_{e'=1}^{E} \Sigma_{f,e'\to e}(\vec{r},t)\phi_{e'}(\vec{r},t)$$

$$\int\limits_{E_e} dE\, Q = q_e(\vec{r},E,t) + \sum_{i=1}^{N} \frac{\chi_{d,i,e}}{4\pi}\lambda_i C_i(\vec{r},t)\ .$$

Thus, the expanded form of the FEDS transport equation is equivalent to the MG transport equation, Eq. (3.2), with the exception that FEDS elements can have a discontiguous support in the energy domain,

$$\begin{aligned} &\frac{1}{v_e}\frac{\partial \psi_e}{\partial t} + \hat{\Omega}\cdot\nabla\psi_e + \Sigma_{t,e}(\vec{r},t)\psi_e(\vec{r},\hat{\Omega},t) = \\ &\qquad \sum_{e'=1}^{E}\int\limits_{4\pi} d\Omega'\, \Sigma_{s,e'\to e}(\vec{r},\hat{\Omega}'\cdot\hat{\Omega},t)\psi_{e'}(\vec{r},\hat{\Omega}',\ t) + \frac{1}{4\pi}\sum_{e'=1}^{E}\Sigma_{f,e'\to e}(\vec{r},t)\phi_{e'}(\vec{r},t) + \\ &\qquad\qquad q_e(\vec{r},E,\ t) + \sum_{i=1}^{N}\frac{\chi_{d,i,e}}{4\pi}\lambda_i C_i(\vec{r},t)\ . \end{aligned} \tag{7.4}$$

Note, the following element-averaged variables were substituted in this derivation

$$\frac{1}{v_e(\vec{r})} = \int\limits_{0}^{\infty} dE\, \frac{1}{v(E)} b_e(\vec{r},E)$$

$$\Sigma_{t,e}(\vec{r},t) = \int\limits_{0}^{\infty} dE\, \Sigma_t(\vec{r},E,t) b_e(\vec{r},E)$$

$$\Sigma_{s,e'\to e}(\vec{r},\hat{\Omega}'\cdot\hat{\Omega},t) = \int\limits_{0}^{\infty} dE\, w_e(E)\int\limits_{4\pi} d\Omega' \int\limits_{0}^{\infty} dE\, \Sigma_s(\vec{r},\hat{\Omega}'\cdot\hat{\Omega},E'\to E,t)\, b_{e'}(\vec{r},E')$$

$$\Sigma_{f,e'\to e}(\vec{r},t) = \int\limits_{0}^{\infty} dE\, w_n(E)\int\limits_{0}^{\infty} dE\, \Sigma_f(\vec{r},E'\to E,t) b_{e'}(\vec{r},E')$$

where

$\psi_e(\vec{r}, \hat{\Omega}, t)$	angular flux for element e
v_e	speed for element e
$\Sigma_{t,e}(\vec{r}, t)$	total macroscopic cross section for element e
$\Sigma_{s,e'\to e}(\vec{r}, \hat{\Omega}' \cdot \hat{\Omega}, t)$	differential scattering cross section from element e' to element e
$\Sigma_{f,e'\to e}(\vec{r}, t)$	differential fission cross section from element e' to element e
$q_e(\vec{r}, \hat{\Omega}, t)$	extraneous source term for element e
$C_i(\vec{r}, t)$	concentration of delayed neutron precursor flavor i
λ_i	decay constant for precursor flavor i
$\chi_{d,i,e}$	delayed neutron source into element e for precursor flavor i

The theoretical advantage of FEDS over MG is that discontiguous energy discretizations can capture resonance-scale behavior with fewer energy degrees-of-freedom, and thus are capable of estimating steady-state quantities of interest with much greater accuracy. However, there are some caveats:

- discontiguous energy discretizations are inherently worse at modeling neutron speeds compared to contiguous energy discretizations
- FEDS can create an ideal energy discretization for a single material, but the energy partitioning can become less optimal when multiple materials need to be modeled
- discontiguous energy discretizations result in to denser scattering matrices due to artificial upscattering, caused by neutrons scattering back and forth between different discontiguous energy elements.

7.2 Objective Function for Finite-Elements with Discontiguous-Support

An optimization algorithm is used to construct the FEDS energy discretization by minimizing the variation of the continuous-energy flux within each energy element. Namely, the optimization algorithm tries to minimize the following objective function,

$$F = \left(\sum_{p} \omega_p \Big[\sum_{g} \Delta E_g |\phi_{p,g} - \bar{\phi}_{p,g(e)}| \Big]^{M} \right)^{1/M} , \tag{7.5}$$

where

p	a point on the continuous-energy spectrum
g	a hyperfine energy group
e	an energy element
δE_g	energy width of group g
M	a norm
$\phi_{p,g}$	the analytical pointwise flux for point p and group g
$\bar{\phi}_{p,g(e)}$	the average of $\phi_{p,g}$ within element e
ω_p	the weight of point p

We estimate the analytical pointwise flux $\phi_{p,g}$ by computing the solution for a spatially-simplified transport problem. Specifically, we compute the pointwise flux by solving the energy-dependent infinite-medium equation,

$$[\Sigma_e + \Sigma_t(E)\phi(E)] = q(E) ,$$

where Σ_e is an analytic escape cross section [36]. For a thermal system, the source term $q(E)$ is assumed to be either a Maxwellian spectrum, a $1/E$ distribution, or a Watt fission spectrum depending on the energy value E.

The problem with the objective function shown in Eq. (7.5) is that the scalar flux can vary by several orders of magnitude and it is usually more practical to minimize the variation of the logarithm of the flux instead [3]. Specifically, the following objective function is minimized instead

$$F = \left\{ \sum_{e} \left(\sum_{g \in S_e} \left[\sum_{p} |O_{p,g} - \bar{O}_{e,p}|^M \right]^{N_1/M} \right)^{N_2/N_1} \right\}^{1/N_2} \tag{7.6}$$

$$O_{p,g} = \omega_p^{1/M} \log_{10}(E_g \phi_{p,g})$$

where $O_{p,g}$ is the observation value for point p and hyperfine group g. Also, M, N_1, and N_2 are norms that depend on the optimization method. For example, if hierarchical agglomerative clustering is used with Euclidean distance measurements and Ward linkage, the values are $M = 2$, $N_1 = 2$, and $N_2 = \infty$. Till has shown that Eq. (7.6) works well for steady-state simulations, but is not fine-tuned for time-of-flight simulations [3].

7.3 Improving Convergence to Continuous Energy in Time-Dependent Simulations

For time-dependent simulations, it is essential that both FEDS cross sections and speed values converge to their continuous-energy values. Previously, Till showed that FEDS energy discretizations can also be constructed by minimizing the variation in multiple parameters simultaneously [3]. Here, we borrow this idea to write an objective function that should theoretically perform well for a single-material time-of-flight problem. This objective function depends on flux, cross section, and neutron speed (ϕ, Σ, and v) simultaneously:

$$F=\left\{\sum_{e}\left(\sum_{g\in S_e}\left[\sum_{p}|A_{p,g}-\bar{A}_{e,p}|^M+|B_{p,g}-\bar{B}_{e,p}|^M+|C_{p,g}-\bar{C}_{e,p}|^M\right]^{N_1/M}\right)^{N_2/N_1}\right\}^{1/N_2} \tag{7.7}$$

$$A_{p,g}=\omega_p^{1/M}\log_{10}(E_g\phi_{p,g})$$

$$B_{p,g}=\omega_p^{1/M}\log_{10}(\Sigma_{p,g})$$

$$C_{p,g}=\omega_p^{1/M}\log_{10}(v_g)$$

where $A_{p,g}$, $B_{p,g}$, and $C_{p,g}$ represent three unique observations corresponding to point p and hyperfine group g. Note, in time-of-flight simulations neutron arrival times are proportional to $1/v$, so it seems natural to use $1/v$ as an optimization parameter instead of v. However, note that in Eq. (7.7) using v as an optimization parameter is equivalent to using $1/v$ as an optimization parameter because of the following property of logarithms:

$$|\log_{10}(v)|=|\log_{10}(1/v)|\,.$$

For multi-material problems Eq. (7.7) would have to be modified by adding more observations to account for the cross sections and fluxes in other materials.

Figure 7.2 demonstrates how Eq. (7.7) improves convergence to continuous-energy speeds and cross sections. Notice how MG converges well to continuous-energy speeds, but not continuous-energy cross sections. Inversely, the version of FEDS that only used ϕ and Σ as clustering optimization parameters converges well to continuous-energy cross section values, but not continuous-energy speeds. By adding v as an additional optimization parameter, FEDS demonstrated simultaneous convergence to both continuous-energy speeds and cross sections. However, note that this convergence to continuous-energy speeds is still slightly slower than the rate at which MG converges to continuous-energy speeds.

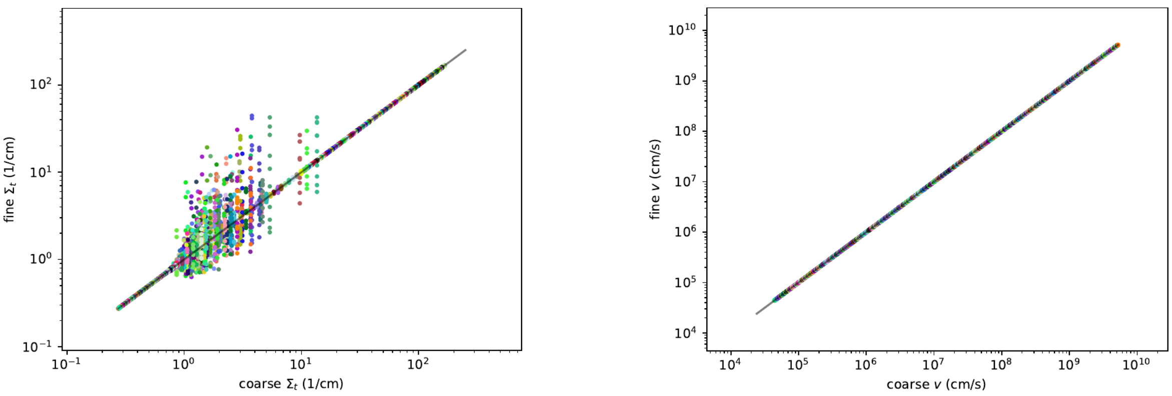

(a) MG cross sections

(b) MG speeds

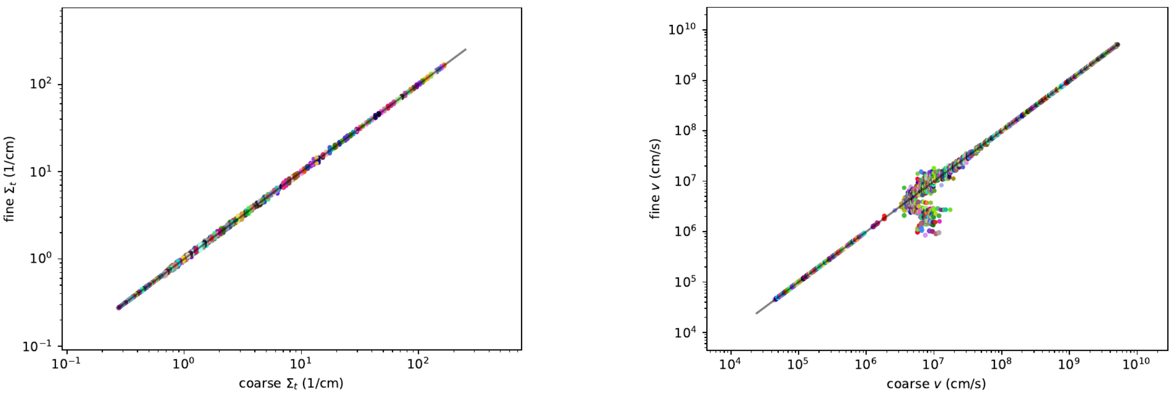

(c) FEDS (ϕ, Σ) cross sections

(d) FEDS (ϕ, Σ) speeds

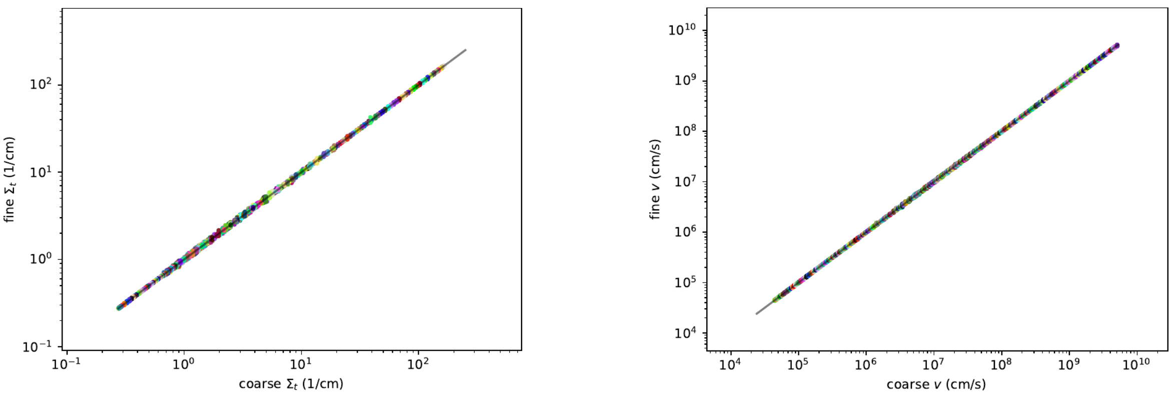

(e) FEDS (ϕ, Σ, v) cross sections

(f) FEDS (ϕ, Σ, v) speeds

Figure 7.2: These plots compare how different energy discretizations converge to continuous-energy values (indicated by the black line) for an infinite-medium of HEU. Group/elements are color coordinated. In these plots "fine" refers to 5000 pointwise values, and "coarse" refers to group- or element-averaged values.

7.4 Energy Penalties

An alternative strategy for improving FEDS' ability to model neutron speeds is to use an energy penalty [3]. This energy penalty is imposed by defining a new observation for the FEDS objective function,

$$O_{p,g} = \beta\sqrt{N_o}\log_{10}\left[\frac{\phi_{\text{max}}}{\phi_{\text{min}}}\right]\frac{\log_{10}(E_g)}{\log_{10}\left(\frac{E_{\text{max}}}{E_{\text{min}}}\right)}$$

where β is the energy penalty term, $\frac{\phi_{\text{max}}}{\phi_{\text{min}}}$ is the ratio of the largest to the smallest flux, and N_o represents the number of other observations in the objective function. Note that when $\beta = 0$, it is equivalent to not having an energy penalty. For a single-material time-dependent neutron transport simulation, we can use the following FEDS objective function:

$$F = \left\{\sum_{e}\left(\sum_{g\in S_e}\left[\sum_{p}|A_{p,g}-\bar{A}_{e,p}|^M+|B_{p,g}-\bar{B}_{e,p}|^M+|C_{p,g}-\bar{C}_{e,p}|^M\right]^{N_1/M}\right)^{N_2/N_1}\right\}^{1/N_2} \tag{7.8}$$

$$A_{p,g} = \omega_p^{1/M}\log(E_g\phi_{p,g})$$

$$B_{p,g} = \omega_p^{1/M}\log(\Sigma_{p,g})\ ,$$

$$C_{p,g} = \beta\sqrt{N_o}\log_{10}\left[\frac{\phi_{\text{max}}}{\phi_{\text{min}}}\right]\frac{\log_{10}(E_g)}{\log_{10}\left(\frac{E_{\text{max}}}{E_{\text{min}}}\right)}$$

where $C_{p,g}$ is the observation with the energy penalty term β. In this case $N_o = 2$, since there are two other observations. For multi-material neutron transport simulations, a similar objective function can be defined but with $2N_m + 1$ observations instead, where N_m is the number of materials and $N_o = 2N_m$. In the past, this energy penalty was only applied to steady-state quantities of interest, and values of β less than one were used. However, in this study, we found that larger values of β were able to enhance the performance of FEDS for time-dependent neutron transport.

Figure 7.3 demonstrates the effect that energy penalties have on the FEDS discretizations. For small energy penalty values, FEDS elements tend to be more discontiguous. As larger energy penalties are used the FEDS discretizations begin to look more like contiguous MG discretizations. Consequently, when large values of energy penalties are used the accuracy of the FEDS discretizations are similar to the accuracy of MG discretizations for various quantities of interest.

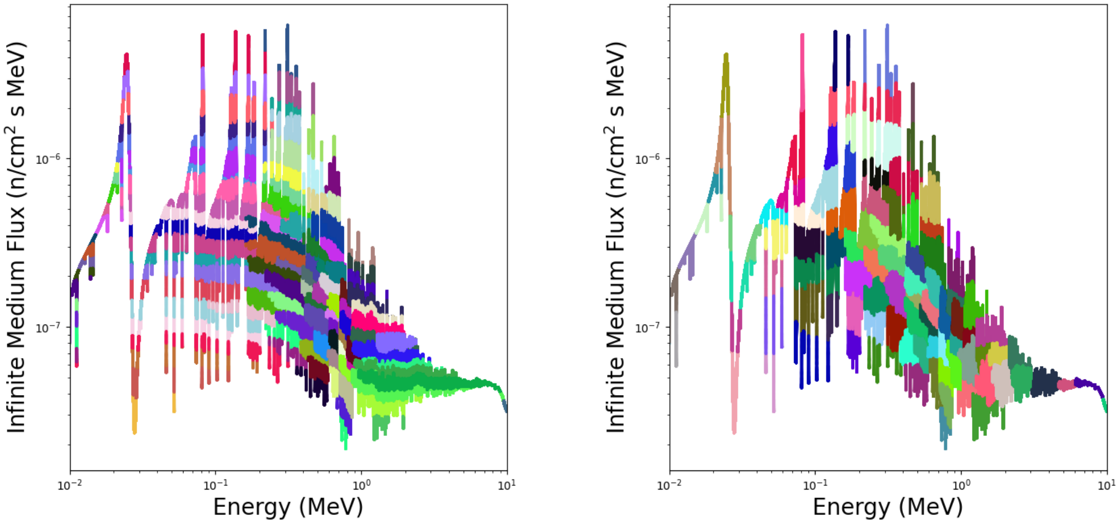

(a) Energy Penalty = 0

(b) Energy Penalty = 1

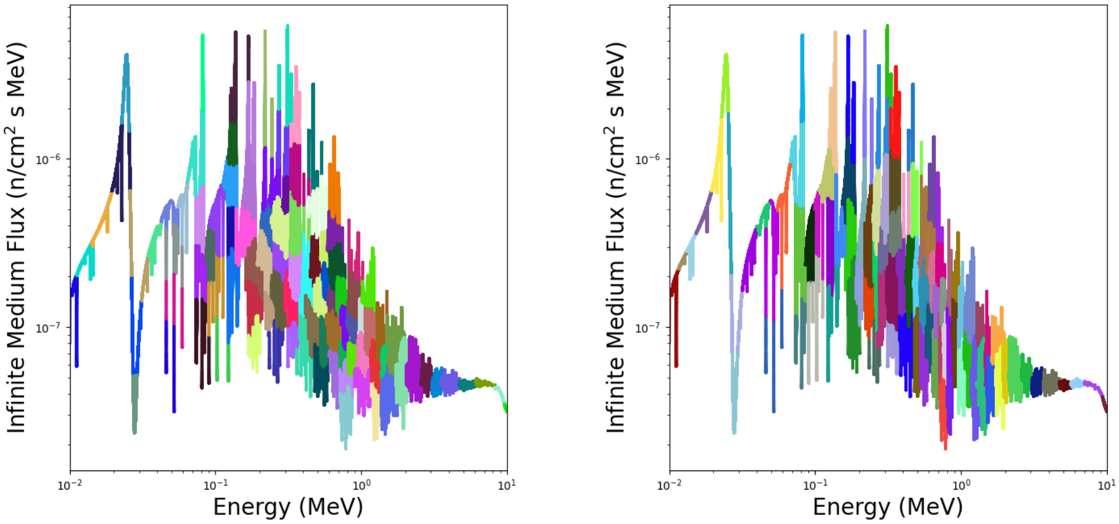

(c) Energy Penalty = 2.5

(d) Energy Penalty = 5

Figure 7.3: These plots show the FEDS energy discretizations that were constructed for different energy penalty values. Each color represents a different energy element.

7.5 Coarse Groups

A third strategy for improving the performance of FEDS for time-dependent simulations is to use coarse groups. This is accomplished by first partitioning the energy domain into coarse groups which are contiguous, and then further partitioning those coarse groups into FEDS energy elements which can be discontiguous. The intention is to confine the maximum energy span of an energy element.

Figure 7.4 compares FEDS energy discretizations that have different numbers of coarse groups. A theoretical disadvantage of using coarse groups is that elements that belong to the same coarse group tend to have the same energy span and thus have similar element-averaged neutron speeds. In fact, it is possible that multiple elements belonging to the same coarse group have almost identical values for element-averaged neutron speed. This could result in large gaps in the element speeds that belong to different coarse groups, which is problematic for time-of-flight simulations. On the other hand, a theoretical advantage of using coarse groups is that it bounds the artificial upscattering that is created by using discontiguous energy discretizations, reducing the amount of upper-diagonal terms in the scattering matrix. This creates a scattering matrix that is block lower-triangular [36].

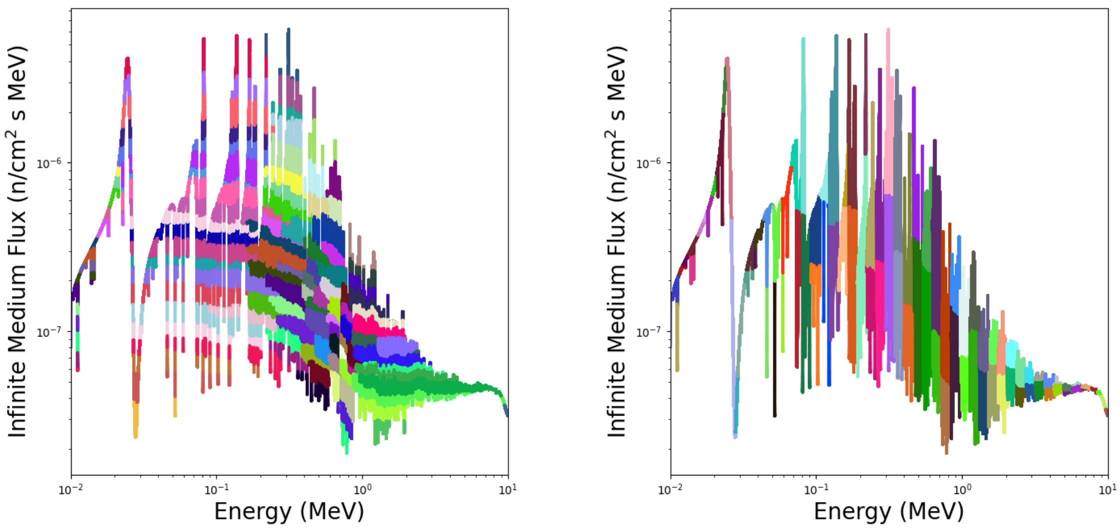

(a) FEDS, No Coarse Groups

(b) FEDS, 2 Elements per Coarse Group

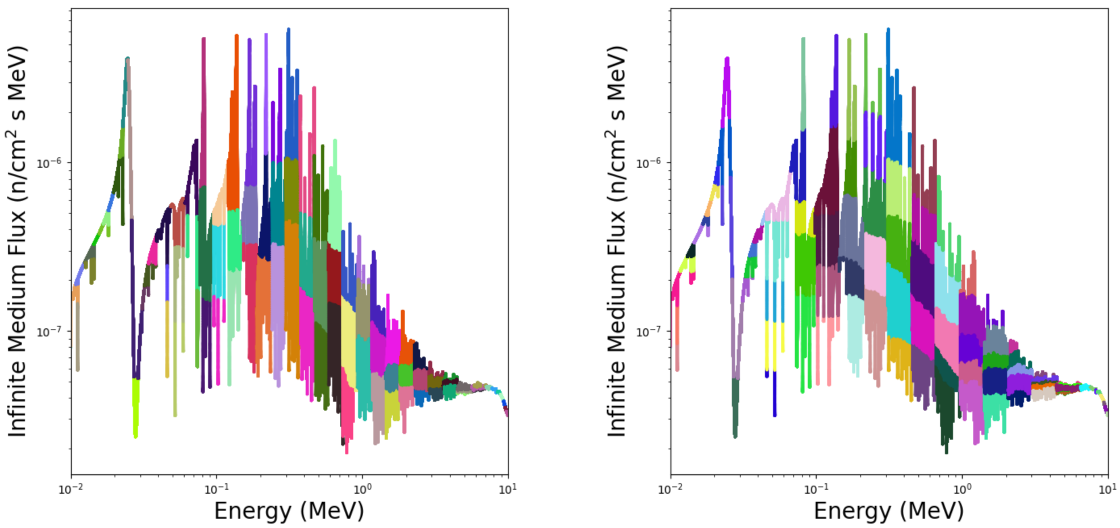

(c) FEDS, 3 Elements per Coarse Group

(d) FEDS, 5 Elements per Coarse Group

Figure 7.4: These plots display the FEDS energy discretizations that were constructed with different numbers of FEDS elements per coarse group. Each color represents a different energy element.

We conducted some preliminary comparisons to determine which energy discretization strategies result in the smallest discrepancy between the various energy discretizations and continuous-energy values. For these studies we used 400 energy degrees-of-freedoms (MG groups or FEDS elements) for each discretization, and macroscopic cross section data for U-235 was used. Table 7.1 compares the discrepancy between discrete and continuous-energy values for cross section at 10,000 points, logarithmically-spaced in the energy domain. Similarly, Table 7.2 compares the discrepancy between discrete and continuous-energy values for speed at 10,000 points, logarithmically-spaced in the energy domain. The L_1, L_2, and L_∞ relative error norms were used as metrics to quantify the energy-discretization error for various discretization strategies, and are defined as

$$||\varepsilon||_1 = \frac{\sum_p |u_{d,p} - u_{c,p}|}{\sum_p |u_{c,p}|}$$

$$||\varepsilon||_2 = \sqrt{\frac{\sum_p |u_{d,p} - u_{c,p}|^2}{\sum_p |u_{c,p}|^2}}$$

$$||\varepsilon||_\infty = \frac{\max |u_{d,p} - u_{c,p}|}{\max |u_{c,p}|}$$

where $u_{d,p}$ is the energy-discretized value for point p and $u_{c,p}$ is the continuous-energy value at point p.

Note that in Table 7.1, the MG discretization and the FEDS discretization with an energy penalty of 50 had the largest L_1, L_2, L_∞ cross section error norms. In contrast, the FEDS discretization that used v as an additional optimization parameter had the smallest L_1, L_2, L_∞ cross section error norms. In general, many FEDS discretizations provided an improvement in cross section values compared to MG. Inversely, note that in Table 7.2, the MG discretization had the smallest L_1, L_2, L_∞ speed error norms. Although, using either high energy penalties or using coarse groups allowed FEDS to also have small L_1, L_2, L_∞

speed error norms as well.

For energy penalty values, there was a noticeable trade off in ability to accurately model cross sections and neutron speeds: smaller energy penalties generated more accurate cross sections, whereas large energy penalties produced more accurate neutron speeds.

Table 7.1: Comparing the discrepancy between continuous and discrete values for cross section, Σ_t, at 10,000 logarthmically-spaced points using L_1, L_2, L_∞ relative error norms. Each energy discretization compared contained 400 energy degrees-of-freedoms.

Method	Clustering Constraints	L_1 Error	L_2 Error	L_∞ Error
MG	logarithmically-spaced groups	8.76%	18.95%	91.71%
FEDS	no coarse groups, no energy penalty	3.87%	4.80%	21.62%
FEDS	used $v(E)$ as additional optimization parameter	3.56%	4.11%	17.71%
FEDS	energy penalty = 0.25	3.62%	4.21%	17.71%
FEDS	energy penalty = 0.50	3.66%	4.23%	17.71%
FEDS	energy penalty = 1.	3.65%	4.78%	25.72%
FEDS	energy penalty = 2.5	4.19%	6.42%	30.03%
FEDS	energy penalty = 5.	4.67%	6.91%	31.43%
FEDS	energy penalty = 10.	5.61%	9.61%	45.28%
FEDS	energy penalty = 25.	7.88%	15.77%	88.59%
FEDS	energy penalty = 50.	9.18%	19.70%	89.22%
FEDS	exactly 2 elements per coarse group	5.93%	12.33%	65.75%
FEDS	average of 2 elements per coarse group	3.64%	4.64%	25.99%
FEDS	exactly 5 elements in each coarse group	3.61%	6.18%	32.20%
FEDS	average of 5 elements per coarse group	4.41%	5.19%	17.71%

Table 7.2: Comparing the discrepancy between continuous and discrete values for speed, v, at 10,000 logarthmically-spaced points using L_1, L_2, L_∞ relative error norms. Each energy discretization compared contained 400 energy degrees-of-freedoms.

Method	Clustering Constraints	L_1 Error	L_2 Error	L_∞ Error
MG	logarithmically-spaced groups	0.74%	0.85%	1.47%
FEDS	no coarse groups, no energy penalty	4.39%	5.31%	9.77%
FEDS	used $v(E)$ as additional optimization parameter	3.41%	4.04%	9.93%
FEDS	energy penalty = 0.25	3.21%	3.99%	9.77%
FEDS	energy penalty = 0.50	2.49%	2.90%	4.94%
FEDS	energy penalty = 1.	1.82%	2.12%	4.42%
FEDS	energy penalty = 2.5	1.48%	1.73%	3.68%
FEDS	energy penalty = 5.	1.24%	1.46%	3.22%
FEDS	energy penalty = 10.	1.03%	1.22%	2.54%
FEDS	energy penalty = 25.	0.95%	1.17%	2.34%
FEDS	energy penalty = 50.	0.86%	1.01%	2.08%
FEDS	exactly 2 elements per coarse group	0.79%	0.95%	2.85%
FEDS	average of 2 elements per coarse group	1.48%	1.71%	3.03%
FEDS	exactly 5 elements per coarse group	0.85%	0.98%	2.49%
FEDS	average of 5 elements per coarse group	3.50%	4.09%	6.27%

7.6 Hierarchical Agglomerative Clustering

One option for minimizing the FEDS objective function is to use a hierarchical agglomerative clustering algorithm. The purpose of this clustering algorithm is to cluster data points with similar values into clusters. This results in minimal variation of values within each cluster.

In order to construct the optimal FEDS energy grid, it is best to start with a large number of points in the energy domain, for example, a million energy points logarithmically-spaced between 10^-5 eV and 20 MeV. For each energy point, we determine the value of different observations corresponding to that point. For hierarchical agglomerative clustering, each point starts off as its own cluster i, then:

1. The distance between any two clusters i and j is computed, for all possible combinations of clusters.
2. The distances are then sorted to determine the shortest distance.
3. The clusters i and j that have the shortest distance from each other are clustered together. This process is repeated until the desired number of clusters is achieved.

In this study, the Ward's minimum variance method was used to evaluate the distance between two clusters [39]. In the Ward minimum variance method, the distance between cluster A and cluster B is measured as the increase in variance that would result from merging the two clusters,

$$\Delta(A,B) = \sum_{i \in A \cup B} \|O_i - \bar{O}_{A \cup B}\|_2 - \sum_{i \in A} \|O_i - \bar{O}_A\|_2 - \sum_{i \in B} \|O_i - \bar{O}_B\|_2 \,,$$

where $\bar{O}$ represents the centroid of a cluster, and $\Delta(A,B)$ is called the merging cost for combining clusters A and B.

Figure 7.5 shows an example of hierarchical agglomerative clustering with six data points, and its associated dendrogram. Figure 7.5 demonstrates how observations 1 and 2 can be thought of as orthogonal dimensions in a Euclidean space (even if the observations are not truly orthogonal) and shows how six data points are merged into two separate clusters via hierarchical agglomerative clustering. This visual also depicts how each point or cluster can be thought of as a node on a hierarchical tree. Each node in the hierarchical tree can have a maximum of one parent node and a maximum of two daughter nodes. A node that has no parent nodes, is called an orphan node. In Figure 7.5, there are two orphan nodes “ABC" and “DEF". Once the algorithm is complete, each orphan node corresponds to a FEDS energy element. This could result in a discontiguous set of energies belonging to a single FEDS element, assuming no connectivity constraints are placed on the algorithm.

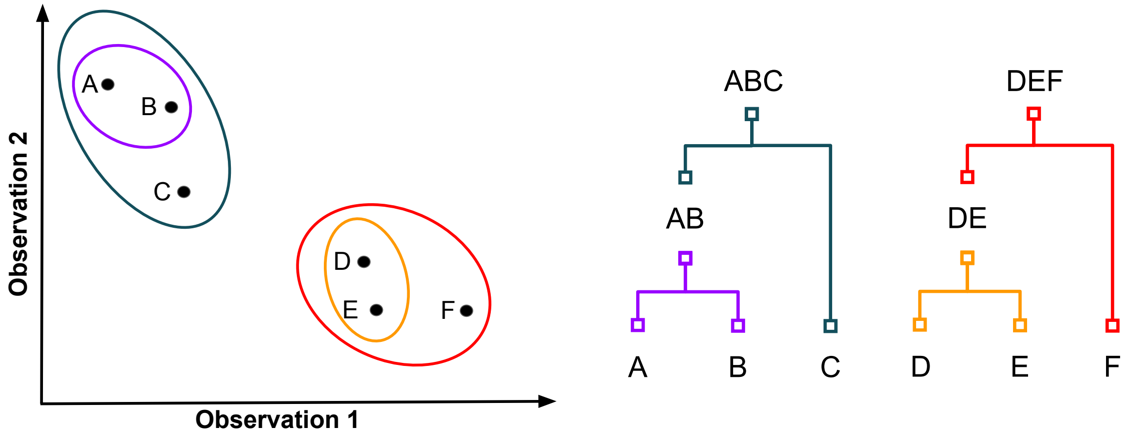

Figure 7.5: An example of hierarchical agglomerative clustering on a two-dimensional Euclidean space (left), and it’s equivalent dendrogram (right).

After the clustering process is complete, FEDS cross sections are computed for the constructed energy discretization [3]. One of the limitations of the optimization algorithm is that it may converge to a local minimum, instead of the global minimum.

7.7 Generating Weighted-Averaged Cross Sections

Bondarenko iterations are used to iteratively modify the weighting spectrum to produce self-consistent MG (or FEDS) cross sections for each energy group g and each isotope i in a material [40]. A Bondarenko iteration consists of the following steps:

Step 1: Compute the background microscopic cross section $\sigma_{0,g,i}^{k}$ for iteration k

$$\sigma_{0,g,i}^{k} = \frac{1}{N_i}\Big(\Sigma_e + \sum_{j\neq i} N_j \sigma_{t,g,i}^{k-1}\Big) \ ,$$

where N is the number density of an isotope, and Σ_e is an analytic escape cross section.

Step 2: Compute the weighting spectrum $w_i^k(E)$ using the new background cross section

$$w_i^k(E) \approx \frac{S(E)}{N_i\Big(\sigma_{t,i}^{k}(E) + \sigma_{0,g,i}^{k}\Big)} \ .$$

Step 3: Compute the total microscopic cross section $\sigma_{t,g,i}^{k}$ using the updated weighting spectrum

$$\sigma_{t,g,i}^{k} = \frac{\int_{E_g}^{E_{g-1}} dE \ w_i^k(E)\sigma_{t,i}^{k}(E)}{\int_{E_g}^{E_{g-1}} dE \, w_i^k(E)} \ .$$

Step 4: After steps 1 through 3 are completed for all isotopes and groups, check that the following convergence criterion is satisfied,

$$|| \frac{\sigma_{t,g,i}^{k} - \sigma_{t,g,i}^{k-1}}{\sigma_{t,g,i}^{k}} || < \varepsilon \ .$$

If the convergence criterion is not satisfied, repeat steps 1 through 4.

8. TIME-OF-FLIGHT PROBLEM 1: AN IRON SLAB

This test problem derives from the time-of-flight problem in Till's dissertation [3]. However, in this study we compare an even wider variety of energy discretizations.

In time-of-flight simulations, the quantity of neutrons reaching a detector is measured as a function of time. For these simulations, it is essential to accurately model neutron speeds, since detector arrival times are inversely proportional to neutron speeds. Previously, the only FEDS discretizations that were tested for this problem were FEDS discretizations that used coarse groups. The reason for using coarse groups is that they strictly limit the energy span of FEDS elements, thus resulting in element speeds that are more representative of true neutron speeds. Here, we also test discretizations that do not use coarse groups, but rely on other strategies for limiting the energy span of FEDS elements. These strategies included adding v as an additional FEDS optimization parameter well as using energy penalties. We also compare these to the standard MG method.

8.1 Description of Time-Of-Flight Problem 1

This test problem consists of a thin slab of containing an extraneous fission source adjacent to a slab of natural iron, with a density of 7.874 g/cm^3 at room temperature (293.6 K). A point detector is placed at various distances away from the source. This detector is used to obtain the energy-integrated flux at the detector location as a function of time. The physical layout of the test problem is shown in Figure 8.1, and isotopic composition of the iron is shown in Table 8.1.

The point detector is assumed to be perfectly collimated and therefore the contribution of scattered neutrons to the detector signal is assumed to be negligible. Consequently, the flux of neutrons reaching the detector can be approximated as simply the uncollided flux for $\hat{\Omega} = +\hat{x}$. The source is pulsed and turned off after 1 ns. The extraneous fission

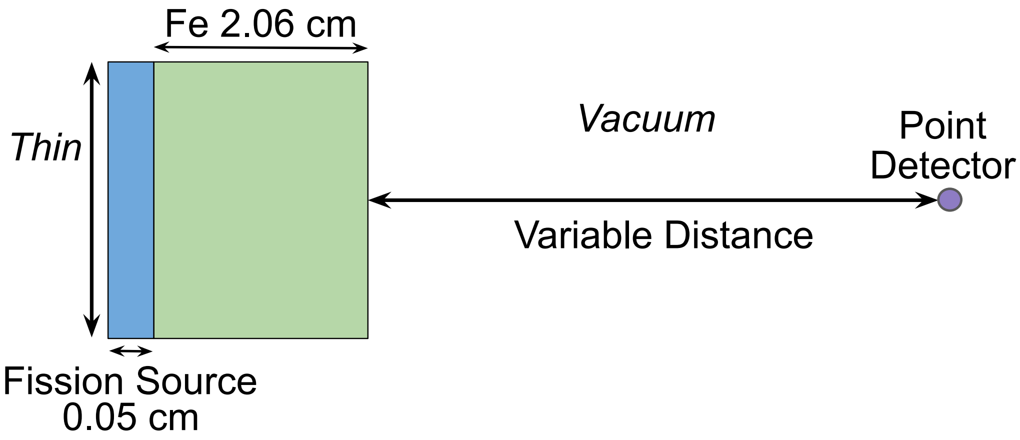

Figure 8.1: Physical configuration of the iron slab time-of-flight problem.

Table 8.1: Isotopic composition of iron.

Isotope	Number Density ($\frac{\text{nuclei}}{\text{barn-cm}}$)
^{54}Fe	8.68307×10^{-6}
^{56}Fe	1.36306×10^{-4}
^{57}Fe	3.14789×10^{-6}
^{58}Fe	4.18926×10^{-7}

source is assumed to produce neutrons with energies corresponding to the Watt spectrum for ^{235}U, and is also assumed to produce these neutrons uniformly in space, angle and time. Additionally, neutron interactions within the fission source are assumed to be negligible. Based on these assumptions, the transport equation can be simplified to

$$\left(\frac{1}{v(E)}\frac{\partial}{\partial t} + \frac{\partial}{\partial x} + \Sigma(x,E)\right)\phi(x,E,t) = \frac{q(x,E,t)}{4\pi} \, ,$$

$$q(x,E,t) = \begin{cases} \frac{4\pi}{\tau X_S}\chi(E) & \text{for } x \in [0, X_S] \, , \; t \in [0, \tau] \\ 0 & \text{otherwise} \end{cases} \, ,$$

$$\Sigma(x,E) = \begin{cases} \Sigma_I(E) & \text{for } x \in [X_S, X_S + X_I] \\ 0 & \text{otherwise} \end{cases} ,$$

where X_S is the thickness of the source, X_I is the thickness of the iron, τ is the duration of the pulse, Σ_I is the macroscopic cross section for iron, and $\chi(E)$ is the Watt fission spectrum for U-235. Next, we wish to analytically determine the following quantities of interest:

1. the total number of reactions
2. the energy-integrated detector response as a function of time.

The total number of reactions, R, is calculated by integrating over time and phase space

$$R = \int_0^\infty dE \ \chi(E)(1 - e^{-\Sigma(E)X_I}) \, .$$

The energy-integrated detector response D_b for time bin b can be expressed as

$$D_b = \int_0^\infty dE \int_{t_b}^{t_{b+1}} dt \, \phi(X_D, E, t) \, , \tag{8.1}$$

where X_D is the location of the detector along the x-axis, and the flux at the detector location is defined as

$$\phi(X_D, E, t) = \frac{\chi(E)}{\tau X_S} e^{-\Sigma(E)X_I} \int_{X_D - X_S}^{X_D} dx_\delta \left[\, H\left(t - \frac{x_\delta}{v}\right) - H\left(t - \tau - \frac{x_\delta}{v}\right) \right] ,$$

where X_I is the thickness of the iron slab, X_S is the thickness of the source and H is the

Heaviside step function [41]. Thus, Eq. (8.1) becomes

$$D_b = \int\limits_0^\infty dE\,\frac{\chi(E)}{\tau X_S} e^{-\Sigma(E)X_I} \int\limits_{X_D - X_S}^{X_D} dx_\delta \int\limits_{t_b}^{t_{b+1}} dt\left[H\left(t - \frac{x_\delta}{v}\right) - H\left(t - \tau - \frac{x_\delta}{v}\right)\right], \quad (8.2)$$

where t_b and t_{b+1} represent the lower and upper bounds for time bin b, where $t_{b+1} > t_b$. Both of the following integrals can be evaluated using integration by parts

$$\int\limits_{t_b}^{t_{b+1}} dt\,H\left(t - \frac{x_\delta}{v}\right) = t_{b+1}H\left(t_{b+1} - \frac{x_\delta}{v}\right) - t_bH\left(t_b - \frac{x_\delta}{v}\right) - \frac{x_\delta}{v}H\left(\frac{x_\delta}{v} - t_b\right)H\left(t_{b+1} - \frac{x_\delta}{v}\right), \quad (8.3)$$

$$\int\limits_{t_b}^{t_{b+1}} dt\,H\left(t - \tau - \frac{x_\delta}{v}\right) = t_{b+1}H\left(t_{b+1} - \tau - \frac{x_\delta}{v}\right) - t_bH\left(t_b - \tau - \frac{x_\delta}{v}\right) - \left(\tau + \frac{x_\delta}{v}\right)H\left(\tau + \frac{x_\delta}{v} - t_b\right)H\left(t_{b+1} - \tau - \frac{x_\delta}{v}\right). \quad (8.4)$$

By plugging in Eq. (8.3) and Eq. (8.4) into Eq. (8.2), we find that the detector response is

$$\begin{aligned} D_b = \int\limits_0^\infty dE\,\frac{\chi(E)}{\tau X_S} e^{-\Sigma(E)X_I} \int\limits_{X_D - X_S}^{X_D} dx_\delta \Bigg\{ & t_{b+1}\Big[H\left(t_{b+1} - \frac{x_\delta}{v}\right) - H\left(t_{b+1} - \tau - \frac{x_\delta}{v}\right)\Big] - \\ & t_b\Big[H\left(t_b - \frac{x_\delta}{v}\right) - H\left(t_b - \tau - \frac{x_\delta}{v}\right)\Big] - \\ & \frac{x_\delta}{v}H\left(\frac{x_\delta}{v} - t_b\right)H\left(t_{b+1} - \frac{x_\delta}{v}\right) + \\ & \left(\tau + \frac{x_\delta}{v}\right)H\left(\tau + \frac{x_\delta}{v} - t_b\right)H\left(t_{b+1} - \tau - \frac{x_\delta}{v}\right)\Bigg\}. \quad (8.5) \end{aligned}$$

A Python script was written in order to obtain the analytical solutions.

The cross sections for iron were extracted from the United States' Evaluated Nuclear Data Library B-VII.1 (ENDF/B-VII.1) [14], and post-processed with the NJOY Nuclear Data Processing System, Version 2016 (NJOY2016) [15] in order to generate the continuous-energy, MG and FEDS cross sections. Figure 8.2 shows the macroscopic cross section for natural iron. The MG and FEDS cross sections were generated using Bondarenko iterations in order to properly weight cross section values. For the MG discretizations, we simply partitioned the energy domain into logarithmically-spaced groups. Similarly, for FEDS discretizations that used coarse groups, we also partitioned the energy domain into logarithmically-spaced groups. For the energy discretizations that used v is an additional observation, no coarse groups were used. Also, for the energy discretization that used energy penalties, no coarse groups were used.

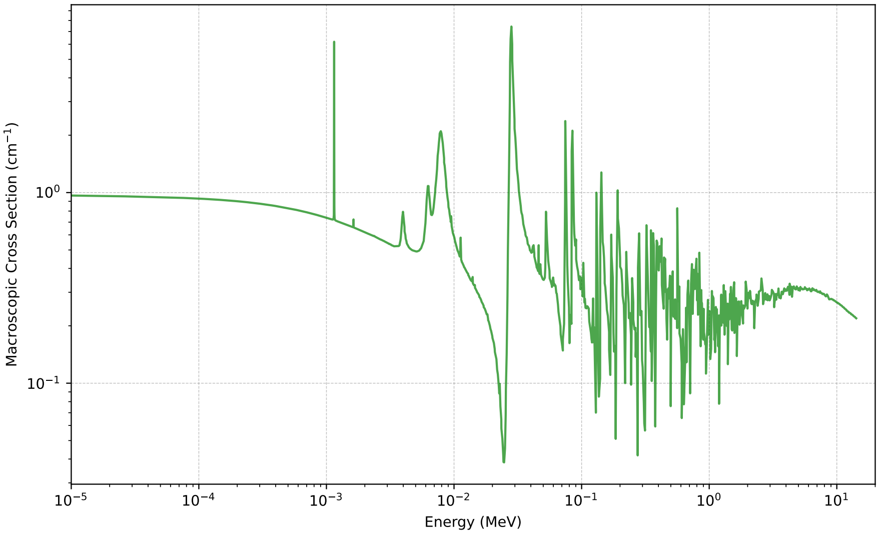

Figure 8.2: Macroscopic cross section of natural iron, acquired from the ENDF/B-VII.1 library and post-processed with NJOY2016.

8.2 Detector Responses for Time-Of-Flight Problem 1

The total number of reactions and the time-dependent detector response were computed for different energy discretization strategies for 100, 200, 300, 400, and 500 energy degrees-of-freedom. The analytical solutions were computed for two detector distances: 10 cm and 100 cm. For the detector distance of 10 cm, linearly-spaced time bins were placed between 0 and 10^{-7} s. For the detector distance of 100 cm, linearly-spaced time bins were placed between 0 and $\times 10^{-6}$ s. The reference “continuous-energy" solution for this time-of-flight problem used 100,000 logarithmically-spaced groups.

Figures 8.3 and 8.4 show the detector response at a distance of 10 cm, using 1000 time bins, with 500 energy-degrees-freedom for each of the various energy discretization strategies. Figures 8.5 and 8.6 show the detector response at a distance of 10 cm, using 100 time bins, with 500 energy-degrees-freedom for each of the various energy discretization strategies.

Similarly, Figures 8.7 and 8.8 show the detector response at a distance of 100 cm, using 1000 time bins, with 500 energy-degrees-freedom for each of the various energy discretization strategies. Figures 8.9 and 8.10 show the detector response at a distance of 100 cm, using 100 time bins, with 500 energy-degrees-freedom for each of the various energy discretization strategies.

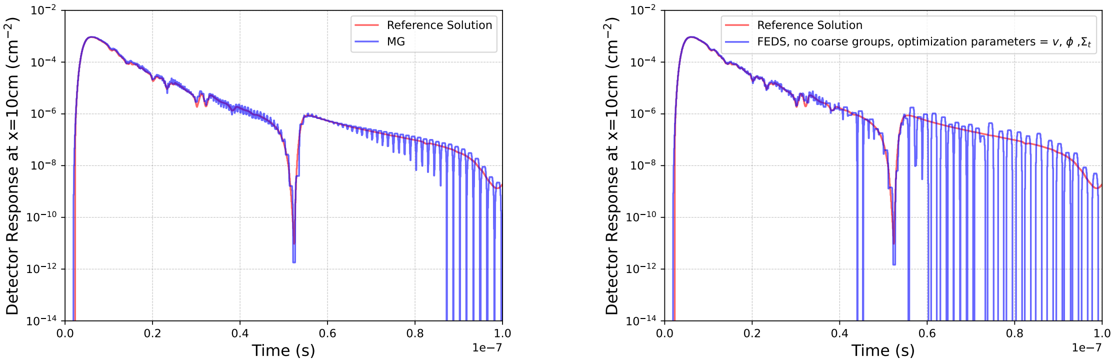

(a) MG, logarithmically-spaced

(b) FEDS, optimized using v, ϕ, Σ

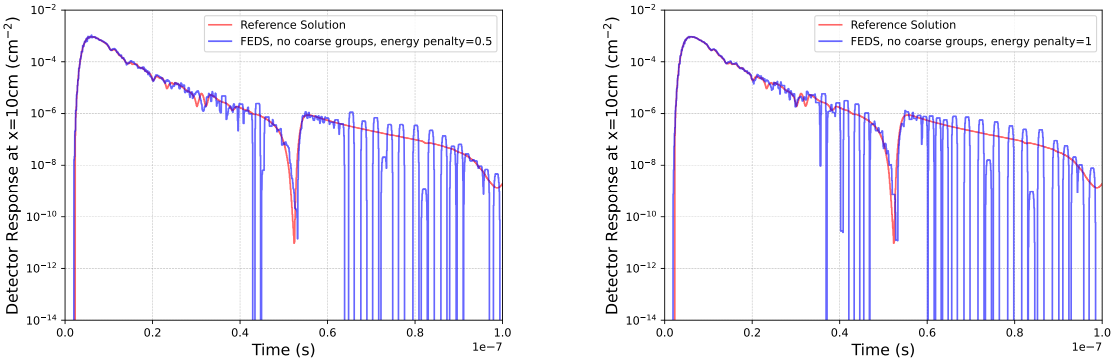

(c) FEDS, energy penalty = 0.5

(d) FEDS, energy penalty = 1

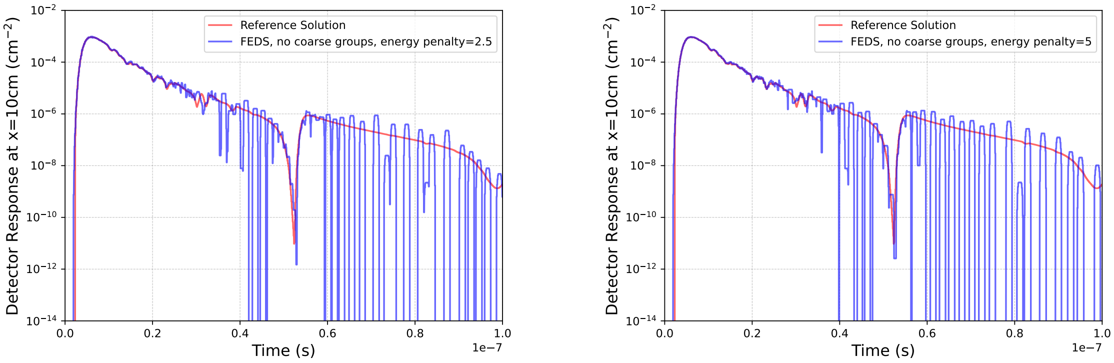

(e) FEDS, energy penalty = 2.5

(f) FEDS, energy penalty = 5

Figure 8.3: Detector response for different energy discretizations. These solutions are based on a detector distance of 10 cm with 1000 linearly-spaced time bins.

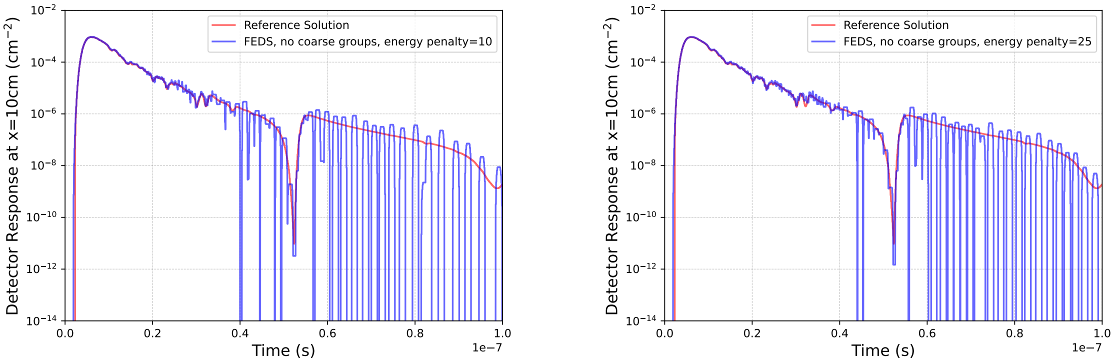

(a) FEDS, energy penalty = 10

(b) FEDS, energy penalty = 25

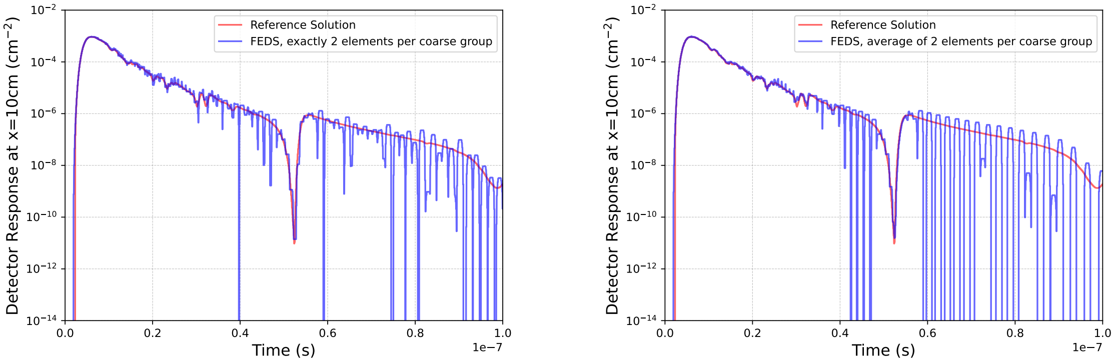

(c) FEDS, exactly 2 elements per coarse group

(d) FEDS, avg. of 2 elements per coarse group

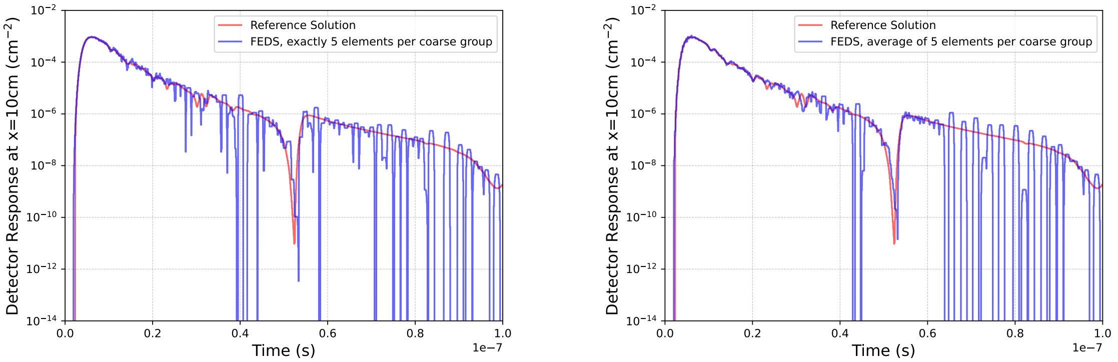

(e) FEDS, exactly 5 elements per coarse group

(f) FEDS, avg. of 5 elements per coarse group

Figure 8.4: This is a continuation of Figure 8.3. Detector response for different energy discretizations. These solutions are based on a detector distance of 10 cm with 1000 linearly-spaced time bins.

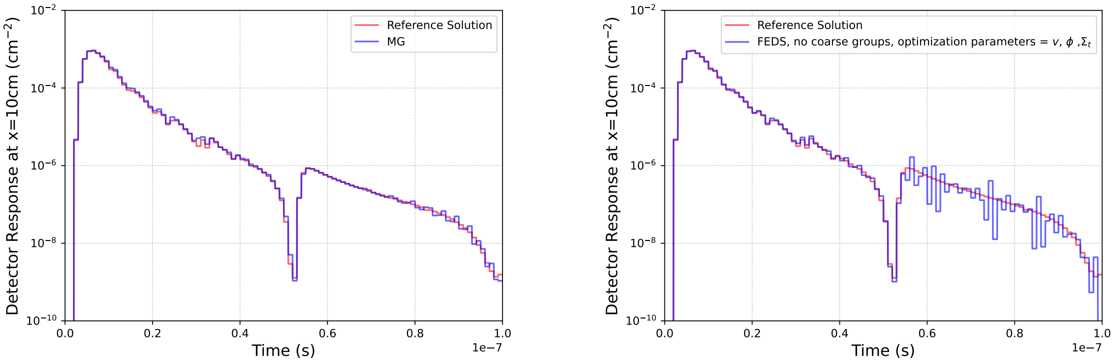

(a) MG, logarithmically-spaced

(b) FEDS, optimized using v, ϕ, Σ

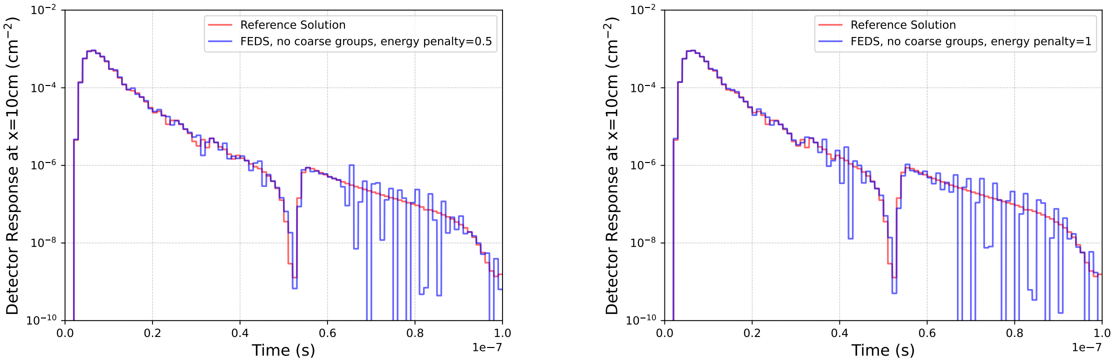

(c) FEDS, energy penalty = 0.5

(d) FEDS, energy penalty = 1

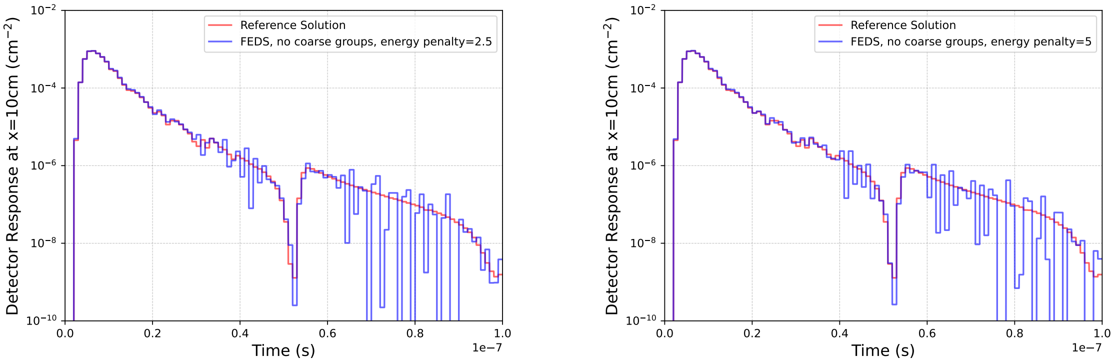

(e) FEDS, energy penalty = 2.5

(f) FEDS, energy penalty = 5

Figure 8.5: Detector response for different energy discretizations. These solutions are based on a detector distance of 10 cm with 100 linearly-spaced time bins.

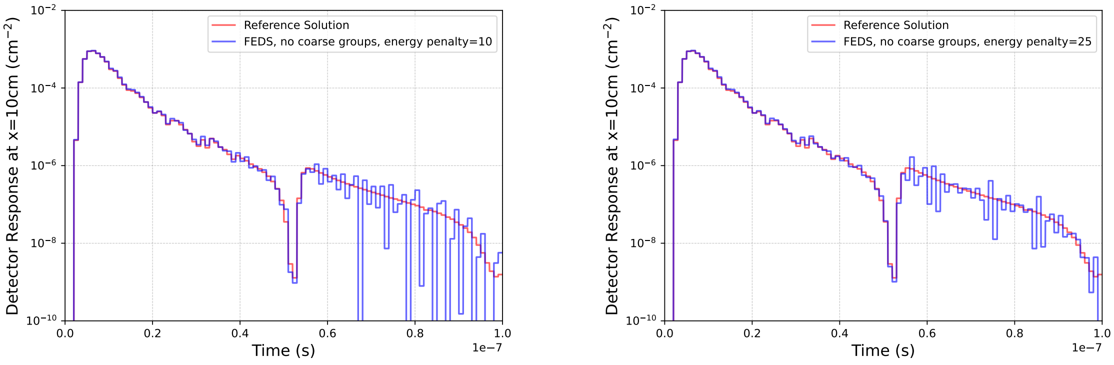

(a) FEDS, energy penalty = 10

(b) FEDS, energy penalty = 25

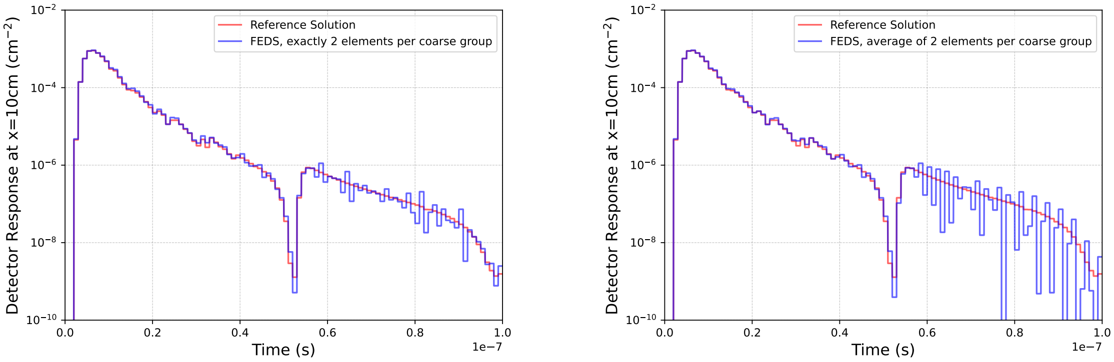

(c) FEDS, exactly 2 elements per coarse group

(d) FEDS, avg. of 2 elements per coarse group

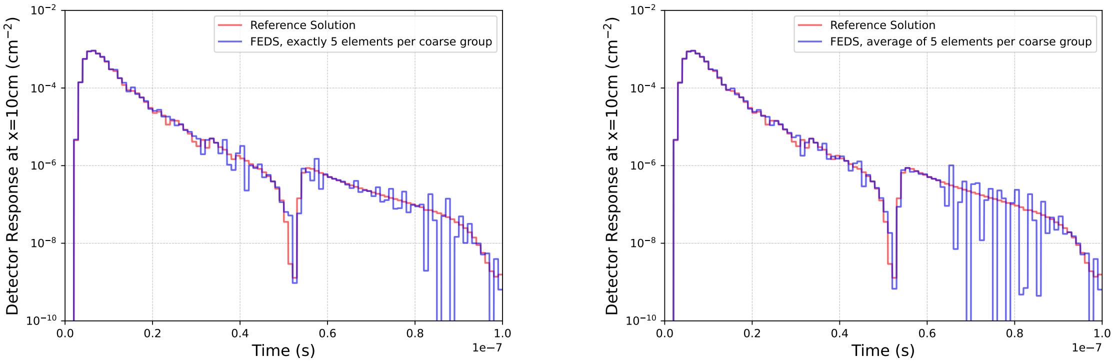

(e) FEDS, exactly 5 elements per coarse group

(f) FEDS, avg. of 5 elements per coarse group

Figure 8.6: This is a continuation of Figure 8.5. Detector response for different energy discretizations. These solutions are based on a detector distance of 10 cm with 100 linearly-spaced time bins.

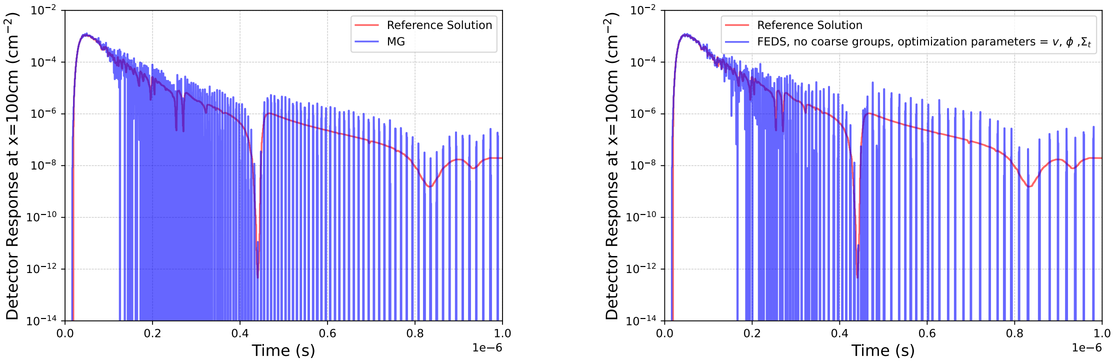

(a) MG, logarithmically-spaced

(b) FEDS, optimized using v, ϕ, Σ

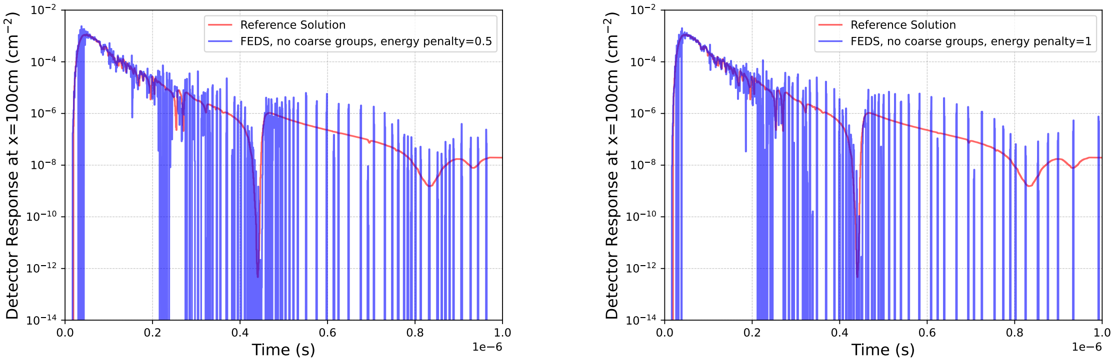

(c) FEDS, energy penalty = 0.5

(d) FEDS, energy penalty = 1

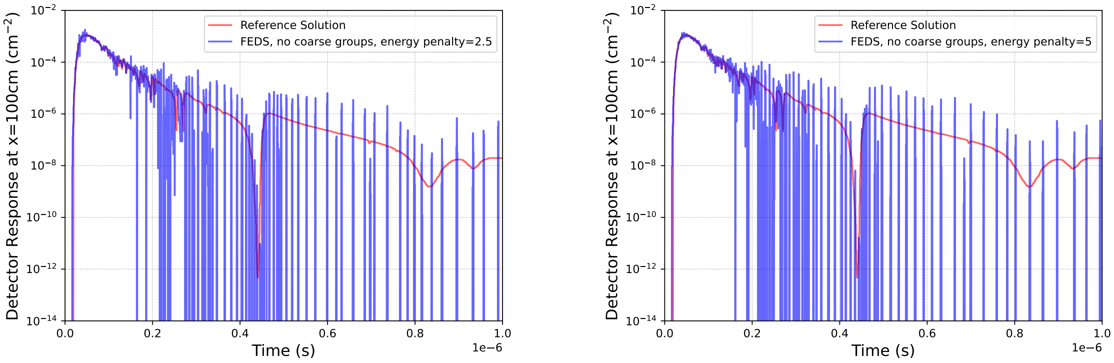

(e) FEDS, energy penalty = 2.5

(f) FEDS, energy penalty = 5

Figure 8.7: Detector response for different energy discretizations. These solutions are based on a detector distance of 100 cm with 1000 linearly-spaced time bins.

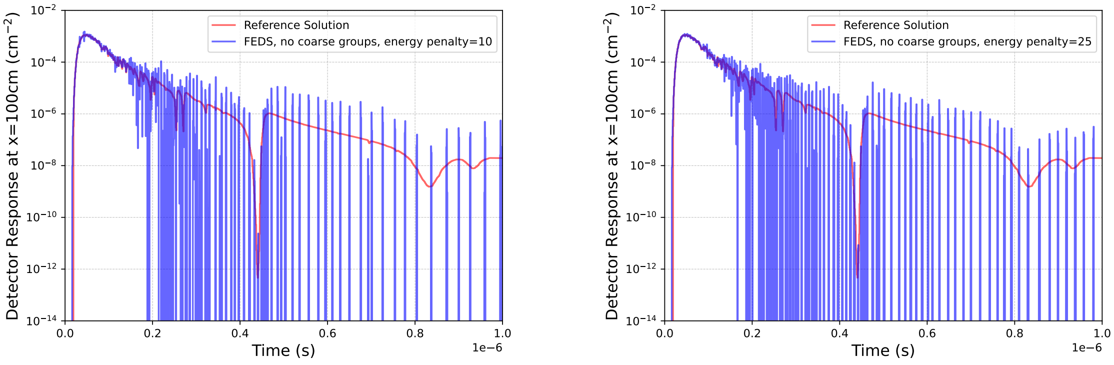

(a) FEDS, energy penalty = 10

(b) FEDS, energy penalty = 25

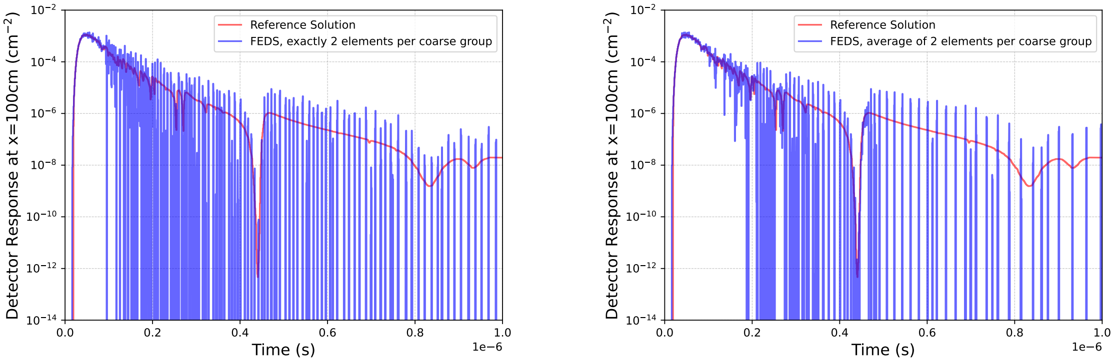

(c) FEDS, exactly 2 elements per coarse group

(d) FEDS, avg. of 2 elements per coarse group

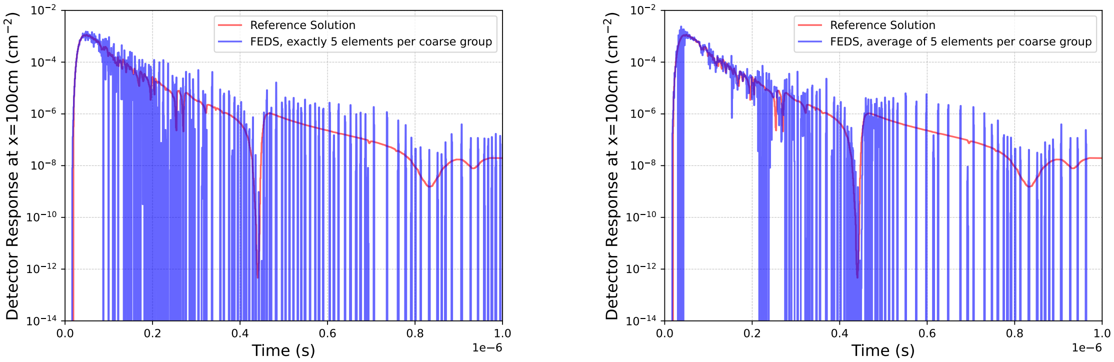

(e) FEDS, exactly 5 elements per coarse group

(f) FEDS, avg. of 5 elements per coarse group

Figure 8.8: This is a continuation of Figure 8.7. Detector response for different energy discretizations. These solutions are based on a detector distance of 100 cm with 1000 linearly-spaced time bins.

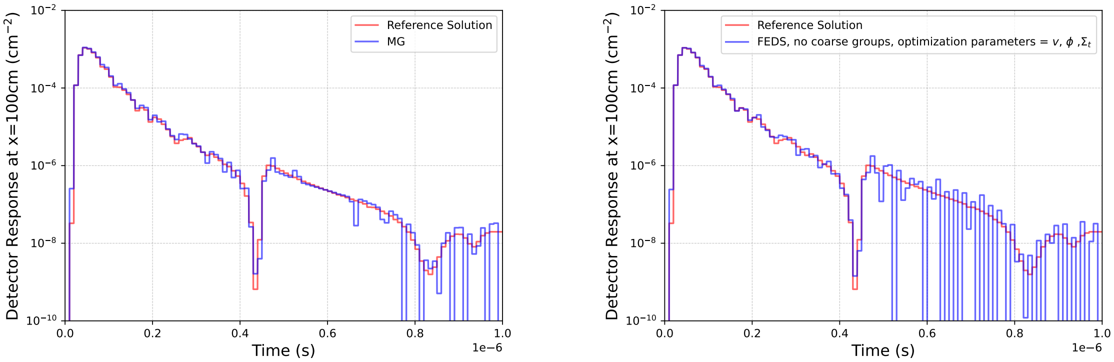

(a) MG, logarithmically-spaced

(b) FEDS, optimized using v, ϕ, Σ

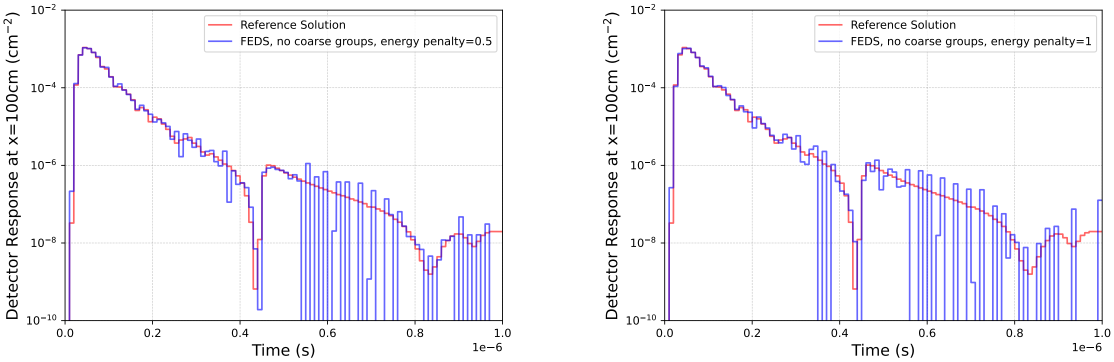

(c) FEDS, energy penalty = 0.5

(d) FEDS, energy penalty = 1

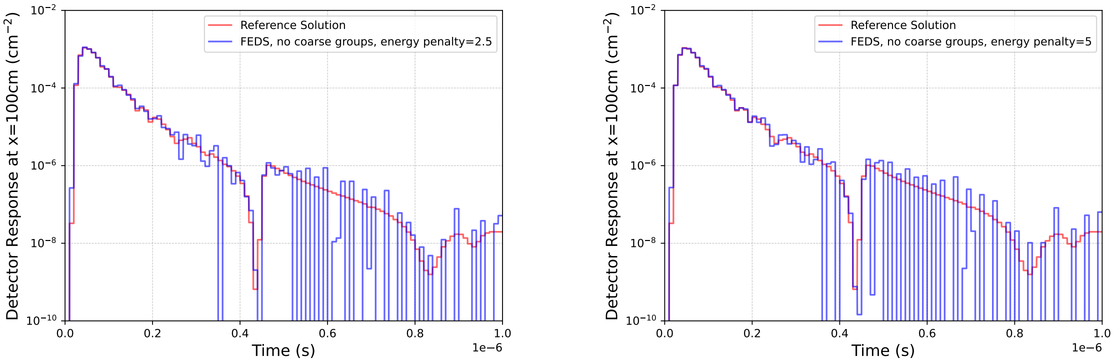

(e) FEDS, energy penalty = 2.5

(f) FEDS, energy penalty = 5

Figure 8.9: Detector response for different energy discretizations. These solutions are based on a detector distance of 100 cm with 100 linearly-spaced time bins.

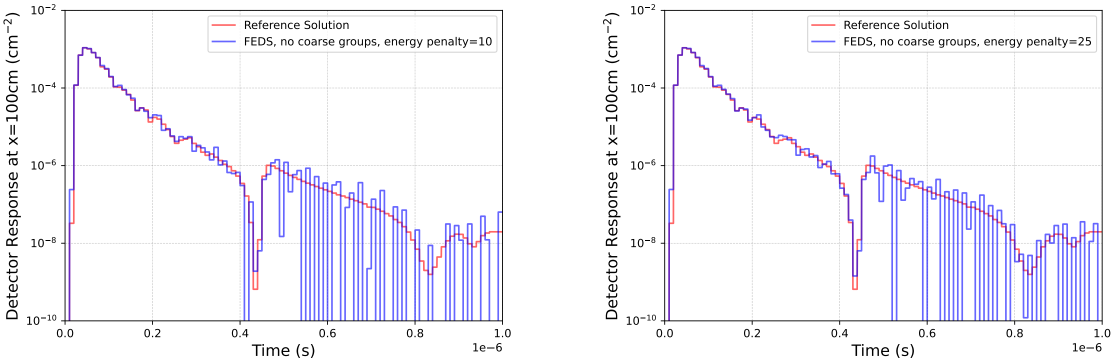

(a) FEDS, energy penalty = 10

(b) FEDS, energy penalty = 25

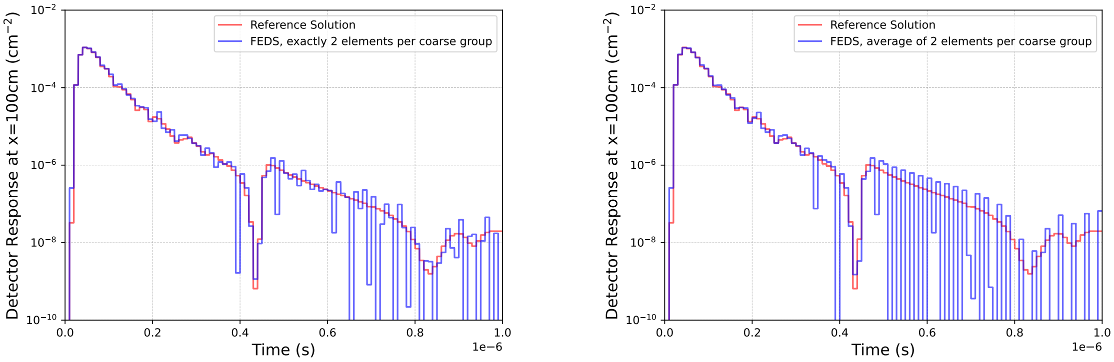

(c) FEDS, exactly 2 elements per coarse group

(d) FEDS, avg. of 2 elements per coarse group

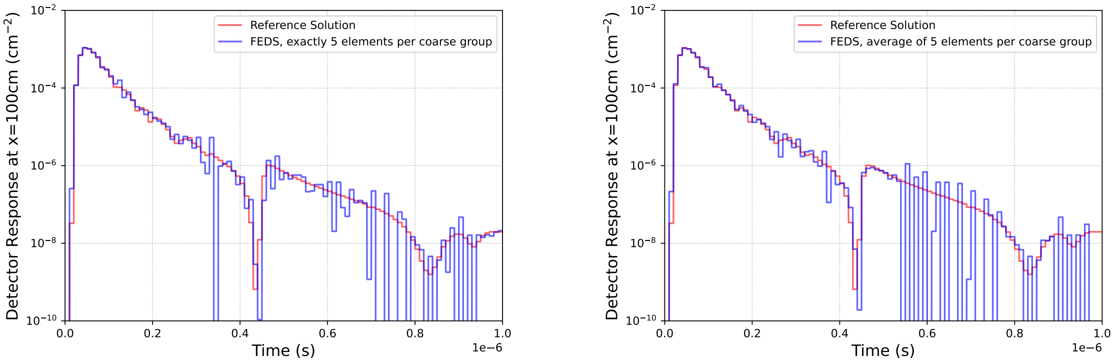

(e) FEDS, exactly 5 elements per coarse group

(f) FEDS, avg. of 5 elements per coarse group

Figure 8.10: This is a continuation of Figure 8.9. Detector response for different energy discretizations. These solutions are based on a detector distance of 100 cm with 100 linearly-spaced time bins.

8.3 Error Comparisons for Time-Of-Flight Problem 1

The L_2 error norm for a discretization was determined by comparing the result to a reference solution. The reference solution used 100,000 logarithmically-spaced energy groups. Specifically, the L_2 error was for computed for 1000 linearly-spaced time bins as

$$||\varepsilon||_2 = \sqrt{\frac{\sum_b |u_{d,b} - u_{r,b}|^2}{\sum_b |u_{r,b}|^2}}$$

where $u_{d,b}$ is the energy-discretized analytic estimate for time bin b and $u_{r,b}$ is the reference solution value for time bin b. The consequence of this error metric is that if a neutron is simulated with a sufficiently inaccurate speed, then that neutron will appear in the wrong time bin and therefore introduce errors in two seperate time bins. For this reason, we also computed the L_2 error norm for 100 linearly-spaced time bins, since it is slightly more forgiving of inaccurate speeds. It should also be noted that this magnitude of this error metric is mostly impacted by time bins with largest absolute errors, not the time bins with the largest relative errors.

Figures 8.11 and 8.12 compare the L_2 error norms for the detector response for various energy discretizations at a detector distance of 10 cm, using 1000 time bins and 100 time bins, respectively. Figures 8.13 and 8.14 compare the L_2 error norms for the detector response for various energy discretizations at a detector distance of 100 cm, using 1000 time bins and 100 time bins, respectively.

The results from these time-of-flight simulations demonstrate that using large energy penalty values are an effective strategy for improving the performance of FEDS discretizations for single-material time-of-flight simulations. Using large energy penalty values usually resulted in better time-dependent detector responses compared to logarithmically-spaced MG for various detector distances and number of time bins. However, note that using large energy penalty values gradually degrades the performance of FEDS for steady-state quantities of interest. Figure 8.15 compares the L_2 error norms for total number of reactions occuring in the iron slab for various energy discretizations. For this steady-state quantity of interest, using an energy penalty of 25 provided the least accurate result compared to other FEDS discretizations, however it was still more accurate than using MG, especially when 500 energy degrees-of-freedom were used. Since iron has resonances in the keV and MeV range, where the neutron flux is largest, FEDS was expected to compute reaction rates more accurately than MG; the results in Figure 8.15 agree with these expectations.

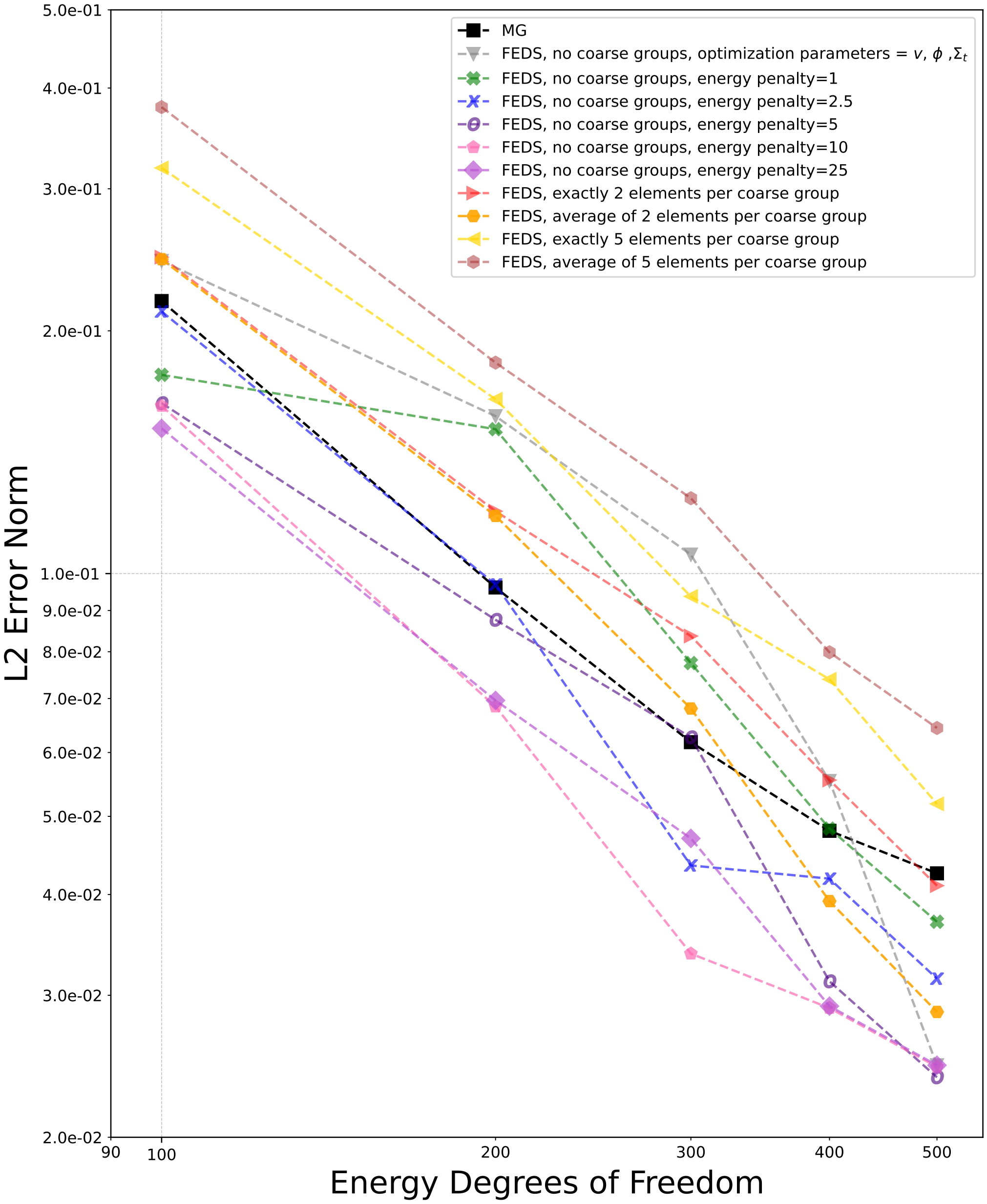

Figure 8.11: Error convergence for time-dependent detector response for 1000 time bins with the detector placed 10 cm from the source.

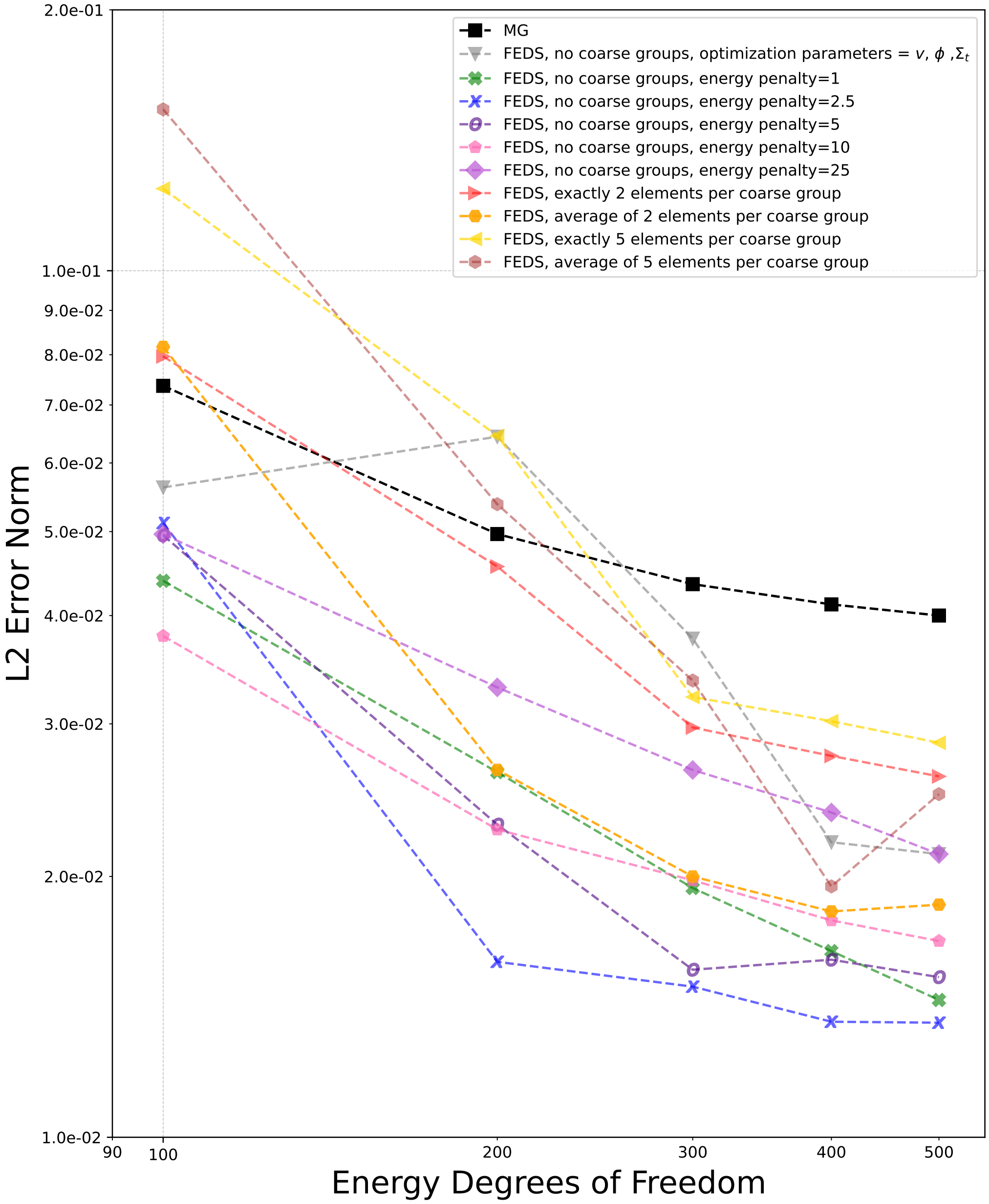

Figure 8.12: Error convergence for time-dependent detector response for 100 time bins with the detector placed 10 cm from the source.

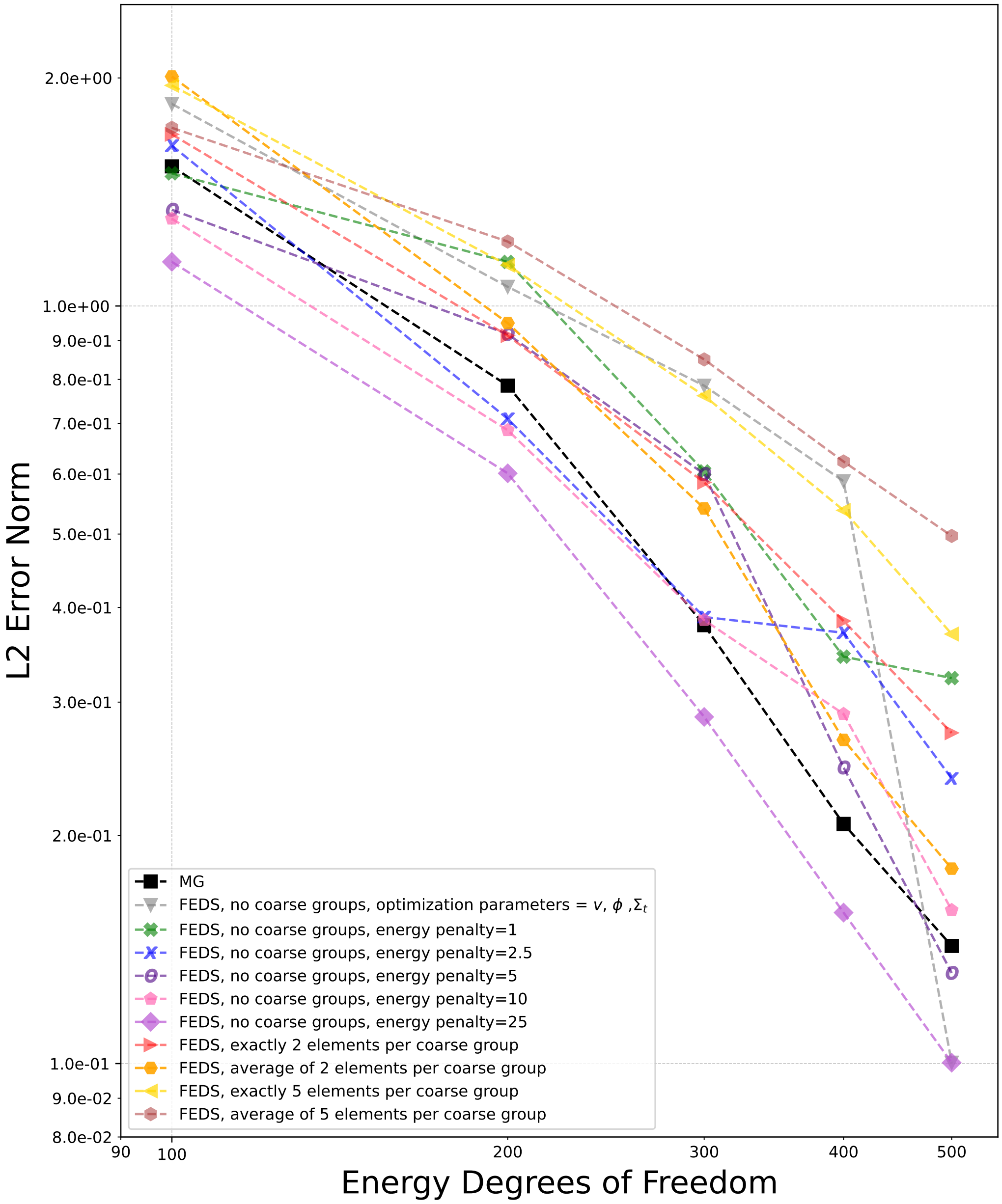

Figure 8.13: Error convergence for time-dependent detector response for 1000 time bins with the detector placed 100 cm from the source.

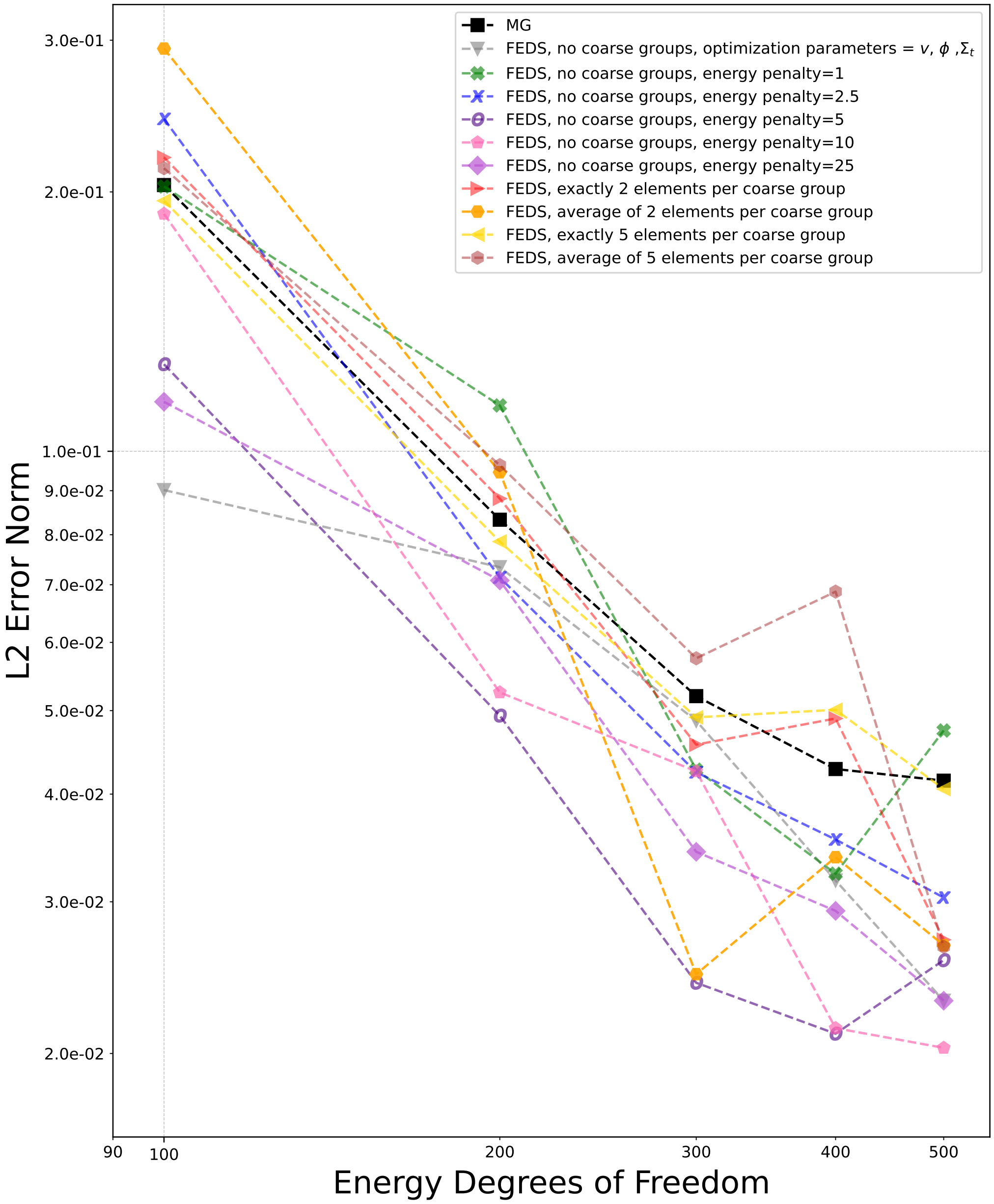

Figure 8.14: Error convergence for time-dependent detector response for 100 time bins with the detector placed 100 cm from the source.

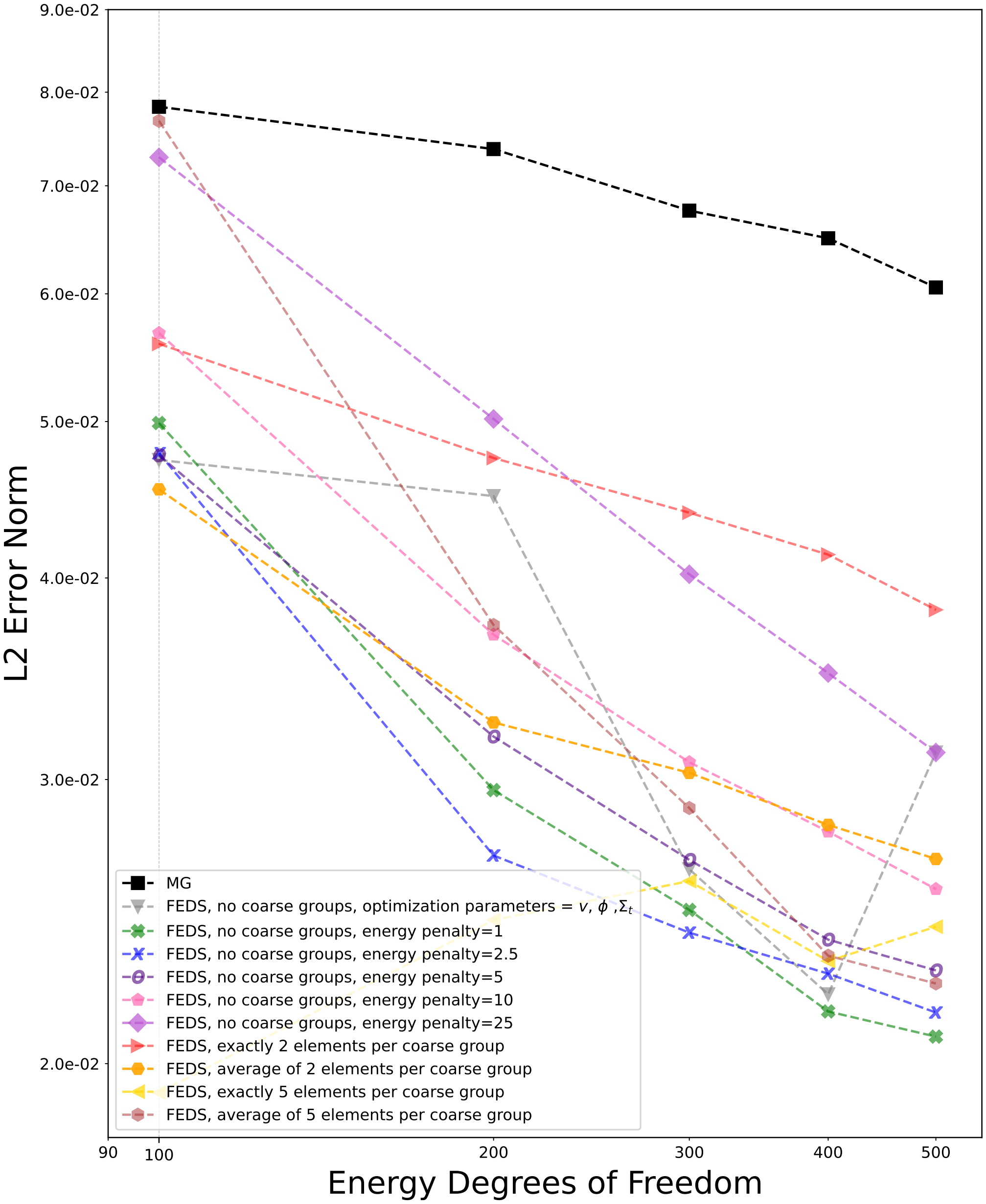

Figure 8.15: Error convergence for total number of reactions in the iron slab.

9. TIME-OF-FLIGHT PROBLEM 2: A MULTILAYER SLAB

In this chapter, we test the performance of FEDS for a multi-material time-of-flight problem. This creates an additional challenge for discontiguous energy methods, because a discontiguous energy discretization that is ideal for one material may not be ideal for other materials. However, Till [3] and Lou [36] have previously demonstrated that FEDS designed to handle this challenge better than other discontiguous energy methods.

9.1 Description of Time-Of-Flight Problem 2

This test problem consists of a 1D multilayer slab geometry, with a 14.1 MeV neutron source incident normally to the multilayer slab. The first layer consists of 4 cm of U-235 with a density of 19 g/cm^3. The second layer consists of 3 cm of Al-27 with a density of 2.7 g/cm^3. The third layer consists of a 3 cm thick slab of Fe-56 with a density of 7.8 g/cm^3. Finally, a detector is placed adjacent to the right boundary of the multilayer slab. Figure 9.1 shows the physical layout of the problem. Note, the slabs are infinite in the $\hat{y}$ and $\hat{z}$ dimensions.

The neutron source is pulsed according to a time-dependent gaussian distribution,

$$\frac{1}{\sigma\sqrt{2\pi}}e^{-\frac{1}{2}(\frac{t-t_o}{\sigma})^2}$$

where σ = 0.2 ns and t_o = 1 ns. The detector response was measured for 2000 time bins between 0 and 20 ns.

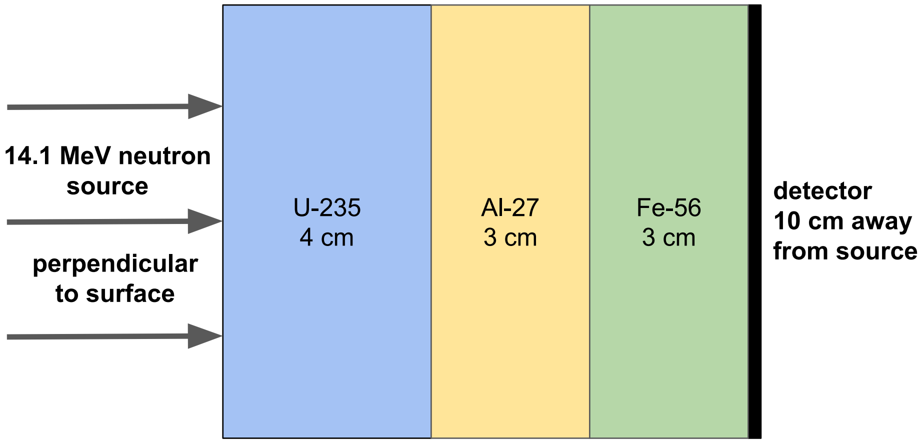

Figure 9.1: Physical configuration of the multilayer slab time-of-flight problem.

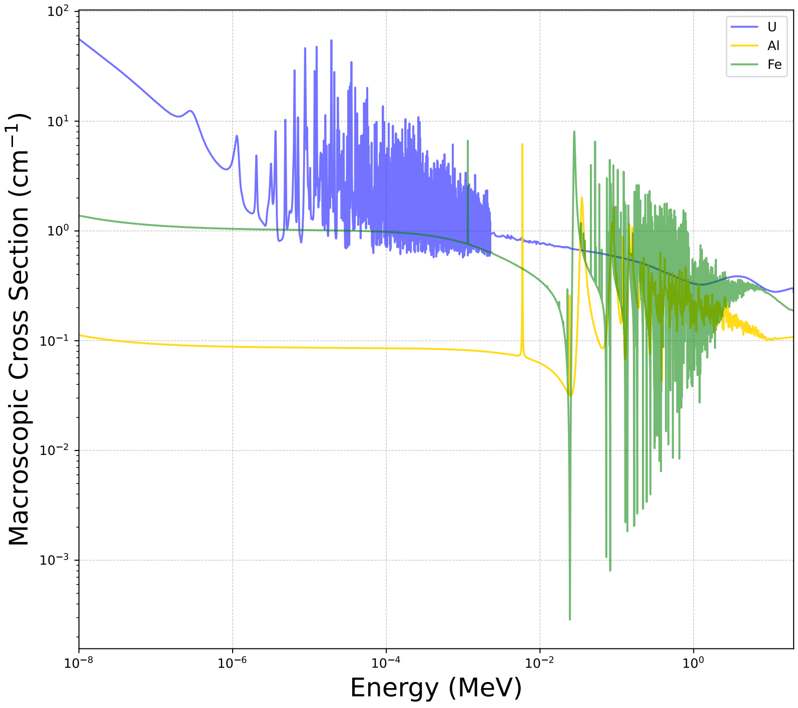

Figure 9.2: Macroscopic cross sections for three layers, acquired from the ENDF/B-VII.1 library and post-processed with NJOY2016.

We wish to evaluate the following quantities of interest:

1. criticality
2. the time-dependent fission rate
3. the energy-integrated detector response as a function of time.

The microscopic cross sections were extracted from ENDF/B-VII.1 [14], and post-processed with NJOY2016 [15] in order to generate the continuous-energy, MG and FEDS cross sections. Figure 9.2 shows the macroscopic cross sections for three materials in the problem. The MG and FEDS cross sections were generated using Bondarenko iterations. However, the cross sections for the three materials were generated independently. For example, when generating the MG or FEDS cross sections for uranium, the weighting spectrum was only impacted by the cross sections for uranium, and the cross sections for iron and aluminum neglected.

For the MG discretizations, we simply partitioned the energy domain into logarithmically-spaced groups. Similarly, for FEDS discretizations that used coarse groups, we also partitioned the energy domain into logarithmically-spaced coarse groups. Also, note that coarse groups were not used for the FEDS energy discretization that used energy penalties or used v as an additional optimization parameter.

A Python package was created to run discrete-ordinates S_N neutron transport simulations. For the steady-state simulations, the code used a cell-centered diamond-difference spatial discretization with 500 spatial cells. The angular domain was discretized into 256 polar angles, and 13^{th}-order Gauss-Lobatto quadrature was used.

For the time-dependent simulations, the code used a Crank-Nicolson temporal discretization scheme with 2000 time steps between 0 and 20 ns, as well as 120 spatial cells, 32 polar angles, and 13^{th}-order Gauss-Lobatto quadrature.

9.2 Reference Solutions for Time-of-Flight Problem 2

The Monte Carlo N-Particle Transport Code 6 (MCNP6) was used to generate reference solutions, by sampling from continuous-energy cross sections [42]. A MCNP6 criticality, "kcode", simulation was conducted to determine the value of k_{eff}, which was found to be 0.87452 ± 0.00003. A separate MCNP6 simulation was used to determine the time-dependent detector response and fission rate. The detector response was determined using the "F2" surface fluence tally and 2000 linearly-spaced time bins. The fission rate was determined using the "F4" cell fluence tally, a cross section multiplier for U-235 fission reactions, "FM4 -1 92235 -6", and 2000 linearly-spaced time bins.

Figure 9.3, Figure 9.4, and Figure 9.5 show the reference MCNP6 fluences, detector response, and time-dependent fission rate, respectively.

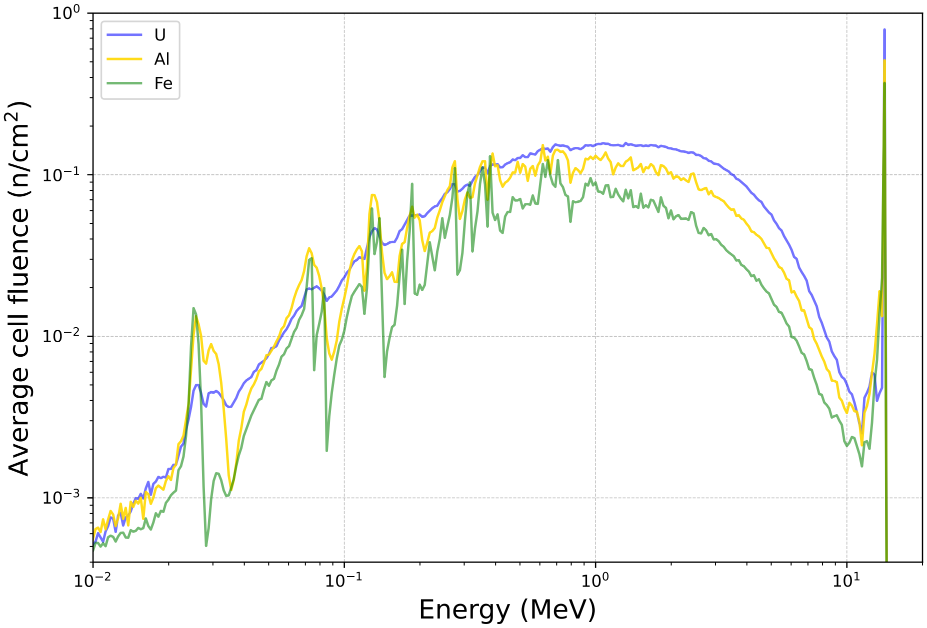

Figure 9.3: MCNP6 fluences, obtained by using a separate cell fluence tally for each material.

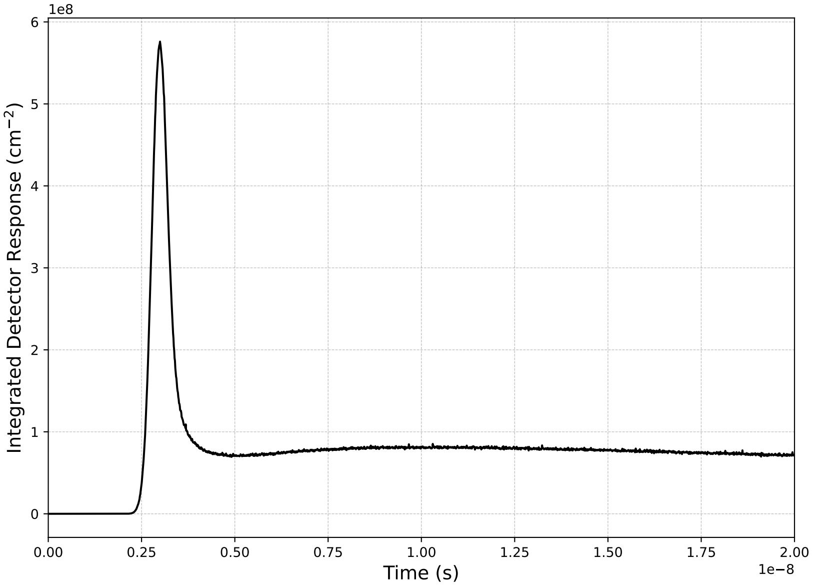

Figure 9.4: Reference detector response, based on MCNP6 simulation.

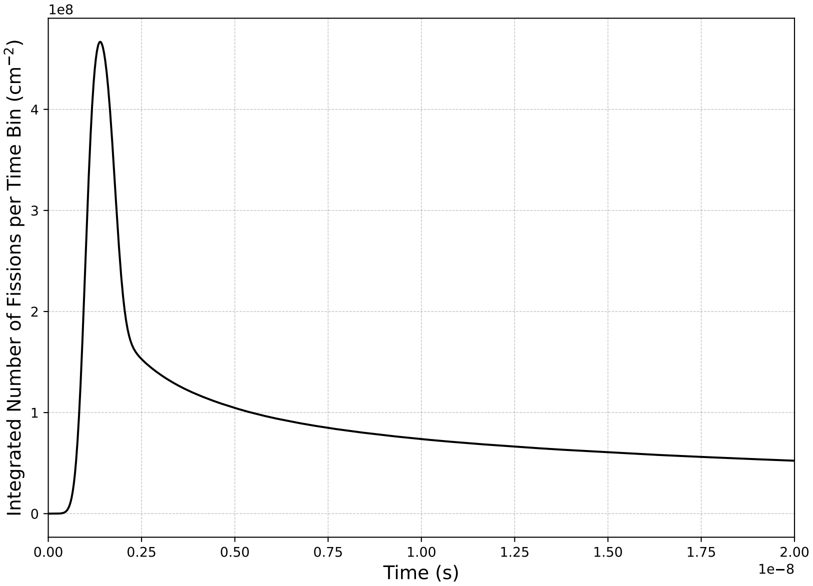

Figure 9.5: Reference time-dependent fission rate, based on MCNP6 simulation.

9.3 Error Comparisons for Time-Of-Flight Problem 2

The L_2 error norm for an energy discretization was computed by comparing the simulation results to the reference MCNP6 solution at 2000 linearly-spaced time bins as

$$||\varepsilon||_2 = \sqrt{\frac{\sum_b |u_{d,b} - u_{r,b}|^2}{\sum_b |u_{r,b}|^2}}$$

where $u_{d,b}$ is the energy-discretized value for time bin b and $u_{r,b}$ is the reference value for time bin b. The consequence of this error metric is that if a neutron is simulated with a sufficiently inaccurate speed, then that neutron will appear in the wrong time bin and therefore introduce errors in two seperate time bins. Another problem with this error metric is that spatial, angular, and temporal discretization can also cause a neutron to appear in the wrong time bin. For this reason, we also computed the L_2 error norm for a single time bin between 0 and 20 ns. The spatial, angular, and temporal discretization error would have a smaller impact in this case.

The simulation errors were compared for 50, 100, 200, and 300 energy degrees-of-freedom for each energy discretization strategy. Figures 9.6 and 9.7 compare the L_2 error norms for the detector response for various energy discretizations, using 2000 time bins and 1 time bin, respectively. Figures 9.8 and 9.9 compare the L_2 error norms for the fission rate for various energy discretizations, using 2000 time bins and 1 time bin, respectively. Lastly, Figure 9.10 compare the relative error for k_{eff} for various energy discretizations. It is important to note that a method can achieve an accurate estimate of the detector response for only 1 time bin simply by luck, due to error cancellations. Similarly, a method can also achieve an accurate estimate of k_{eff} simply by luck, due to error cancellations.

A common pattern that was observed for the results for this test problem is that FEDS discretizations that used exactly 2 elements in each coarse group were consistently more accurate than MG when 200 or 300 energy degrees-of-freedom were used for various steady-state and time-dependent quantities of interest. In general, when 300 energy degrees-of-freedom were used, most of the FEDS energy discretization strategies were more accurate than MG for various steady-state and time-dependent quantities of interest, especially when using an energy penalty equal to one with no coarse groups.

It is important to note, that for time-of-flight simulations with 2000 time bins the spatial, angular and temporal discretization error were non-negligible. Based on convergence studies, the spatial discretization error for time-of-flight simulations with 2000 time bins is estimated to be less than 1%, the temporal discretization error was also estimated to be less than 1%, the angular discretization error was estimated to be less than 1%, and the truncation error for the 13^{th}-order Legendre polynomial expansion was estimated to be around 1%.

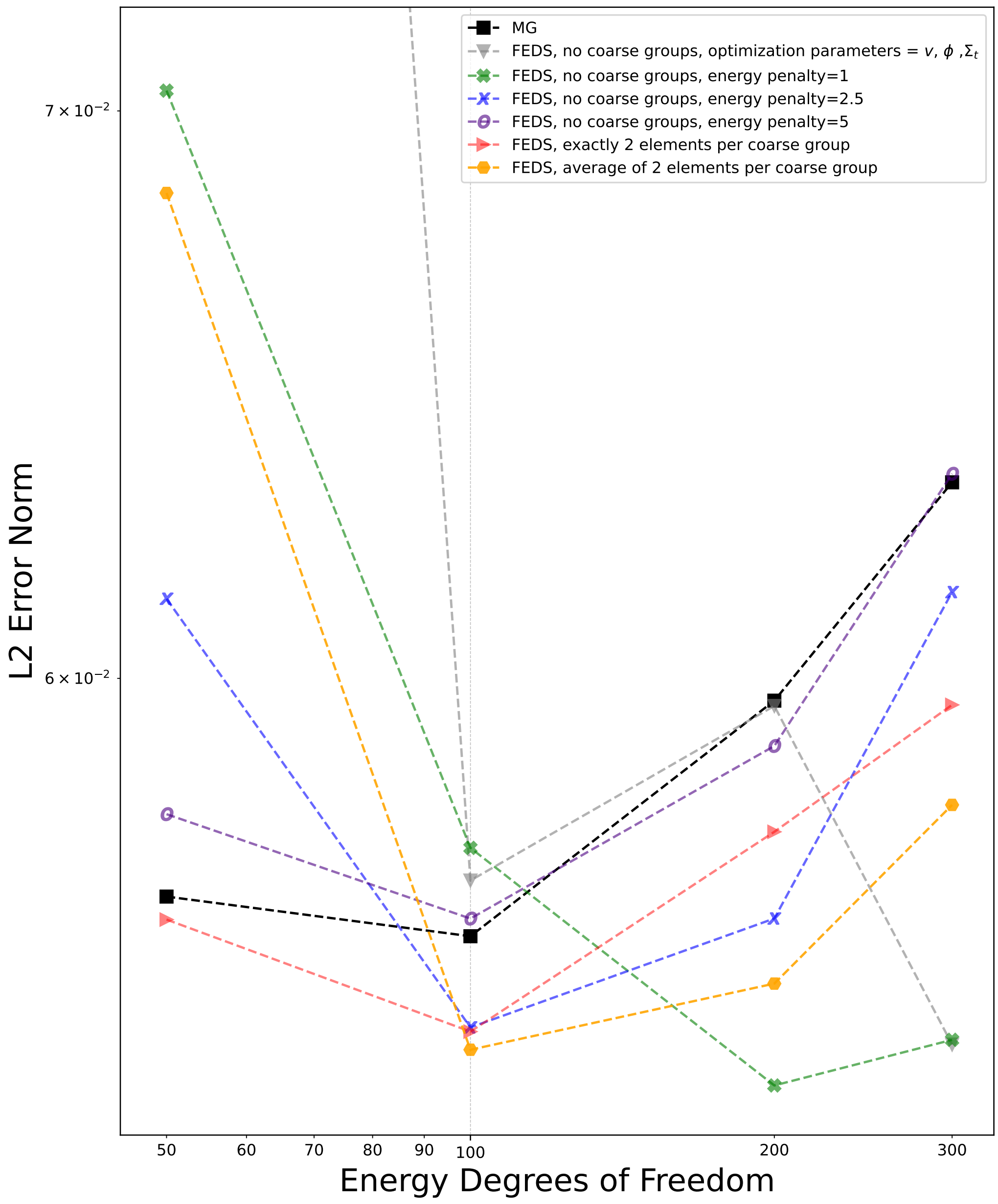

Figure 9.6: Error comparisons for time-dependent detector response for 2000 time bins.

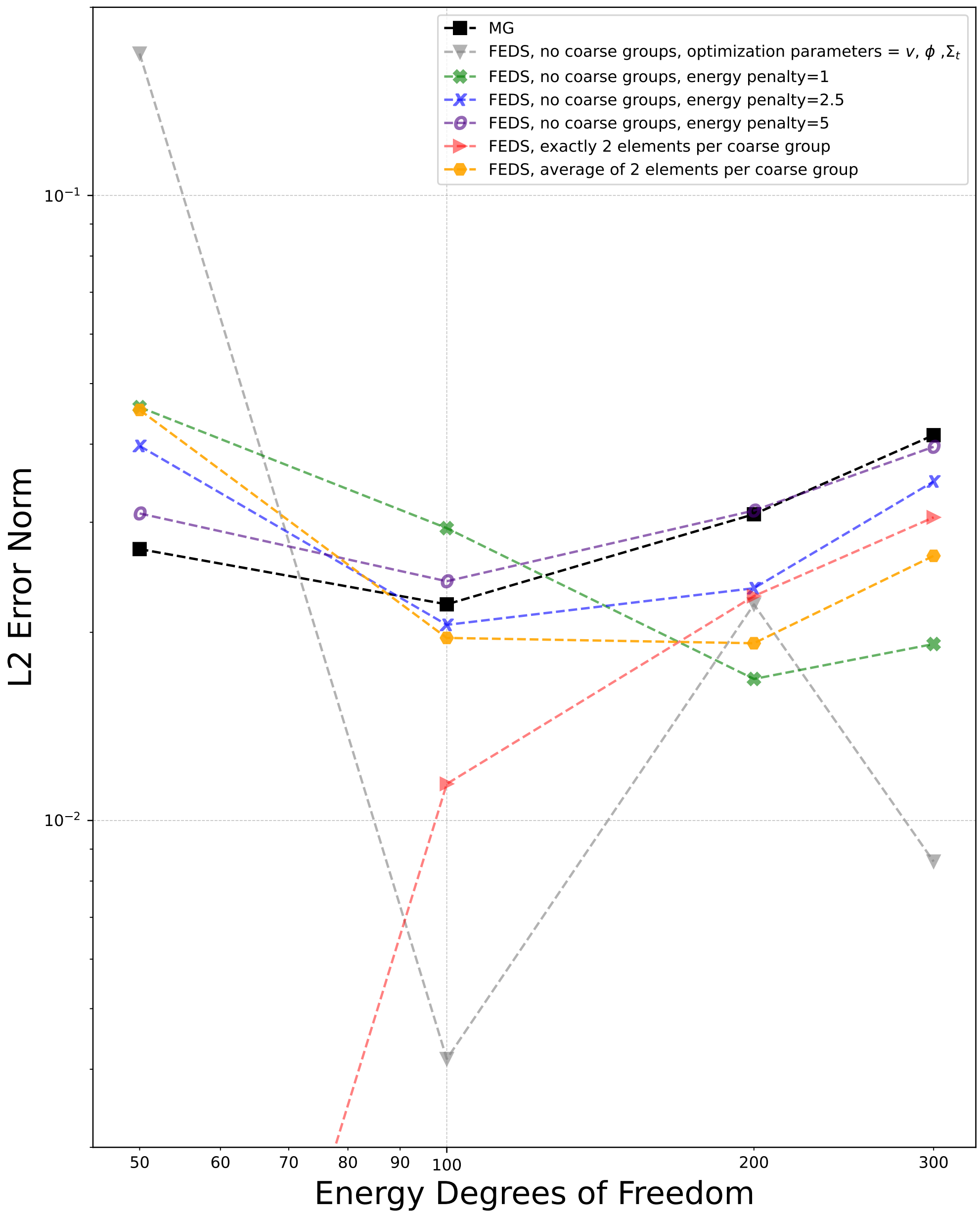

Figure 9.7: Error comparisons for time-dependent detector response for 1 time bin.

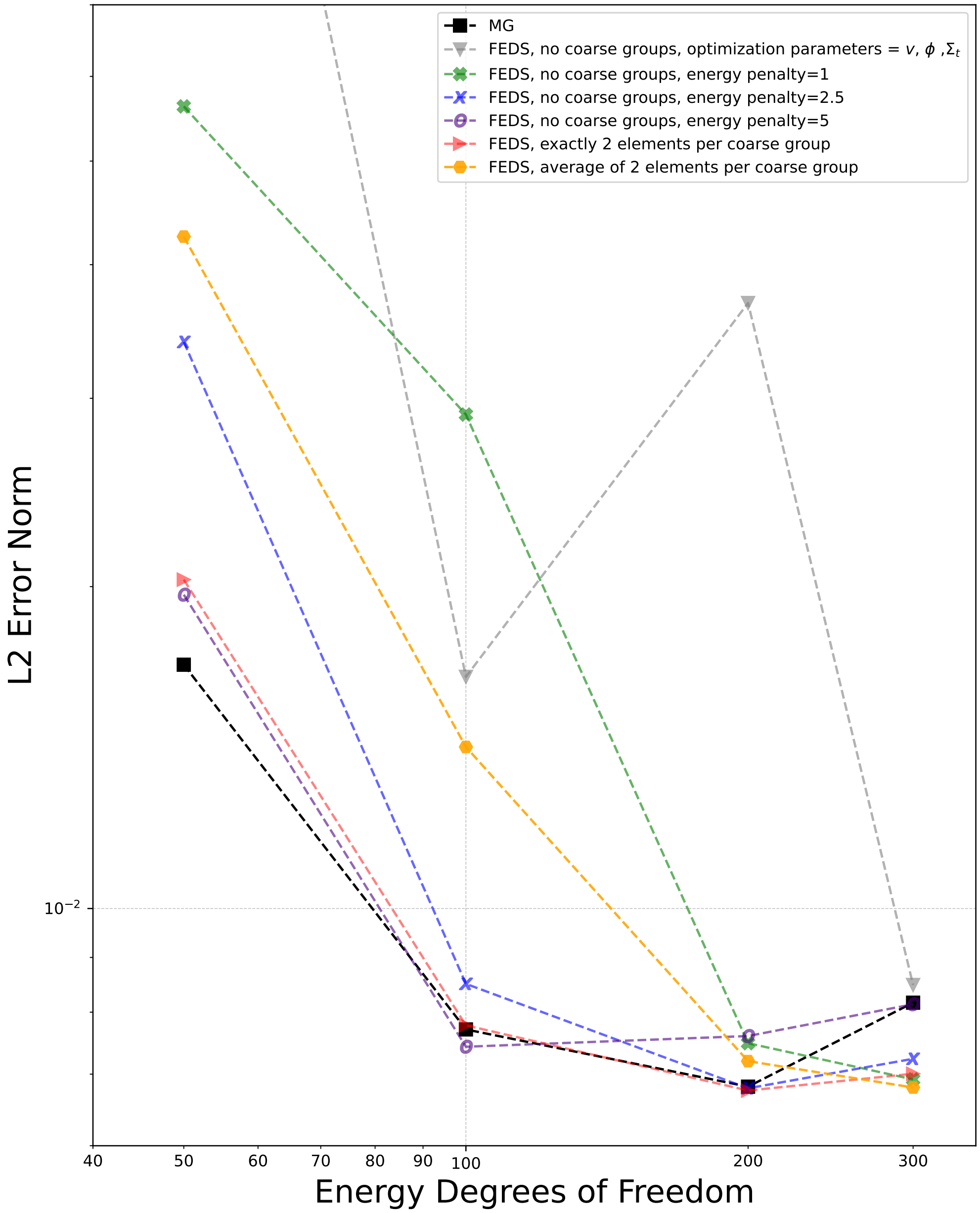

Figure 9.8: Error comparisons for time-dependent fission rate for 2000 time bins.

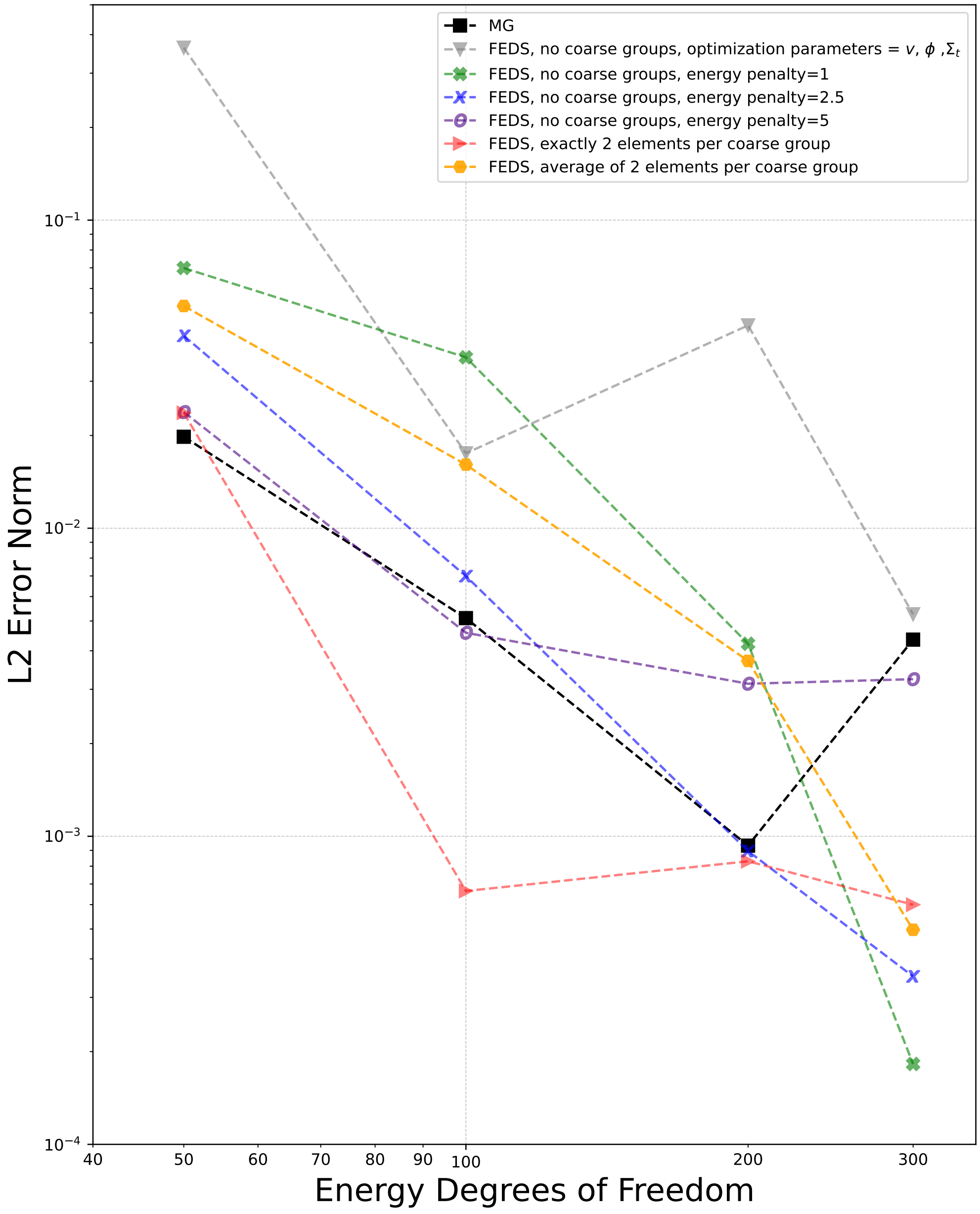

Figure 9.9: Error comparisons for time-dependent fission rate for 1 time bin.

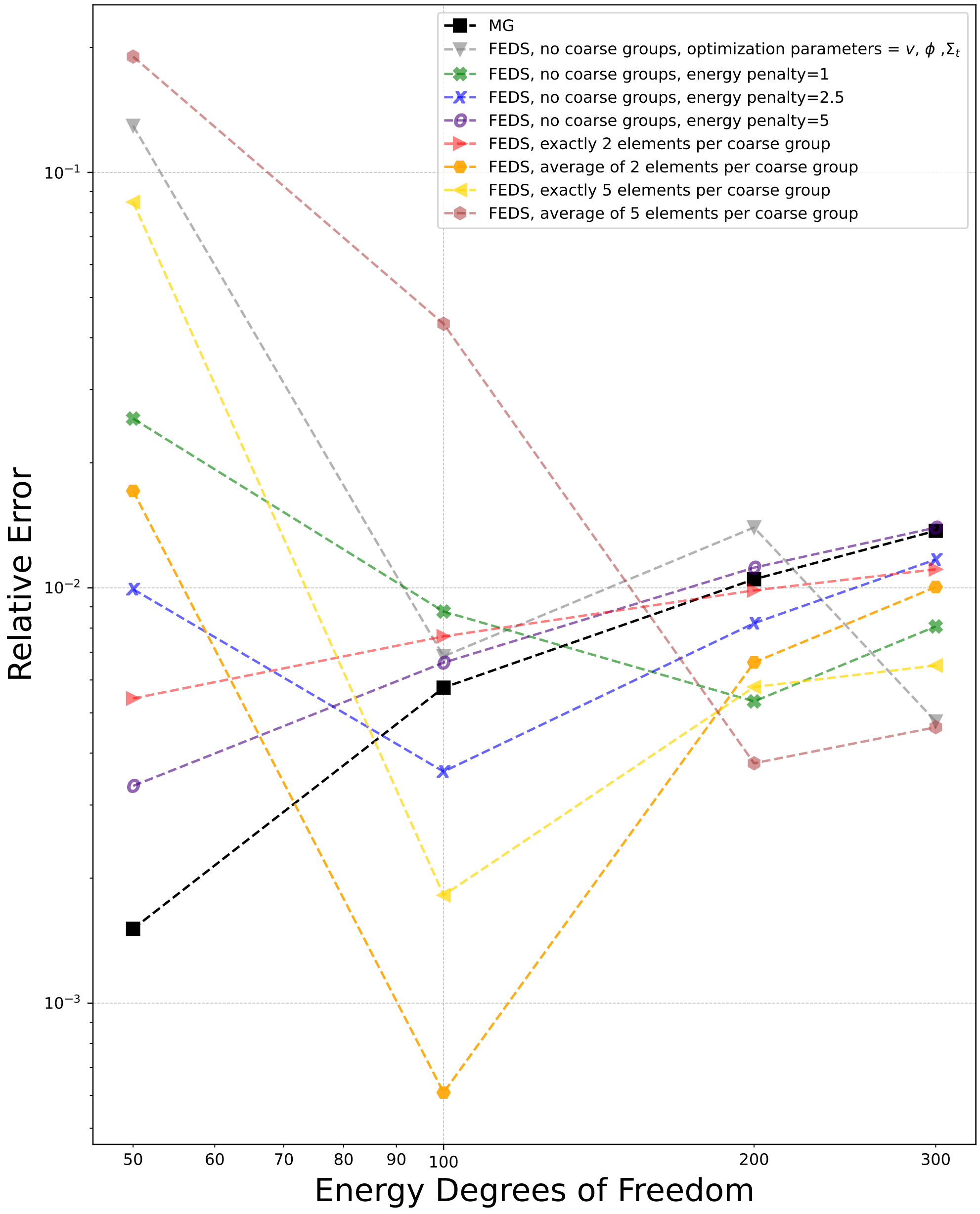

Figure 9.10: Error comparisons for k_{eff}.

10. CONCLUSION

In this study, we introduced the coarse-scattering (CS) method, and proved its ability to reduce the computational time required to model scattering in multigroup (MG) simulations. We applied the CS method to a slab-geometry criticality simulation, and showed that it was able to reduce the overall runtime of the simulation by almost a factor of four. Furthermore, we proved that the CS method is able to conserve particle balance as long as the the CS scattering spectrum and CS fission spectrum are recomputed in the last iteration.

Also in this study, we showed that finite-element with discontiguous-support (FEDS) method and the multigroup (MG) method have certain advantages and disadvantages for simulating time-of-flight problems. FEDS is inherently able to model cross sections more accurately, while MG inherently is able to model neutron speeds more accurately. For this reason, there may be some time-of-flight problems where the MG method will always produce more accurate simulations, or vice-versa. We compared a wide variety of FEDS energy discretizations, and determined their performance for a single-material and a multi-material time-of-flight simulation. We found that either using FEDS energy discretizations with large energy penalties or FEDS energy discretizations with a small number of elements per coarse group performed best for time-of-flight simulations. The FEDS energy discretizations that used energy penalties were usually more accurate than the MG simulations for the single-material and the multi-material time-of-flight problems, for various detector distances and number of time bins. Also, the FEDS energy discretization that used exactly two FEDS elements in each coarse group was competitive with MG for the single-material time-of-flight problem and usually more accurate than MG for the multi-material time-of-flight problem. Another noticeable result from these test problems is that when very high energy penalty values were used, the accuracy of the FEDS simulations were similar to the accuracy of MG simulations.

A conservative strategy for generating FEDS energy discretizations for time-dependent neutron transport is to first create a MG grid that already provides reasonable estimates for various quantities of interests, then further partition each MG group into a few FEDS elements per group until the desired level of accuracy is achieved for various quantities of interest. However, it may be simpler and possibly more accurate to just generate a FEDS energy discretization using an appropriate energy penalty.

In the future, the use of energy penalties and coarse groups for time-dependent FEDS simulations should be further investigated, using even higher energy degrees-of-freedom as well as a wider variety of test problems. Also, there should be more investigations into possible modifications to the FEDS objective function and clustering algorithm. For example, it may be possible to limit the energy span of energy elements by modifying the connectivity graph used for hierarchical agglomerative clustering, and yield better results for time-dependent simulations.

REFERENCES

[1] A. T. Till , M. L. Adams, J. E. Morel, A Generalized Multigroup Method Based on Finite Elements, International Conference on the Physics of Reactors (PHYSOR) - The Role of Reactor Physics Toward a Sustainable Future, American Nuclear Society, Kyoto, Japan, 2014.

[2] A. T. Till, A Generalized Multigroup Method, Master's thesis, Texas A&M University (2014).

[3] A. T. Till, Finite Elements with Discontiguous Support for Energy Discretization in Particle Transport, Ph.D. thesis, Texas A&M University (2015).

[4] G. I. Bell, S. Glasstone, Nuclear Reactor Theory, Van Nostrand Reinhold, New York, NY, 1970.

[5] G. Peters, J. H. Wilkinson, $Ax = \lambda Bx$ and the Generalized Eigenproblem, SIAM Journal on Numerical Analysis 7 (4) (1970) 479–492.

[6] E. E. Lewis, W. F. Miller, Computational Methods of Neutron Transport, John Wiley & Sons, Inc., New York, NY, 1993.

[7] M. Machida, How to Construct Three-Dimensional Transport Theory Using Rotated Reference Frames, Journal of Computational and Theoretical Transport 45 (7) (2016) 594–609.

[8] N. Metropolis, S. Ulam, The Monte Carlo Method, Journal of the American Statistical Association 44 (247) (1949) 335–341.

[9] Z. Botev, A. Ridder, Variance Reduction, Wiley StatsRef: Statistics Reference Online (2017) 1–6.

[10] J. J. Duderstadt, L. J. Hamilton, Nuclear Reactor Analysis, John Wiley & Sons, Inc., New York, NY, 1976.

[11] E. Gelbard, Application of Spherical Harmonics Method to Reactor Problems, Tech. Rep. WAPD-BT-20, Bettis Atomic Power Laboratory (1960).

[12] R. von Mises, H. Pollaczek-Geiringer, Praktische Verfahren der Gleichungsauflösung, Zeitschrift für Angewandte Mathematik und Mechanik 9 (1929) 152–164.

[13] M. I. Ortega, P. N. Brown, T. S. Bailey, R. N. Slaybaugh, B. Chang, A Rayleigh Quotient Method for Solving the Alpha-Eigenvalue Problem in Neutron Transport, Tech. Rep. LLNL-CONF-737630, Lawrence Livermore National Laboratory (2017).

[14] M. Chadwick, M. Herman, P. Obložinský, et al., ENDF/B-VII.1 Nuclear Data for Science and Technology: Cross Sections, Covariances, Fission Product Yields and Decay Data, Nuclear Data Sheets 112 (12) (2011) 2887–2996.

[15] R. E. Macfarlane, D. W. Muir, R. M. Boicourt, A. C. Kahler, J. L. Conlin, W. Haeck, The NJOY Nuclear Data Processing System, Version 2016, Tech. Rep. LA-UR-17-20093, Los Alamos National Laboratory (2016).

[16] G. I. Petrov, Application of Galerkin's Method to the Problem of Stability of Flow of a Viscous Fluid, Journal of Applied Mathematics and Mechanics 4 (1940) 3–12 (in Russian).

[17] S. Chandrasekhar, The Radiative Equilibrium of the Outer Layers of a Star, with Special Reference to the Blanketing Effect of the Reversing Layer, Monthly Notices of the Royal Astronomical Society 96 (1935) 21–41.

[18] S. E. Strom, R. L. Kurucz, A Statistical Procedure for Computing Line-Blanketed Model Stellar Atmospheres with Applications to the F5 IV Star Procyon, J. Quant. Spectrosc. Radiat. Transfer (1966) 591–607.

[19] D. F. Carbon, A Comparison of the Straight-Mean, Harmonic-Mean, and Multiple-Picket Approximations for the Line Opacities in Cool Model Atmospheres, The Astrophysical Journal 187 (1974) 135–145.

[20] M. N. Nikolaev, V. V. Filippov, Measurement of the Resonance Parameters for Total Cross Sections of Some Elements in the Energy Region 0.3-2.7 MeV, Atom. Energ. 6 (6) (1963) 493 (in Russian).

[21] J. C. Stewart, Non-Grey Radiative Transfer, J. Quant. Spectrosc. Radiat. Transfer 4 (1964) 723–729.

[22] D. E. Cullen, G. C. Pomraning, The Multiband Method in Radiative Transfer Calculations, Journal of Quantitative Spectroscopy and Radiative Transfer 24 (2) (1980) 97–117.

[23] T. Takeda, H. Fujimoto, K. Sengoku, S. Shiroya, H. Unesaki, K. Kanda, Application of Multiband Method to KUCA Tight-Pitch Lattice Analysis, Journal of Nuclear Science and Technology 28 (9) (1991) 863–869.

[24] M. Tatsumi, A. Gihou, T. Takeda, Space and Angular Dependence of Interface Currents in the Multiband-CCCP Method, Journal of Nuclear Science and Technology 37 (7) (2000) 572–580.

[25] M. J. Milosevic, A New Subgroup Method for Resolved Resonance Treatment, Nucl. Sci. Bull. 2 (1) (1997) 9–13.

[26] T. Yamamoto, Background-Cross-Section-Dependent Subgroup Parameters, Journal of Nuclear Science and Technology 40 (6) (2003) 370–375.

[27] A. A. Wray, J.-F. Ripoll, D. Prabhu, Investigation of the Opacity Binning Approach for Solving the Shock-Generated Radiation of the Apollo AS-501 Reentry, Tech. rep., Center for Turbulence Research (2006).

[28] S.-E. Huang, K. Wang, D. Yao, An Advanced Approach to Calculation of Neutron Resonance Self-Shielding, Nuclear Engineering and Design 241 (8) (2011) 3051–3057.

[29] L. B. Levitt, Probability Table Method for Treating Unresolved Neutron Resonances in Monte Carlo Calculations, Nucl. Sci. Eng. 49 (4) (1972) 450–457.

[30] D. E. Cullen, Application of the Probability Table Method to Multigroup Calculations of Neutron Transport, Nucl. Sci. Eng. 55 (4) (1974) 387–400.

[31] P. Ribon, J. M. Maillard, Probability Tables and Gauss Quadrature: Application to Neutron Cross-Sections in the Unresolved Energy Range, ANS Topical Meeting on Advances in Reactor Physics and Safety, ANS, Saratoga Springs, NY, 1986.

[32] A. Hébert, M.Coste, Computing Moment-Based Probability Tables for Self-Shielding Calculations in Lattice Codes, Nucl. Sci. Eng. 142 (2002) 245–257.

[33] G. Chiba, H. Unesaki, Improvement of Moment-Based Probability Table for Resonance Self-Shielding Calculation, Annals of Nuclear Energy 33 (13) (2006) 1141–1146.

[34] A. T. Till, R. Lowrie, C. Fontes, Application of the Finite-Element-with-Discontinuous-Support Method to Thermal Radiation Transport, The International Conference on Mathematics and Computational Methods Applied to Nuclear Science and Engineering (M&C), Jeju, Korea, 2017.

[35] P. Vaquer, R. McClarren, Criticality Benchmarks for the Finite-Element-with-Discontiguous-Support Multigroup Method, The International Conference on Mathematics and Computational Methods Applied to Nuclear Science and Engineering (M&C), Jeju, Korea, 2017.

[36] J. Lou, Implementation of the Finite-Element-with-Discontiguous-Support Multgroup Method, Ph.D. thesis, Texas A&M University (2020).

[37] A. T. Till , M. L. Adams, J. E. Morel, The Finite-Element with Discontiguous-Support Method, Nuclear Science and Engineering 196 (2022) 53–74.

[38] G. E. Sjoden, Foundations in Applied Nuclear Engineering Analysis, World Scientific Publishing Company, 2015.

[39] J. H. Ward, Hierarchical Grouping to Optimize an Objective Function, Journal of the American Statistical Association 58 (1963) 326–244.

[40] I. I. Bondarenko, Group Constants for Nuclear Reactor Calculations, Tech. rep., Consultants Bureau, New York (1964).

[41] K. F. Riley, M. P. Hobson, S. J. Bence, Mathematical Methods for Physics and Engineering, American Association of Physics Teachers, 1999.

[42] C. Werner, MCNP Users Manual—Code Version 6.2, Tech. Rep. LA-UR-17-29981, Los Alamos National Laboratory (2017).